Characterising Material Models for Silicone-Rubber using an Inverse Finite Element Model Updating Method

by
Du Toit Viljoen

Thesis presented in partial fulfilment of the requirements for the degree of Master of Engineering (Mechanical) in the Faculty of Engineering at Stellenbosch University

UNIVERSITEIT
iYUNIVESITHI
STELLENBOSCH
UNIVERSITY

100
1918·2018

Supervisor: Prof G. Venter

March 2018

Declaration

By submitting this thesis electronically, I declare that the entirety of the work contained therein is my own, original work, that I am the sole author thereof (save to the extent explicitly otherwise stated), that reproduction and publication thereof by Stellenbosch University will not infringe any third party rights and that I have not previously in its entirety or in part submitted it for obtaining any qualification.

Date: March 2018

i

UNIVERSITEIT·STELLENBOSCH·UNIVERSITY
jou kennisvennoot • your knowledge partner

Plagiaatverklaring / Plagiarism *Declaration*

1   Plagiaat is die oorneem en gebruik van die idees, materiaal en ander intellektuele eiendom van ander persone asof dit jou eie werk is.
Plagiarism is the use of ideas, material and other intellectual property of another's work and to present is as my own.

2   Ek erken dat die pleeg van plagiaat 'n strafbare oortreding is aangesien dit 'n vorm van diefstal is.
I agree that plagiarism is a punishable offence because it constitutes theft.

3   Ek verstaan ook dat direkte vertalings plagiaat is.
I also understand that direct translations are plagiarism.

4   Dienooreenkomstig is alle aanhalings en bydraes vanuit enige bron (ingesluit die internet) volledig verwys (erken). Ek erken dat die woordelikse aanhaal van teks sonder aanhalingstekens (selfs al word die bron volledig erken) plagiaat is.
Accordingly all quotations and contributions from any source whatsoever (including the internet) have been cited fully. I understand that the reproduction of text without quotation marks (even when the source is cited) is plagiarism.

5   Ek verklaar dat die werk in hierdie skryfstuk vervat, behalwe waar anders aangedui, my eie oorspronklike werk is en dat ek dit nie vantevore in die geheel of gedeeltelik ingehandig het vir bepunting in hierdie module/werkstuk of 'n ander module/werkstuk nie.
I declare that the work contained in this assignment, except where otherwise stated, is my original work and that I have not previously (in its entirety or in part) submitted it for grading in this module/assignment or another module/assignment.

Studentenommer / *Student number*	Handtekening / *Signature*
Voorletters en van / *Initials and surname*	Datum / *Date*

Abstract

Characterising Material Models for Silicone-Rubber using an Inverse Finite Element Model Updating Method

D. Viljoen

Thesis: Master of Engineering (Mechanical)

March 2018

Silicone-rubber was investigated and its mechanical behaviour was characterised. Uni-axial tensile tests were conducted on two different sample geometries: rectangular flat strip and dumbbell shaped. Bi-axial bubble inflation tests were done on membranes and unconstrained uni-axial compression tests were conducted on cylindrical samples. Two identification methods were incorporated to determine three constitutive hyper-elastic material models from every experimental test: the direct and inverse. The direct method is the more traditional approach, where experimental data is used with a least squares fit to determine the constants that govern the material model. The inverse method is fundamentally different, it requires a finite element (FE) model and experimental results. The experimental results are used as boundary conditions in the FE model. Numerical optimisation is then used to obtain the material model constants that minimise the error between the FE model and the experimental results. The material models investigated in this thesis include the Mooney-Rivlin two- and three parameter models along with the Ogden three parameter model. Finally, an independent validation test was done, with a complex stress state. The validation test along with the extrapolation of each material model into all three stress states (uni-axial tension, -compression and bi-axial tension), served as the criteria to determine the best material model and identification method. It was found that the Mooney-Rivlin three parameter model obtained from uni-axial tensile tests (both sample geometries) using both the direct and inverse FE model updating method delivered the best results. However, additional user-input constraints were needed for the direct method (inverse method required no constraints) to obtain a material model that predicted feasible material behaviour.

iii

Uittreksel

Karakterisering van Materiaalmodelle vir Silikoon-Rubber met behulp van 'n Inverse Eindige Element Model Opdateringsmetode

("Characterising Material Models for Silicone-Rubber using an Inverse Finite Element Model Updating Method")

D. Viljoen

Tesis: Magister in Ingenieurswese (Meganiese)

Maart 2018

Silikoon-rubber is ondersoek ten einde sy meganiese gedrag te karakteriseer. Eenassige trektoetse was uitgevoer op twee verskillende steekproef geometrieë: reghoekige plat strook en 'n hondebeen vorm. Verder was tweeassige borrel-inflasietoetse op membrane uitgevoer, asook onbeperkte eenassige druktoetse op silindriese monsters. Twee identifikasiemetodes is gebruik om drie hiperelastiese-materiaalmodelle vanaf elke eksperimentele toets te bepaal: die direkte en die inverse metodes. Die direkte metode is die meer tradisionele benadering waar eksperimentele data gebruik word met 'n minste vierkante passing om die konstantes wat die materiaalmodel beheer, te bepaal. Die inverse metode verskil fundamenteel hiervan deurdat dit 'n eindige element model tesame met die eksperimentele resultate vereis. Die eksperimentele resultate word as grensvoorwaardes vir die eindige element model gebruik. Numeriese optimering word dan gebruik om die materiaalmodel se konstantes te bepaal wat die fout tussen die eindige element model en die eksperimentele resultate minimeer. Die materiaalmodelle wat ondersoek is sluit in, die Mooney-Rivlin twee- en drie parametermodelle, sowel as die Ogden drie-parameter model. Tenslotte was 'n onafhanklike trektoets met 'n komplekse spanningstoestand uitgevoer om die modelle te valideer. Die valideringstoets saam met die ekstrapolasie van elke materiaalmodel in al drie spanningstoestande (eenassige spanning, -druk en tweeassige spanning) dien as die kriteria om die beste materiaalmodel en identifikasiemetode te bepaal. Daar was bevind dat die drie-parametermodel van Mooney-Rivlin, verkry vanaf eenasige trektoetse (vir beide steekproef geometrieë) met behulp van beide die direkte metode en

die inverse eindige element model opdateringsmetode, die beste resultate gele-
wer het. Daar word egter addisionele beperkings benodig vir die gebruik van
die direkte metode (teenoor die inverse metode wat geen beperkings vereis nie)
ten einde 'n wesenlike model te verkry, wat logiese materiaalgedrag voorspel.

Acknowledgements

I would like to express my sincere gratitude to the following people:

Thank you Prof. Gerhard Venter for the guidance and support. I have acquired a lot of technical knowledge and work etiquette. Thank you for taking me in as a student and helping me find work for when I am done with this thesis.

Thank you Dr. Martin Venter, without you, the whole topic of silicone-rubber would not have happened. Thank you also for a lot of technical advise given over the past few years.

Thank you mother and father for all the love and support you gave me over the past few years.

And lastly I would like to thank our Father in Heaven for the opportunity and ability to complete a masters degree.

Table of Contents

List of Figures

List of Tables

Chapter 1

Introduction

This chapter will discuss the background and motivation for the work presented here. The objectives will be explained, followed by a presentation of the layout of this thesis.

1.1 Background

Silicone-rubber is used in a wide variety of fields, which include mould making, bio-medical applications and soft robotics. These silicone-rubbers exhibit good chemical, heat and abrasion resistance, with excellent bio-medical compatibility. In order to effectively design with these materials, a good characterisation of the materials' behaviour is required.

The simplest way to characterise silicone-rubber is to conduct uni-axial tensile tests, and to determine constitutive hyper-elastic material models from the test data using a least squares fit (direct method), as was done by Polygerinos *et al.* (2013) and Case *et al.* (2015). While Martins *et al.* (2006) used an inverse FE model updating method on uni-axial tensile data to determine hyper-elastic material models of silicone-rubber and soft tissue.

To better predict more complex stress states, other experimental tests may also be conducted, like the uni-axial compression or bi-axial bubble inflation tests, as by Meunier *et al.* (2008) and Sasso *et al.* (2008). To demonstrate the effects of the non-linear time dependent properties of silicone-rubber,Case *et al.* (2015) characterised three silicone-rubbers using uni-axial pull to failure tests, cyclic loading tests and stress relaxation tests.

While all these studies provide valuable information, it is necessary to note that there exists possible further contributions to this field. An example is the use of an inverse method to characterise silicone-rubber using more than just uni-axial tensile data. Another is to investigate the effect of extrapolating

1

a hyper-elastic material model into different stress states (eg. from uni-axial tensile to uni-axial compression) to evaluate the predictability of the model. Both examples form part of this thesis, which aims to contribute to the ongoing research in the characterisation of the mechanical response of silicone-rubber. Details regarding the experimental tests, constitutive models and methods used to determine the models will be provided.

1.2   Objectives

This thesis developed material models, using different experimental tests and methods for the silicone-rubber Smooth-Sil-950. While only one silicone-rubber was used, the primary aim of this thesis was to serve as a guide for the characterisation of any similar silicone-rubber. Three experimental tests were employed: uni-axial tensile, uni-axial compression and bi-axial bubble inflation. Three commonly used constitutive hyper-elastic models were used, which included the Mooney-Rivlin two parameter model as an introductory model. Following this, the more complex Mooney-Rivlin three parameter and Ogden three parameter models were employed. All models were characterised using two methods, the direct and the inverse FE model updating method. All tests, models and methods are explained in Chapter 2.

To determine the best way to characterise the mechanical behaviour of silicone-rubber, it is necessary to compare different models and methods. Therefore an independent validation test was developed, where a tensile test was conducted on a complex test sample (Chapter 10 and the predicted and measured response was compared).

To accomplish the aim of this thesis, the following summarised objectives must be met:

- Determine different material models using different tests and methods.

- Evaluate each model against the independent validation test.

- Extrapolate each model into different stress states to determine the predictability of that model.

- Using the validation test and extrapolation results to determine the best material model and method.

1.3   Thesis Layout

This thesis is composed of eleven chapters which follow the logical steps that were taken. Necessary literature and concepts to understanding this thesis can be found in Chapter 2. A discussion on the polynomial fitting of experimental data is presented in Chapter 3. Chapter 4 is a discussion on the relative displacement field method that was utilised during uni-axial tensile tests. The silicone-rubber moulding process can be found in Chapter 5. The uni-axial tensile test method with all the material models obtained are discussed in Chapter 6. Chapter 7 presents the bi-axial bubble inflation test method as well as all the material models obtained. Chapter 8 is the discussion of the uni-axial compression test method with the material models obtained. A special material model where uni-axial tensile and compression data are combined is discussed in Chapter 9. The validation test and model extrapolation evaluation results can be found in Chapter 10. The thesis is then concluded in Chapter 11 along with a discussion on future work.

Chapter 2

Literature and Concepts

This chapter will discuss literature, concepts and theory to help understand the work presented in this thesis. The topics will include experimental tests, silicone rubber, material models, Digital Image Correlation (DIC), the inverse Finite Element (FE) model updating method, numerical optimisation and explaining how a non-linear FE solver works.

2.1 Experimental Tests

The following section will give a brief background followed by a literature review on the tests that were done in this thesis. It will start with the uni-axial tensile test. Followed by the bi-axial bubble inflation test. Finally, the unconstrained uni-axial compression test will be discussed.

2.1.1 Uni-axial Tensile Test

The uni-axial tensile test is the most common test to use when determining material properties. An investigation of material properties, normally starts with a uni-axial tensile test. However, it has its limitations. Real world problems will rarely be subjected to a one directional stress-state. Sasso *et al.* (2008) stated that uni-axial tensile data cannot accurately characterise a hyper-elastic material, especially for applications with bi-axial loadings such as inflatable tubes or membranes

Consider Figure 2.1, and assuming the material is incompressible, the engineering stress in the Y-direction can be calculated by:

$$\sigma_{eng-yy} = \frac{F_{yy}}{w_0 t_0} \tag{2.1}$$

where F_{yy} is the force measured by a load cell in the Y-direction, w_0 is the initial gauge width of the sample and t_0 the initial gauge thickness. The stretch in the Y-direction (Figure 2.1) can be calculated by:
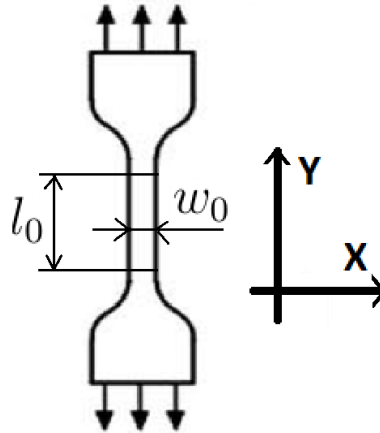
Figure 2.1: Uni-axial tensile test dumbbell shaped sample.

$$\lambda_{yy} = \frac{l}{l_0} \tag{2.2}$$

where l is the gauge length at the instant of acquisition and l_0 the initial gauge length. To define the specifics regarding the uni-axial tensile test, it is necessary to first take a look at some literature.

Meunier *et al.* (2008) characterised silicone-rubber using five homogeneous tests, one of which was the uni-axial tensile test. Dumbbell shaped samples were used, having an initial gauge length (l_0) of 60 mm, a gauge width (w_0) of 12 mm and a gauge thickness (t_0) of 2 mm. Samples were held in place with self-tightening grips, with a rated load cell of 250 N. The deformation of the sample was recorded using a DIC system. The silicone-rubber was assumed to be incompressible. The nominal stress tensor (First Piola-Kirchhoff stress tensor), as well as the deformation gradient tensor, were assumed to be homogeneous during the tests.

Sasso *et al.* (2008) characterised hyper-elastic rubber-like materials using uni-axial and bi-axial tension tests based on optical methods. Dumbbell shaped specimens was used, according to the ISO 37:2005 standard, with an initial gauge length (l_0) of 40 mm, a gauge width (w_0) of 9 mm and a gauge thickness (t_0) of 1.7 mm. A rated load cell of 5 kN was used. The deformation of the sample was recorded using a high-resolution video extensometer.

Case *et al.* (2015) characterised silicone-rubbers for robotic applications employing uni-axial pull-to-failure tests. Dumbbell shaped samples was used, having an initial gauge length (l_0) of 25.4 mm, a gauge width (w_0) of 5.334 mm and a gauge thickness (t_0) of 0.64 mm. A rated load cell of 1 kN was used, along with custom-made material grips.

Using these articles as a guide, the uni-axial tensile method for this thesis was developed and can be found in Chapter 6.

2.1.2 Bi-axial Bubble Inflation Test

While the uni-axial tensile test can be simplified as a 2D test, the bi-axial bubble inflation test works in 3D space. Furthermore, it provides bi-axial data which is a better representation for inflatable tubes or membranes. By clamping a circular specimen by its periphery and introducing a controlled pressure from one side, the out of plane deformation of the membrane can be related to the pressure. The stress-state can then be described as being equi-bi-axial at the pole, because of axial symmetry. Treloar (1944) was the first to use bubble inflation with compressed air in 1944, to study the behaviour of natural rubber and its mechanics of bursting.

Assuming the material is incompressible and isotropic, an assumption of hemispherical deformation during inflation can be made. The engineering stress in each direction at the polar area (area around centre of the membrane) can then be calculated by the following equation (Meunier *et al.*, 2008):

$$\sigma_{xx} = \sigma_{yy} = \frac{PR_c\lambda}{2t_0} \tag{2.3}$$

where P is the pressure which is recorded during the test, R_c the radius of the curvature of the bubble, λ the stretch and t_0 the original membrane thickness. With the assumptions stated previously, the stretch in the X-direction λ_{xx} is equal to the stretch in the Y-direction λ_{yy}. This can be calculated by:

$$\lambda = \frac{l}{l_0} \tag{2.4}$$

where l is the length of arc of the surface element of the polar area at the instant of acquisition, and l_0 is the initial polar area length. The variables l and l_0 can be calculated by the diameter of a predefined virtual circle at the pole area, and the radius of curvature of the bubble (Figure 2.2).

Assuming that the centre of the circle remains at the pole point during inflation, the stretch can be calculated in the following way (Bojtos, 2010):

$$\lambda = \frac{2R_c \arcsin\left(\frac{d}{2R_c}\right)}{d_0} \tag{2.5}$$

where d_0 is the initial virtual circle diameter, and d is the diameter at the instant of acquisition. Since the bubble shape is assumed to be hemispherical, the radius of curvature R_c can be estimated by:
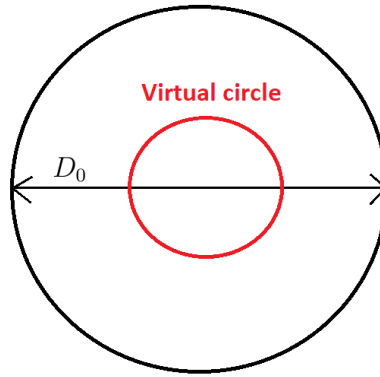
Figure 2.2: Bi-axial bubble inflation membrane.

$$R_c = \frac{a^2 + H^2}{2H} \tag{2.6}$$

where a is the flat membrane radius, thus $\frac{D_0}{2}$ and H is the apex height of the bubble. These equations holds true if the assumptions made are correct. The confirmation of the assumptions that the bubble deform symmetrically and hemispherical can be found in Chapter 7. The bi-axial bubble inflation method for this thesis was developed by using the following studies, among others.

Reuge *et al.* (2001) characterised an elastomer using the bubble inflation method. A sample membrane with an initial diameter (D_0) of 40 mm and initial thickness (e_0) of 2 mm was used. Air pressure was used to inflate the membrane and a pressure sensor recorded the pressure, which was located at the backside of the membrane. The deformation of the inflated membrane was recorded using a CCD camera (752 x 582 pixels). It was observed that at low elongations, the membrane deformed in a hemispherical shape. The radius of curvature (R_c) was calculated using a least squares fit on the polar area contour.

Meunier *et al.* (2008) also used bubble inflation tests. Sample membranes had an initial diameter (D_0) of 200 mm and initial thickness (e_0) of 2 mm. Air pressure was used to inflate the membrane and was recorded by a rated pressure sensor of 0-50 kPa. Deformation was recorded using a DIC system consisting of two commercial CCD cameras (3872 x 2592 pixels). The material was assumed to be isotropic. As $D_0 >> e_0$, the stress was assumed to be constant along the thickness.

The detailed discussion on the bi-axial bubble inflation technique used in this thesis can be found in Chapter 7.

2.1.3   Unconstrained Uni-axial Compression Test

During a compression test, a hyper-elastic material exhibits non-linear material behaviour. While a material model determined from uni-axial tensile or bi-axial tensile data can be extrapolated to predict compression data, it is necessary to validate the extrapolated data. When cylindrical samples are used, and incompressibility and symmetry are assumed, the degree of compression, which is the same as stretch, (λ_{yy}) can be calculated by:

$$\lambda_{yy} = \frac{h}{h_0} \tag{2.7}$$

where h_0 is the initial height and h is the height at the instant of acquisition. The engineering stress can the be described as:

$$\sigma_{yy} = \frac{4F_{yy}}{\pi D_0^2} \tag{2.8}$$

where F_{yy} is the compression force and D_0 is the initial specimen diameter. Using the following study as guide, the uni-axial compression test method for this thesis was developed and can be found in Chapter 8.

Meunier *et al.* (2008) used unconstrained uni-axial compression tests as part of the five homogeneous tests to characterise silicone-rubber. Cylindrical samples were used, having an initial diameter (D_0) of 37 mm and initial height (h_0) of 20 mm. Samples were tested using a uni-axial testing rig with flat circular (larger than the sample) platforms. The platforms were coated with a silicone grease to limit the friction during tests. Symmetry and incompressibility were assumed to simplify calculations. A rated load cell of 5 kN was used.

2.2   Silicone Rubber

The silicone-rubber that was used in this thesis was the Smooth-Sil 950 silicone-rubber from AMT composites. This silicone-rubber can cure at ambient temperature with negligible shrinkage (<0.0001 mm/mm) and a shore A hardness of 50A (Smooth-On, 2012). It is normally used for making production moulds using casting materials such as plasters, wax, concrete, low-melt metal alloys or resins. These materials can be cast into the silicone rubber mould without any release agent. Smooth-Sil 950 has a rated tensile strength at break of 5 MPa (320% elongation) with working temperatures between -19 °C to 232 °C (Smooth-On, 2012). For this thesis, the silicone-rubber will be characterised from -35 % to 100 % strain (stretch of 0.65 to 2) at ambient temperature.

2.3   Material Models

Mooney (1940) and Rivlin (1948) discovered, through experimental measurements of the stress-strain relationships of rubber like materials, that linear theory is an inadequate solution to predicting the mechanical properties of such materials. This is due to the non-linear behaviour as well as large elastic strains observed during testing.

In order to study materials with non-linear elsatic behaviour, which usually undergo large strains with small applied stresses, a non-linear version of the classical elasticity theory was developed by Ogden (1984). The non-linear theory of elasticity, which constitutes the theoretical basis for the study of hyper-elastic materials, such as silicone rubbers uses a strain-energy function (W) to describe in energetic terms the mechanical behaviour of this class of materials.

To capture the non-linear mechanical properties of the material in this study (silicone-rubber), three models will be used: the Mooney-Rivlin two parameter, Mooney-Rivlin three parameter and Ogden three parameter material models. It can be assumed that silicone-rubber behave like an isotropic, hyper-elastic and non-linear material (Martins *et al.*, 2006). The strain energy function (W) can then be described as a function of the strain invariants:

$$W = W(I_1, I_2, I_3) \tag{2.9}$$

where:

$$
\begin{aligned}
I_1 &= \lambda_1^2 + \lambda_2^2 + \lambda_3^2 \\
I_2 &= \lambda_1^2\lambda_2^2 + \lambda_2^2\lambda_3^2 + \lambda_1^2\lambda_3^2 \\
I_3 &= \lambda_1^2\lambda_2^2\lambda_3^2
\end{aligned}
\tag{2.10}
$$

here λ_1, λ_2 and λ_3 are the principle stretches. Assuming that the material is also incompressible ($I_3 = 1$), Equation 2.9 becomes:

$$W = W(I_1, I_2) \tag{2.11}$$

The principle Cauchy stresses can be expressed as a function of the stretches as follows:

$$\sigma_i = \lambda_i \frac{\partial W}{\partial \lambda_i} + p, \quad i = 1, 2, 3 \tag{2.12}$$

where p is the hydrostatic pressure which can be determined from boundary conditions (Martins *et al.*, 2006).

Martins *et al.* (2006) did a comparative study of several material models for the prediction of hyper-elastic properties, with the application to silicone-rubber and soft tissues, using data obtained from uni-axial tensile tests. Using this as the basis, the following three models were selected for this thesis.

2.3.1 Mooney-Rivlin Material Model

This model was one of the first hyper-elastic models that was developed in 1940. It is still widely used today, for it has a high accuracy when predicting the non-linear behaviour of isotropic, rubber-like materials (Mooney, 1940).

2.3.1.1 Two Parameter Mooney-Rivlin Model

The strain-energy equation for this model can be seen in the following equation:

$$W = C_{10}\left(I_1 - 3\right) + C_{01}\left(I_2 - 3\right) \tag{2.13}$$

where C_{10} and C_{01} are empirically determined material constants, and I_1 and I_2 are the first and second invariant of the uni-modular component of the Cauchy-Green deformation tensor, respectively.

2.3.1.2 Three Parameter Mooney-Rivlin Model

The three parameter Mooney-Rivlin material model in terms of the strain energy can be described as the following:

$$W = C_{10}\left(I_1 - 3\right) + C_{01}\left(I_2 - 3\right) + C_{20}\left(I_1 - 3\right)^2 \tag{2.14}$$

where C_{10}, C_{01} and C_{20} are empirically determined material constants, and I_1 and I_2 are the first and second invariant of the uni-modular component of the Cauchy-Green deformation tensor, respectively.

2.3.2 Ogden Three Parameter Material Model

The Ogden hyper-elastic material model used to describe the non-linear stress-strain behaviour of elastic materials was first developed by Ogden (1984). The Ogden model, like other hyper-elastic material models, describes the material behaviour by means of a strain-energy equation. This equation has the general form:

$$W = \sum_{i=1}^{N} \frac{\mu_i}{\alpha_i}\left(\lambda_1^{\alpha_i} + \lambda_2^{\alpha_i} + \lambda_3^{\alpha_i} - 3\right) \tag{2.15}$$

When $N = 3$, excellent convergence between theoretical and experimental results are achieved for silicone rubber (Holzapfel, 2000). For stability, parameters α_i and μ_i needs to be real, positive or negative, satisfying the condition that:

$$\frac{1}{2}\sum_{i=1}^{N}\mu_i\alpha_i = \mu \tag{2.16}$$

where μ is the ground state shear modulus. Note that the Ogden three parameter model has six unknowns, three constants (μ_i) and three exponents (α_i).

For this thesis, the Mooney-Rivlin two parameter model is used as an introductory model, and will only be determined for uni-axial tensile test data. Thereafter the more complex Mooney-Rivlin three parameter and Ogden three parameter models will be determined from all experimental test data.

2.4   Digital Image Correlation

Digital Image Correlation (DIC) is a tool used to calculate deformation from a sequence of consecutive images (LaVision, 2014). The DIC system is incorporated during an experimental test to capture images as a test sample deforms. Each image is split into subsets of $N \times N$ pixels, which is defined by the user. It is important that a unique contrast pattern is present in each individual subset. This is obtained by covering samples in a random speckle pattern as can be observed in Figure 2.3.
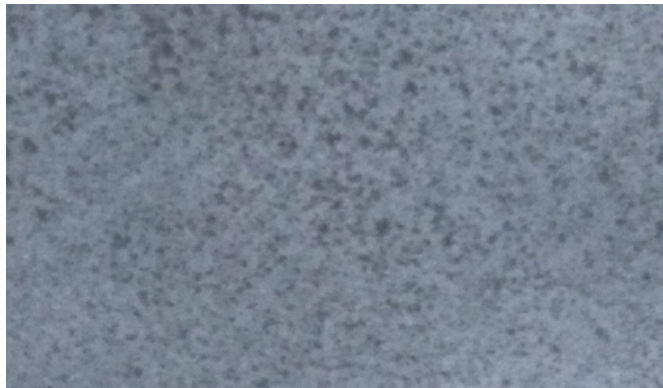
Figure 2.3: Typical random speckle pattern on samples (medium to high relative speckle density).

Then by using the least squares method and an iterative optimisation procedure, linear transformations to the contrast pattern of subsequent images can be calculated. This will result in a subset deformation when the subset changes shape and location. This process is repeated across the entire image to obtain the full displacement field.

In this thesis, the DIC system used is a product of LaVision (2014). The StrainMaster Portable DIC hardware was used along with two VC-Imager E-lite 5-megapixel cameras (LaVision, 2014), and can be seen in Figure 2.4a. Using two cameras enables the DIC system to capture 3D stereoscopic displacement measurements on the surface of a sample. The software used to calculate the displacement fields from images captured by the StrainMaster, was processed using DaVis, also a product from LaVision (2014). The system was calibrated with a calibration plate, as can be seen in Figure 2.4b, before capturing a sequence of images to ensure sub-pixel accuracy.

(a) DIC system.

(b) DIC calibration plate.

Figure 2.4: DIC equipment used in this thesis.

To investigate the effect of different speckle patterns, a speckle pattern sensitivity study was conducted. Speckle patterns of three different densities with three different subset sizes each were tested. Five sequential images were taken for each variation without any external induced deformation. These images were then processed to calculate the deformation using the DaVis software. This deformation can be seen as noise or errors due to no externally applied deformation. Table 2.1 shows the root mean square (RMS) error values of the noise deformation for the different speckle pattern candidates. It can be observed that the high relative density speckle pattern yielded the best results

with the low relative density speckle the worst. The results also indicate that using a larger subset will decrease the RMS error. However, increasing the size of the subset will decrease the spatial resolution (Crammond *et al.*, 2013). For this thesis, a medium to high speckle density was used (Figure 2.3), with a subset size of around 51 to have a balance between accuracy and spatial resolution.

Table 2.1: Comparison of RMS error values of the noise deformation for candidate speckle patterns.

Relative speckle density	Subset size [Pixel]	RMS [μm]
	23	6.858
High	51	4.982
	73	2.703
	23	13.24
Medium	51	4.204
	73	3.255
	23	31.205
Low	51	25.492
	73	15.047

The three-dimensional capabilities of the DIC system were already studied by Jekel (2016), who used the same DIC system as used in this thesis. It was used to measure the radius (40 mm) of a steel bearing ball, to understand and quantify the three-dimensional capabilities of the system. The DIC system determined the radius of the steel bearing ball with an error of 0.42 %. This suggested that the DIC system can accurately determine data points on a surface of a curved object. It is important to note, that for this thesis, the DIC method is only used as a tool to determine the displacements.

2.5   Inverse Finite Element Model Updating Method

All identification methods to determine material models can be classified as either direct or inverse. Uni-axial tension, uni-axial compression and bi-axial tension tests are usually conducted to obtain hyper-elastic material models for silicone rubbers. With the direct method, an experimental test is conducted and the material's constitutive relationship, usually stress-strain data, is determined. Using the stress-strain data, a simple least square fit is done to determine a hyper-elastic material model. The resulting material model is then used directly in an FE analysis that replicates the testing conditions. Ideally, it is then shown that the material model is capable of replicating the

behaviour of the experimental test.

The inverse method is fundamentally different from the direct method. With the inverse method, an FE analysis is created parallel to the experimental tests. This FE analysis replicates the conditions of the experimental test. Numerical optimisation is then used to determine the best material model parameters by minimising the difference between the FE analysis and the corresponding experimental test results. Figure 2.5 shows a work flow diagram of the inverse FE model updating method. The stopping criteria utilised by this thesis is a root means square (RMS) error value between the experimental results and the FE analysis. When the force is used as the boundary condition, displacement fields are compared between the FE analysis and the experimental test results and calculated by the following equation:

$$RMS = \frac{1}{M} \sum_{j=1}^{M} \left(\frac{1}{N} \sum_{i=1}^{N} \left(\sqrt{(Disp_{FE} - Disp_{Exp})^2} \right) \right) \qquad (2.17)$$

where $i = 1, N$ is the number of nodes in the respective displacement fields, and $j = 1, M$ is the number of iterations within the FE analysis. The FE analysis has iterations because non-linear FEM is being used due to the non-linear nature of the silicone-rubber. $Disp_{FE}$ and $Disp_{Exp}$ are the displacement of the same node but from the FE analysis and experimental results respectively.

When the edge displacements are used as the boundary conditions, the reaction forces are then compared between the FE analysis and the experimental results. An equation similar to Equation 2.17 is then used to calculate the RMS error value.

While each identification method has advantages, the inverse FE model updating method can characterise a material with a load state that is more complex than traditional uni-axial or bi-axial testing. This added complexity may be more representative of reality. This also gives the advantage of replacing multiple simple tests with one more complex test. (Garbowski *et al.*, 2011).

Using the following studies as a guide, the inverse FE model updating method for this thesis was developed.

Jekel *et al.* (2016) performed uni-axial tests on PVC-coated polyester to determine a non-linear orthotropic material model. An inverse bubble inflation method was then described and demonstrated on the same PVC-coated polyester material, to also obtain a non-linear orthotropic material model. To validate the material models obtained, a three point bending test using inflated PVC-coated polyester was used. It was concluded that the bubble material
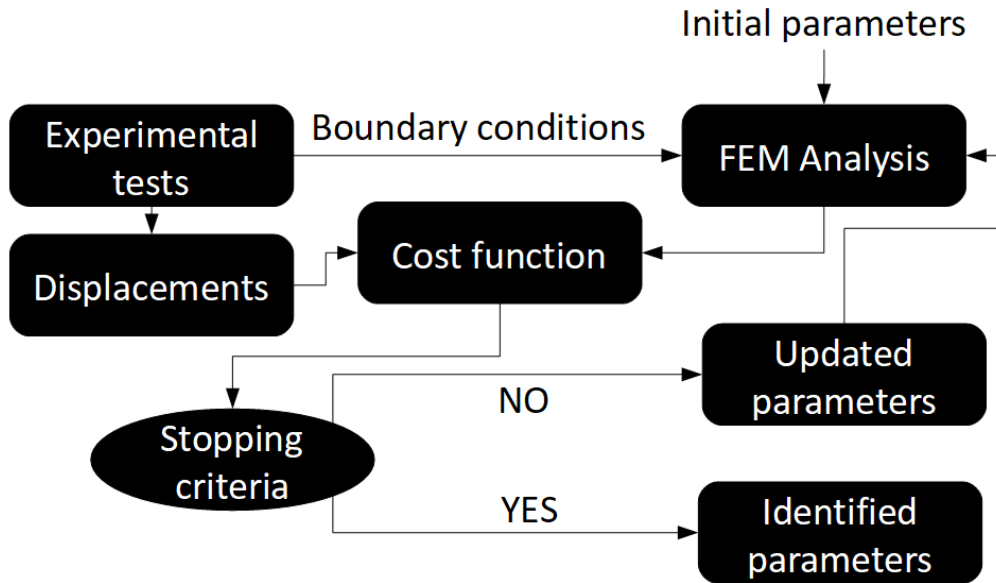
Figure 2.5: Work flow diagram of the inverse FE model updating method.

model overestimated the stiffness of the inflatable beams, while the uni-axial material model underestimated the stiffness.

Fazzini *et al.* (2011) identified constitutive material parameters (elastic and elasto-plastic) of aluminium 2024-T4 using full displacement fields. This was done using uni-axial tests along with two identification techniques, the virtual fields method and the FE model updating method. It was concluded that the FE model updating method is more adaptive than the virtual fields method, but it required more calculation time.

2.6   Numerical Optimisation and VisualDOC

Numerical optimisation is the corner stone of the inverse FE model updating method. It is traditionally used to determine the best solution to a mathematically defined problem. In engineering, numerous design problems can be defined as mathematical problems. For this reason, numerical optimisation plays a large role in solving engineering problems. Vanderplaats Research & Development (2013b) defines a non-linear, constrained engineering problem as follows:

Find a set of design variables, $\boldsymbol{x}_i, i = 1, \cdots, N$ contained in the vector $\boldsymbol{x}$, that will

$$Minimise \quad F(\boldsymbol{x}) \tag{2.18}$$

Subject to:

$$
\begin{aligned}
g_j(\boldsymbol{x}) \leq 0, &\quad j = 1, M \\
h_k(\boldsymbol{x}) = 0, &\quad k = 1, L \\
x_i^L \leq x_i \leq x_i^U, &\quad i = 1, N
\end{aligned}
\tag{2.19}
$$

where $F(\boldsymbol{x})$ is the objective function, that depends upon the design variables ($\boldsymbol{x}$). Each variable may have a lower (x_i^L) and upper (x_i^U) bound. The feasibility of the optimisation problem can be defined by inequality ($g_j(\boldsymbol{x})$) and equality ($h_k(\boldsymbol{x})$) constraints.

The two main categories of optimisation algorithms are gradient and non-gradient based optimisation. Gradient based optimisation algorithms work by starting from a single design point and then using gradient information (typically obtained from finite difference calculations) to obtain a search direction. Normally, a line search method is then performed in the search direction to obtain a better design point. This process is repeated until convergence (usually defined by a pre-defined tolerance) is reached. Non-gradient based methods do not use gradient information. Instead, they utilise a set of design points to obtain convergence. Popular methods include the particle swarm algorithm or the genetic algorithm, which is a heuristic based algorithm (Venter, 2010).

Optimisation algorithms perform differently for each individual engineering problem. For the numerical optimisation of the material model parameters of the inverse problem, gradient based algorithms are recommended by Jekel *et al.* (2016). This is because gradient based algorithms are more computationally efficient than non-gradient based algorithms.

VisualDOC was used throughout this thesis. It is a general purpose multidisciplinary design, optimisation, and process integration software (Vanderplaats Research & Development, 2013, July). The work flow (Figure 2.5) was created using VisualDOC. Design Optimisation Tools (DOT) is the optimisation library used by VisualDOC. DOT was designed to be used as an engineering optimiser, thus the algorithm attempts to stay in the feasible region as much as possible during the one-dimensional search and aims to find a near optimum design quickly. (Vanderplaats Research & Development, 2013a).

Jekel *et al.* (2016) used three algorithms employed by DOT, to obtain nonlinear orthotropic material models for PVC-coated polyester via the inverse bi-axial bubble inflation test method:

1. The Sequential Linear Programming (SLP) algorithm.

2. The Sequential Quadratic Programming (SQP) algorithm.

3. The Modified Method of Feasible Directions (MMFD) algorithm.

It was concluded that the MMFD method consistently performed the best.

The optimisation problem considered in this paper has the undesired feature that not all combinations of the design variables (the material model constants) will result in a valid FE analysis. It is quite possible that the optimisation algorithm proposes a set of design variables that will result in a FE analysis that fails to converge. This problem is addressed by adding a boolean constraint to indicate a failed versus successful FE analysis. Such a Boolean constraint would normally pose a problem for a gradient based optimizer since the gradient will always be zero within both the feasible and infeasible regions. However, within the DOT environment this Boolean constraint can be implemented, by exploiting the particular behaviour of the optimization algorithm itself. The MMFD and SQP in DOT makes use of a one dimensional search, where a design iteration consists of first determining the gradient information at the current design point (typically by using finite difference gradient calculations), followed by the one-dimensional search. Once DOT reaches a feasible design point, it will remain in the feasible design space. If the one-dimensional search is started from a feasible design point and a constraint violation is encountered during the one-dimensional search, DOT will simply backtrack to the previously found feasible design point until the one dimensional search provides a feasible result. New gradient information is then calculated about this design point and the process is repeated until convergence is found. As a result of this behaviour, it is thus possible to successfully implement Boolean type constraints in the DOT environment, provided that the optimization process is started from a feasible design point.

It is worth noting that it is not within this thesis' scope to find the best optimisation algorithm or parameters. Instead, the optimisation is seen as a black-box method, using the MMFD algorithm as suggested by previous work.

2.7   Non-linear Finite Element Software

Hyper-elastic material models along with large displacements are non-linear and it is thus necessary to use a non-linear FE analysis solver. MSC Marc (2015) was used as the non-linear FE analysis software throughout this thesis. Marc is an implicit non-linear FE analysis solver, which uses the Newton-Raphson method to solve non-linear equilibrium equations in a structural analysis by considering the following set of equations (taken from (MSC Software, 2015)):

$$\boldsymbol{K}(\boldsymbol{u})\delta\boldsymbol{u} = \boldsymbol{f} - \boldsymbol{r}(\boldsymbol{u}) \tag{2.20}$$

where $\boldsymbol{K}$ is the tangent-stiffness matrix, $\boldsymbol{u}$ is the nodal-displacement vector, $\boldsymbol{f}$ is the external nodal-load vector and $\boldsymbol{r}$ is the internal nodal-load vector. Both $\boldsymbol{r}$ and $\boldsymbol{K}$ are functions of $\boldsymbol{u}$. The applied load ($\boldsymbol{f}$) is also a function of $\boldsymbol{u}$ in many cases. If the last obtained approximate solution is $\delta\boldsymbol{u}^i$, where i indicates the iteration number, Equation 2.20 can be written as:

$$\boldsymbol{K}(\boldsymbol{u}_{n+1}^{i-1})\delta\boldsymbol{u} = \boldsymbol{f} - \boldsymbol{r}(\boldsymbol{u}_{n+1}^{i-1}) \tag{2.21}$$

This equation is solved for $\delta\boldsymbol{u}^i$ and the next appropriate solution is determined by:

$$\begin{aligned} \triangle\boldsymbol{u} &= \triangle\boldsymbol{u}^{i-1} + \delta\boldsymbol{u}^i \\ \boldsymbol{u}_{n+1}^i &= \boldsymbol{u}_n + \triangle\boldsymbol{u}^i \end{aligned} \tag{2.22}$$

The solving of these equations completes one iteration, and the process is repeated until convergence is reached.

The Newton-Raphson method is graphically illustrated in Figure 2.6, where the method is used in one-dimension to find the roots of the function:

$$\boldsymbol{F}(\boldsymbol{u}) - 1 = \sqrt{\boldsymbol{u}} - 1 = 0 \tag{2.23}$$

starting from increment 1 where $\boldsymbol{F}(\boldsymbol{u}_0) = 0.2$ to increment 2 where $\boldsymbol{F}(\boldsymbol{u}_{last}) = 1$. The iteration process stops when the convergence criteria is satisfied.

There exists three types of convergence criteria in Marc:

1. Residual checking.

2. Displacement checking.

3. Strain energy checking.

Residual checking minimises the maximum nodal residual force ($F_{Residual}$) divided by the maximum nodal reaction force ($F_{Reaction}$) with respect to a tolerance set by the user (Equation 2.24).

$$\frac{max(|F_{Residual}|)}{max(|F_{Reaction}|)} < Tolerance \tag{2.24}$$

Displacement checking minimises the maximum nodal displacement of an iteration (δu) divided by the maximum nodal displacement of the increment ($\triangle u$) with respect to a tolerance set by the user. (Equation 2.25).

$$\frac{max(|\delta u|)}{max(\triangle u|)} < Tolerance \tag{2.25}$$

Both the residual and displacement checking are relative convergence criteria. The strain energy checking criteria is similar to the displacement checking, but the global strain energy is minimised. The convergence criteria used within
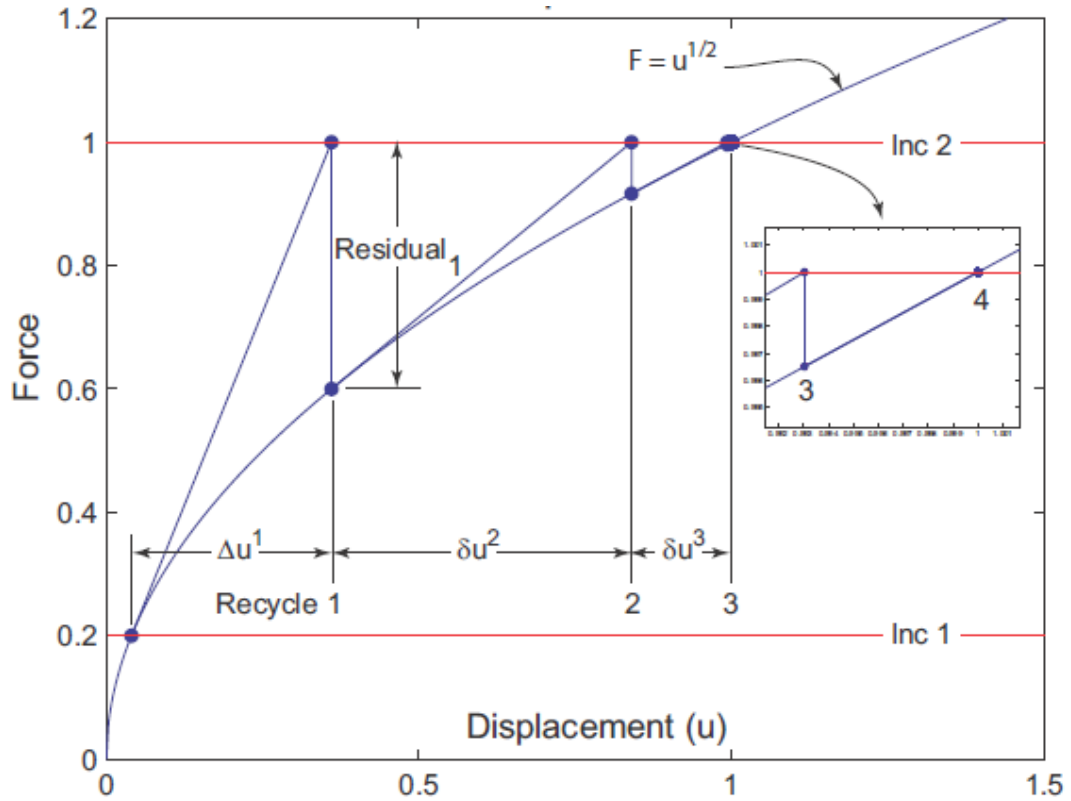
Figure 2.6:   Newton-Raphson method to solve a non-linear FE analysis (MSC Software, 2015).

this thesis were the same as in the study by Jekel *et al.* (2016), who utilised the full Newton-Raphson method with a combination of the residual checking and displacement checking criteria. Maximum tolerances were set at 0.001.

Chapter 3

Polynomial Fitting of Experimental Data

During experimental tests, full displacement fields are recorded using the DIC system discussed earlier. In order to use this data, it needs to be compared to displacement fields obtained in an FE analysis. This comparison requires that all the nodes in both displacement fields are aligned with one another. This can be achieved through interpolation between nodes. To simplify the interpolation process, the data was used to create a polynomial function. Using the FE analysis nodes as inputs to the polynomial function, it can predict the displacements at the same nodes in the experiments, thus aligning the displacement fields. Note that using a lower order polynomial function has the advantage of filtering out numerical noise that may be present within the DIC data. The following section will discuss the specifics regarding each polynomial fit with its respective experimental test.

3.1   Uni-axial Tensile Tests

For the uni-axial tensile tests (method in Chapter 6), the polynomial function was created having three inputs: a X-coordinate, a Y-coordinate and a force value (F). With these three inputs, the X and Y-displacements will be the outputs, respectively. During the uni-axial tensile tests, two different sample geometries were used: rectangular flat strips and dumbbell shaped samples. The effect of using full field displacements (X and Y) vs. only using the longitudinal displacements (Y) was investigated with the rectangular flat strip samples in Appendix A. It was found that using only the Y-displacements were sufficient.

3.1.1   Rectangular Flat Strip Samples

For the rectangular flat strip samples, Figure 3.1 shows the displacement field that was recorded using the DIC system, along with the displacement field used for the polynomial function.
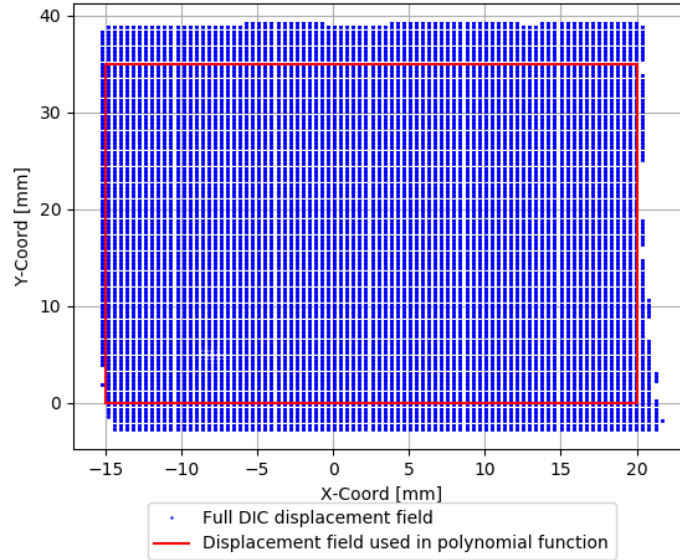
Figure 3.1: Displacement field recorded using DIC for rectangular flat strip sample during uni-axial tensile test.

Using a full second order polynomial (Equation 3.1) to fit the data, the R-squared value was calculated to be 0.999 and an adjusted R-squared also of 0.999, with the number of observation points equal to 164 014.

$$Y_{disp} = C_0 + C_1x + C_2xy + C_3xF + C_4xyF + C_5y + C_6yF + C_7F \\ + C_8x^2 + C_9y^2 + C_{10}F^2 \tag{3.1}$$

A fourth order polynomial function was selected because there are many data points available. It was found that using a fourth order polynomial function (Equation 3.2) was a better fit, with the R-squared value of 1.000 (rounded up from 0.9999) and an adjusted R-squared also of 1.000 (rounded up from 0.9999). Figure 3.2 shows the actual vs. predicted displacement of the fourth order polynomial fit for Y-displacements. A perfect fit is presented by the red line.

$$
\begin{aligned}
Y_{disp} = \ & C_0 + C_1 x + C_2 xy + C_3 xF + C_4 xyF + C_5 y + C_6 yF + C_7 F \\
& + C_8 xy^2 + C_9 Fy^2 + C_{10} yx^2 + C_{11} Fx^2 + C_{12} xF^2 + C_{13} yF^2 \\
& + C_{14} x^2 + C_{15} y^2 + C_{16} F^2 \\
& + C_{17} x^3 + C_{18} y^3 + C_{19} F^3 \\
& + C_{20} x^4 + C_{21} y^4 + C_{22} F^4
\end{aligned} \tag{3.2}
$$
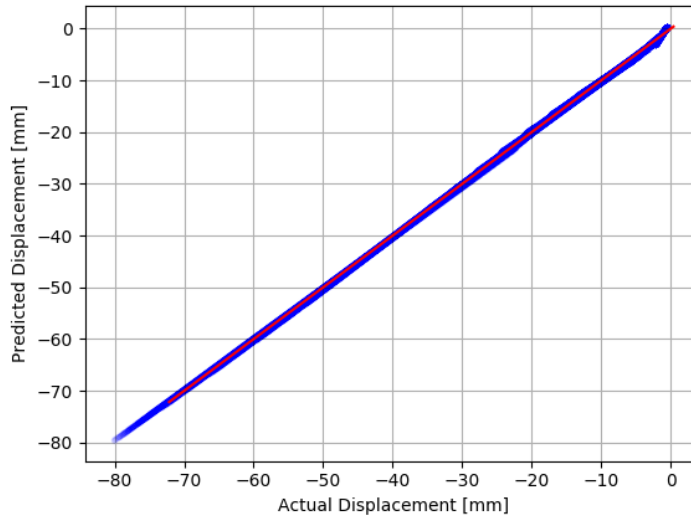
Figure 3.2: Typical fourth order polynomial fit (Y-displacements) for rectangular flat strip samples during uni-axial tensile tests (R-squared = 0.9999).

3.1.2   Dumbbell Shaped Samples

For the dumbbell shaped samples, Figure 3.3 shows the displacement field that was recorded using the DIC system. The displacement field used for the polynomial function is also shown.

Starting with a second order polynomial function (Equation 3.1), an R-squared value of 0.999 and an adjusted R-squared value of 0.999 were found. Using a fourth order polynomial function (Equation 3.2) an R-squared value of 1.000 (rounded up from 0.9999) and an adjusted R-squared value of 1.000 (rounded up from 0.9999) were found. This is a better fit, with a total number of observations equal to 19 656. Figure 3.4 shows the actual vs. predicted Y-displacements of the fourth order polynomial fit. A perfect fit is presented by the red line.
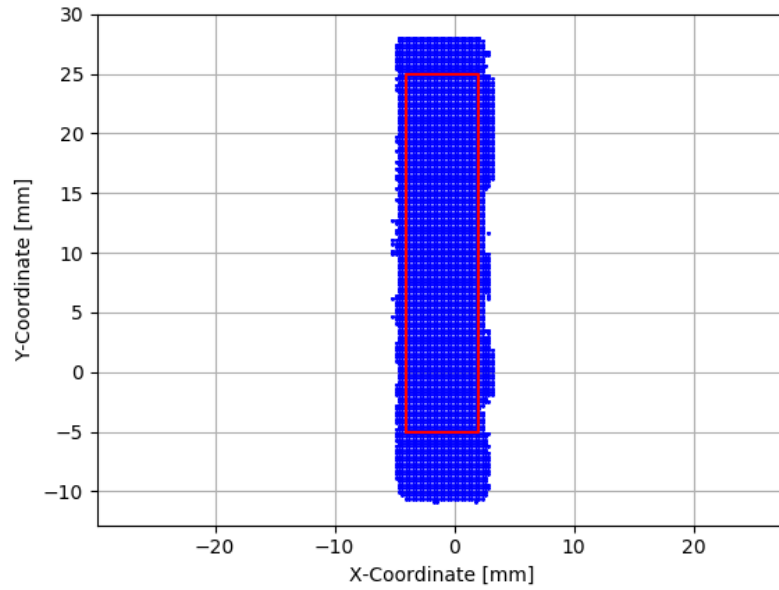
Figure 3.3: Displacement field recorded using DIC for dumbbell shaped sample during uni-axial tensile test.
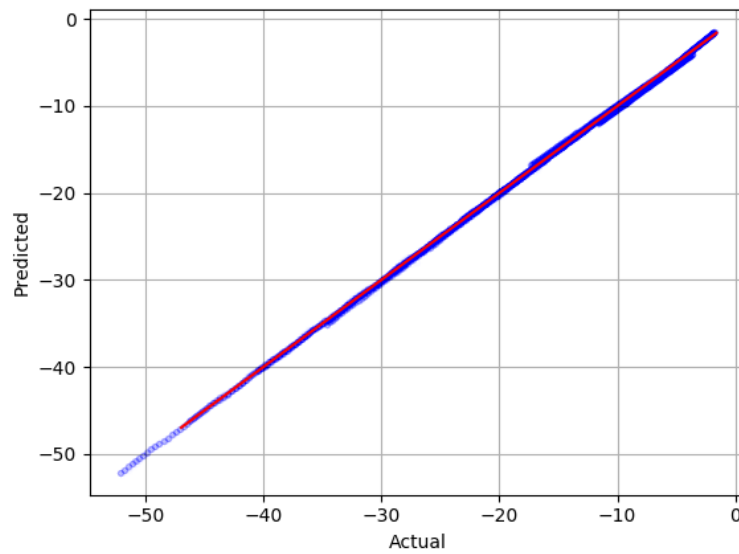
Figure 3.4: Typical fourth order polynomial fit for dumbbell shaped samples during uni-axial tensile tests (R-squared = 0.9999).

3.2   Bi-axial Bubble Inflation Tests

For the bi-axial bubble inflation tests (method in Chapter 7), polynomial functions were created as before, having three inputs: a X-coordinate, a Y-coordinate and a pressure value (P). With these three inputs, the Z-displacements (perpendicular to membrane surface), the X-displacements and the Y-displacements will each be approximated separately. Figure 3.5 shows the displacement field that was recorded using the DIC system, along with the displacement field used for the polynomial function.

It was found that using a fourth order polynomial function (Equation 3.2) was a good fit, with the R-squared value of 0.998, with a total number of observation points equal to 106 357. Figure 3.6 shows the actual vs. predicted displacement of the fourth order polynomial fit for Z-displacements. A perfect fit is presented by the red line.
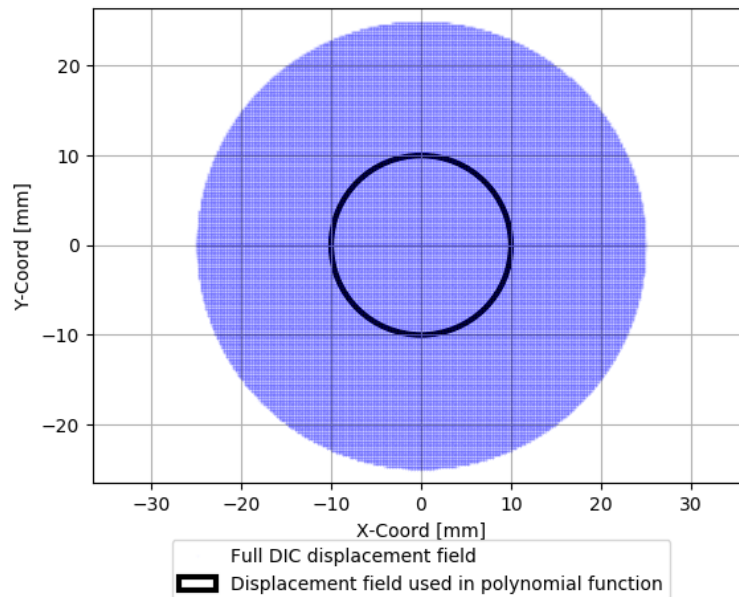
Figure 3.5: Displacement field recorded using DIC for bi-axial bubble inflation tests.

Typical actual vs. predicted displacement graphs for the X-displacements and Y-displacements can be found in Appendix B along with graphs to show that the bubble deforms symmetrically in the X- and Y-direction.
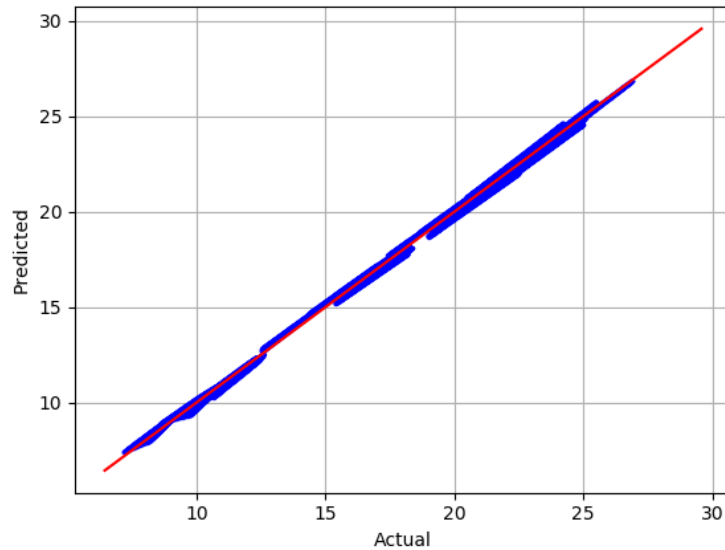
Figure 3.6: Typical fourth order polynomial fit for Z-displacement obtained from bi-axial bubble inflation tests (R-squared = 0.998).

3.3   Unconstrained Uni-axial Compression Test

For the unconstrained uni-axial compression samples (method in Chapter 8), Figure 3.7 shows the displacement field that was recorded using the DIC system, along with the displacement field used for the polynomial function (red).

Using a fourth order polynomial function (Equation 3.2), an R-squared value of 1.000 (rounded up from 0.9999) and an adjusted R-squared value of 1.000 (rounded up from 0.9999) was found. The total number of observation points was equal to 52 668. Figure 3.8 shows the actual vs. predicted Y-displacements of the fourth order polynomial fit. A perfect fit is presented by the red line. In this thesis all the polynomial functions will be used as the experimental data during the inverse FE model updating methods of the respective tests.
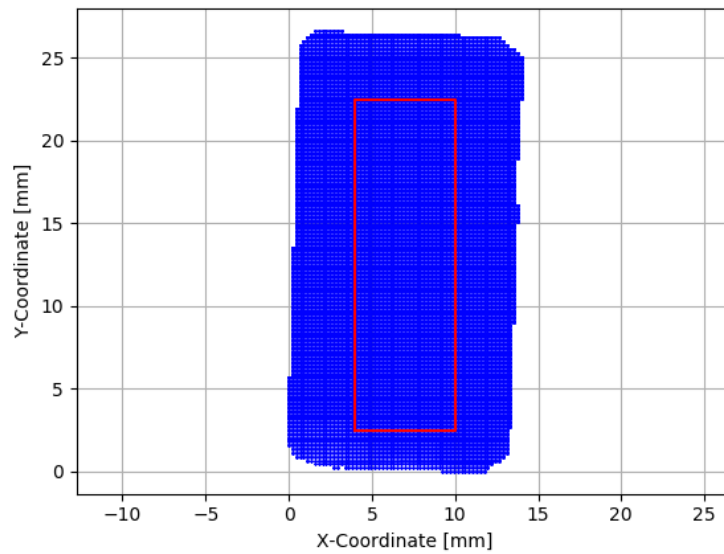
Figure 3.7: Displacement field recorded using DIC for unconstrained uni-axial compression test samples.
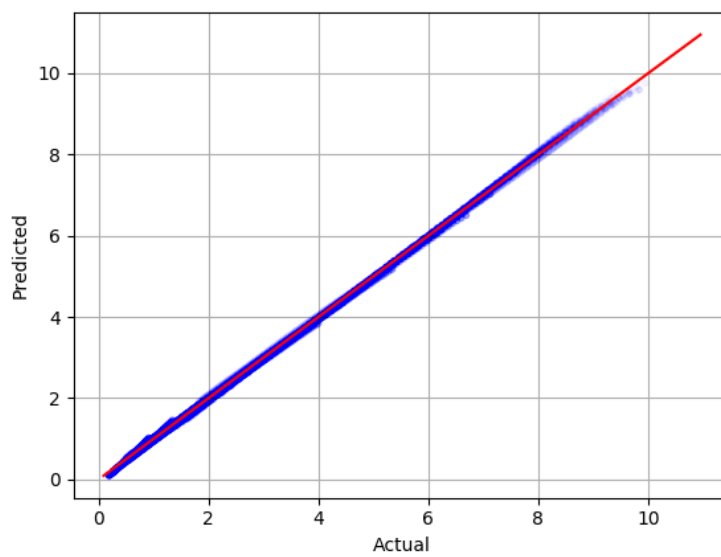
Figure 3.8: Typical fourth order polynomial fit for unconstrained uni-axial compression test samples (R-squared = 0.9999).

Chapter 4

Relative Displacement Fields

The relative displacement fields method was only used on rectangular flat strip samples during uni-axial tensile tests. When performing experimental uni-axial tensile tests, the DIC system captures absolute displacement fields. If slippage occurs during the test, it is also captured as artificial displacements. When using the inverse FE model updating method, where one compares the DIC and FEM displacement fields, these artificial displacements will result in an inaccurate material model. If slippage is assumed to add a uniform component to the measured displacement field, a relative displacement field can be calculated to compensate for slippage. This is similar to removing a rigid body mode from the data. This relative displacement field was calculated using a reference node, specified by the user, and calculating all displacements of other nodes relative to that node.

To prove the assumption that slippage is uniform, Figure 4.1 shows a row of nodes with the same original Y-coordinate (30.872 mm as can be seen in Figure 3.1) with respect to their displacement from this coordinate over the duration of a uni-axial tensile test. Figure 4.2 is for a Y-coordinate of 10.976 mm. The black line represents the mean value of the row of nodes, which is horizontal. For slip to be uniform, the nodes should be on the black line. It can be seen that little deviation occurs between the nodes and the horizontal mean with a maximum standard deviation of 0.27 mm. This maximum standard deviation is small compared to the maximum node displacement of 47 mm, thus the assumption that the slip is uniform holds true.

A sensitivity study was conducted, using seven different reference nodes chosen at random, to calculate the relative displacement field, and then calculating the material properties. Figure 4.3 shows the seven different reference nodes within the boundaries of the full displacement field used during uni-axial tensile tests (rectangular flat strip samples). Figure 4.4 shows a engineering stress-stretch graph showing the difference between using absolute displacement and relative displacement fields. It can be observed that there exists a
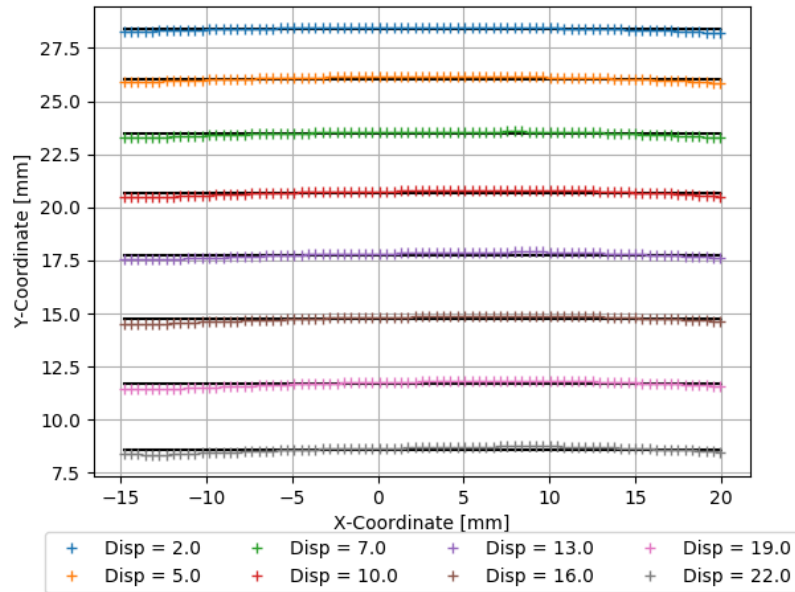
Figure 4.1: A row of nodes with the same original Y-coordinate (30.872 mm) with respect to their Y-displacement over the duration of a uni-axial tensile test.
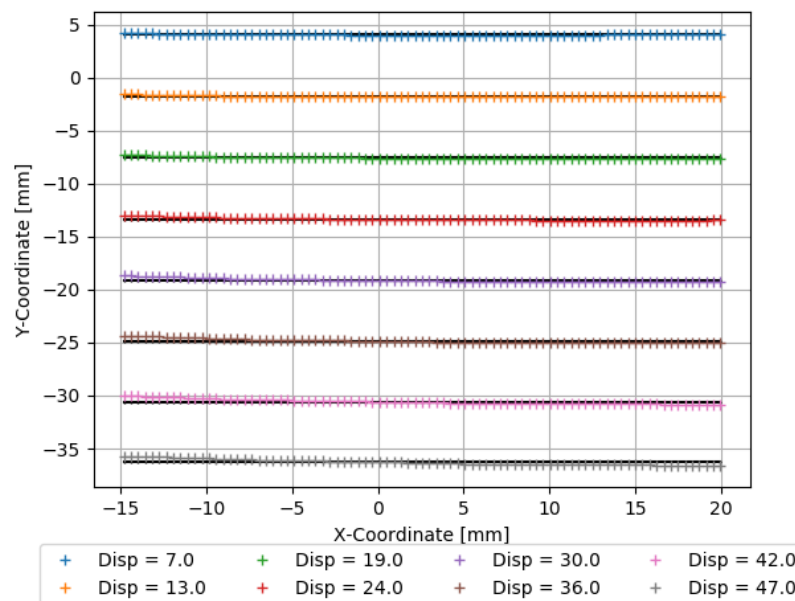
Figure 4.2: A row of nodes with the same original Y-coordinate (10.976 mm) with respect to their Y-displacement over the duration of a uni-axial tensile test.

small, yet negligible error between using different relative nodes, when calculating the relative displacement field. It can thus be concluded that this is a viable method to compensate for slippage happening during uni-axial tensile tests for the rectangular flat strip samples.
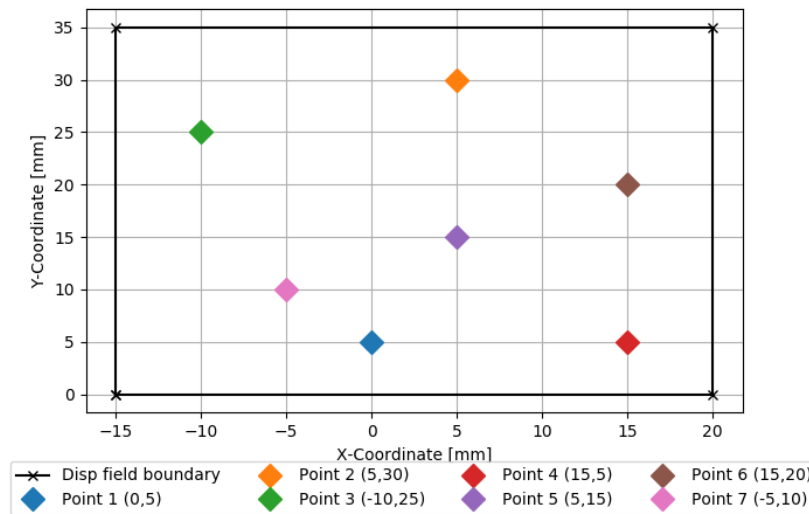
Figure 4.3: Seven Different relative points within the boundaries of the displacement field.
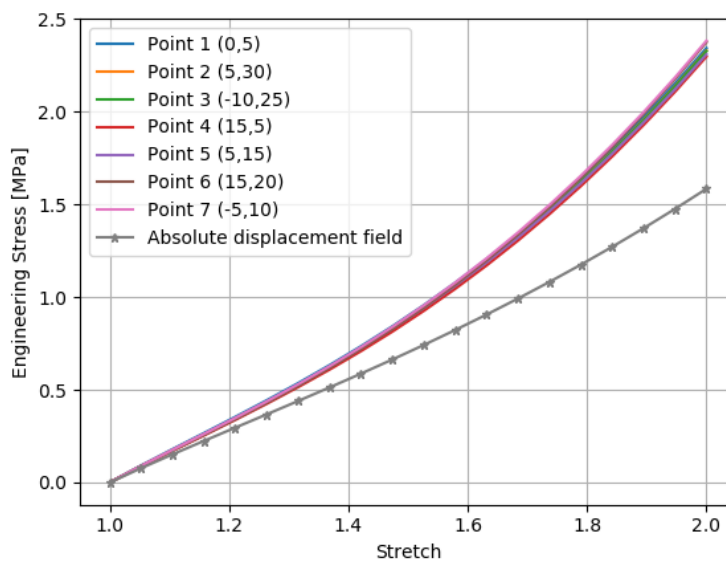
Figure 4.4: Engineering stress-stretch comparison graph of using absolute displacement and relative displacement fields. Seven different relative points were selected to calculate seven different relative displacement fields.

Chapter 5

Moulding Process

This chapter will first discuss various moulding processes found in literature. Then it will end with a discussion on the moulding process that was followed in this thesis.

Meunier *et al.* (2008) used a silicone-rubber produced by Rhodia (RTV 141). Samples were produced by mixing the two liquid parts (uncured silicone and mixing agent) with a 10:1 ratio. The mixture was then put under vacuum for 30 min to eliminate entrapped bubbles. There after, the mixture was injected into moulds and left in an oven at 70 °C for 150 min to cure.

Rey *et al.* (2013) investigated the effects of temperature on the mechanical properties of silicone-rubbers. Two silicone-rubbers were used, Bluestar RTV 141 and RTV 3428. The silicone was mixed with 10:1 weight ratio of the curing agent. There after the mixture was placed under vacuum for 30 min. The degassed mixture was injected into moulds with a medical syringe. The moulds were placed in an oven at 70 °C for 4 hours to cure.

Case *et al.* (2015) characterised three silicone-rubbers, one of which was Smooth-Sil 950. The two parts were mixed using a centrifugal mixer. Then the uncured liquid silicone-rubber was spun onto a glass slide at 400 RPM for 60 s to obtain a constant thickness membrane (0.643 mm). The membranes were left in an oven overnight at 60 °C to cure.

Using these studies as guide, the following moulding process was developed for this thesis. The silicone-rubber used in this thesis (Smooth-Sil 950) was moulded, by mixing part A (uncured silicone and white) with part B (curing agent and blue) with a weight ratio of 10:1 respectively. A Kern EMB 600-2 scale was used to measure the weight of each component, with an accuracy of 0.6 % as calculated in Appendix C. The mixture was poured into a foam cup, and mixed by hand until the colour was consistent throughout. Next, it was poured into the various sample moulds and placed on a level surface.

A straight edge was used to even out the top surface relative to the mould surface, to ensure a constant thickness within the samples.

The mould to cast the membranes for the bubble inflation test was milled (depth of 2 mm) from an aluminium plate. The rectangular flat strip samples were cut from a bubble inflation membrane. For the dumbbell shaped and validation test samples, 3D printed moulds were used, also with a depth of 2 mm. The moulds for the uni-axial compression cylindrical samples were made by glueing plastic round fittings onto a plastic plate. Figure 5.1 shows the different kinds of samples that were used in this thesis.
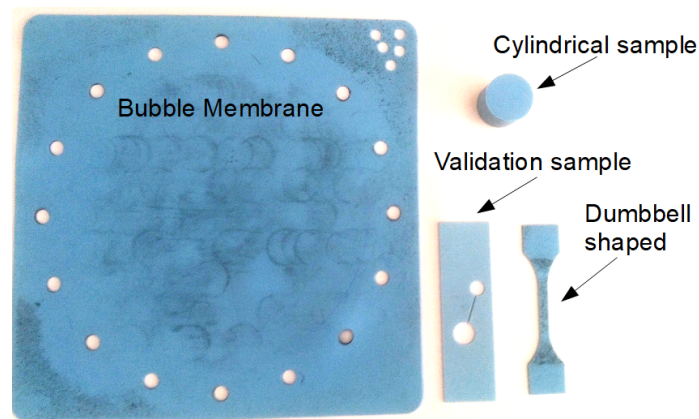
Figure 5.1: Different kinds of samples used within this thesis.

The mould plate used for the bubble inflation test membranes was too large (500 mm × 500 mm) for the vacuum chamber and oven facilities available. This restricted the moulding process to be left at ambient temperature, with no vacuum and a curing time of 24 hours. It was noted that while the sample was left to cure, over time bubbles would escape on their own, this can be explained due to how thin the membrane is ($\approx$ 2 mm). The samples for the uni-axial compression test were placed under vacuum for 30 min, this is because the sample is thick, and not regarded as a membrane. It is thus harder for entrapped bubbles to escape on their own. To further investigate the effect of vacuum and curing temperature, a study was conducted using the dumbbell shaped samples. The results of this study can be found in Chapter 6. Three types of samples were made:

1. Cured over 24 hours at ambient temperature with no vacuum.

2. Cured over 24 hours at ambient temperature with 30 min of vacuum.

3. Vacuumed for 30 min, then cured in an oven at 70 °C for 3 hours.

Chapter 6

Uni-axial Tensile Tests

The uni-axial tensile test is the most common test to use when determining hyper-elastic material properties. The following chapter will discuss various topics which include: the test method used during testing, a presentation of the results obtained, a moulding process and strain rate sensitivity study, results obtained from the direct identification method and the inverse FE model updating method and a sensitivity study on the material models' constants.

6.1 Uni-axial Tensile Test Method

Uni-axial tensile tests were done on an MTS Criterion 44 universal testing machine, using a 1 kN load cell and standard MTS grips. The load cell was calibrated using standard engineering calibration weights because the actual load measured during tests were relatively small compared to the load cell's range. The results of the calibration (Appendix D) was a measurement error of 0.996 % with a repeatability of 0.416 %. Testing was conducted at ambient temperature.

Two different types of samples were tested: rectangular flat strips and dumbbell shaped. The dumbbell shape was according to the ISO 527-2 standard. Figure 6.1 shows a schematic of the specimens, with the initial gauge length (l_0), gauge width (w_0) and gauge thickness (t_0).

6.1.1 Different Inverse FE Model Updating Methods

For the inverse FE model updating method, an FE model was created for each geometry. The boundary conditions for each FE model are also different. For the rectangular flat strip samples, it was decided to match the displacement fields of the FE analysis with the experimental data, using the reaction force as the boundary condition. The dumbbell shaped samples used the edge dis-

32
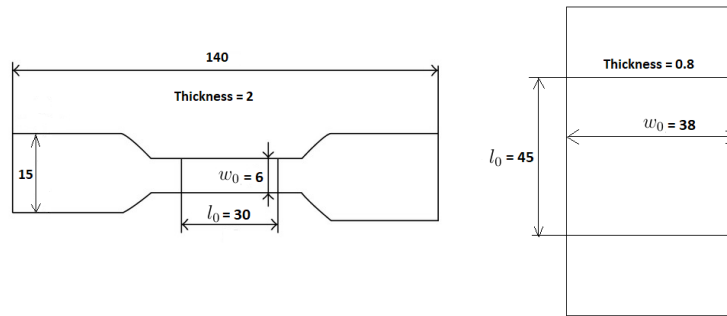
Figure 6.1: Uni-axial tensile test samples. Measurements in mm.

placements as boundary conditions, and matched the reaction force of the FE analysis with the experimental data. The results for both inverse methods can be found in the next section.

Figure 6.2a shows the mesh that was used for the rectangular flat strip samples. A smaller mesh was chosen to eliminate potential errors at the boundaries in the experimental data. The coordinates of the mesh nodes were chosen to correlate with the ones obtained from the DIC displacement fields. The mesh consisted of 1 710 Quad-4 elements, the number of elements were chosen so that one element is approximately 1 mm $\times$ 1 mm. An FE mesh refinement study can be found in Appendix F. Boundary conditions for the FE model can also be seen in Figure 6.2a, which are fully constrained at the top, to simulate a fixed clamp and an edge load at the bottom along with a constraint in the X-direction to simulate a clamp pulling down on the sample.

Figure 6.2b shows the FE mesh used for the dumbbell shaped samples, 60 Quad-4 elements were used (Appendix G shows an FE mesh refinement study). The boundary conditions can also be seen. Assuming that the nodes at the top and bottom boundaries deform linearly in the Y-direction with respect to one another, the boundary conditions for the dumbbell shaped samples were as follows:

1. A non-zero prescribed displacement in the Y-direction for the top 5 nodes.

2. A non-zero prescribed displacement in the Y-direction for the bottom 5 nodes.

3. A zero displacement constraint in the X-direction for the middle node in the top and bottom.

The fixed Y-direction displacement correlates with displacements obtained from test data. With these boundary conditions, the reaction force was determined and compared to the experimental data. For the inverse FE model

updating method, the difference in reaction force was minimised.

(a) Rectangular flat strip samples.

(b) Dumbbell shaped samples.
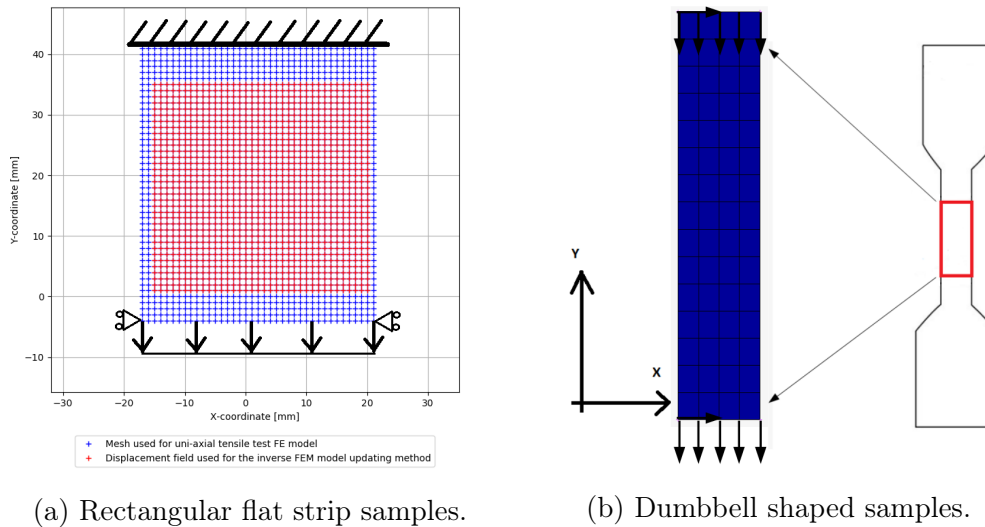
Figure 6.2: Different FE models used for the inverse FE model updating method during uni-axial tensile tests.

6.2 Uni-axial Tensile Test Experimental Results

As stated above, two types of samples were tested. Four samples of each geometry were tested. Table 6.1 shows the standard deviation of stretch and correlation of stretch within each geometry, as well as both geometries together. Figure 6.3 shows the average of each geometry with error bars of one standard deviation of stretch. It can be observed that there exists a difference between the curve shape of each geometry, with a maximum error of stretch equal to 2.33 %. The rectangular flat strip samples have a more concave downward profile, while the dumbbell shaped samples have a more concave upward profile. Combining both geometries resulted in an average engineering stress-stretch curve for uni-axial tensile test data. This average engineering stress-stretch curve was used in Chapter 9 and Chapter 10.

6.3 Moulding Process Study

As discussed in the previous chapter, the effect that vacuum and curing temperature has on the material's properties was investigated using the dumbbell

Table 6.1: Comparison of standard deviation and correlation of stretch between rectangular flat strip and dumbbell shaped samples.

	STD of stretch	Correlation of stretch
Rectangular flat strip	0.0112	0.9989
Dumbbell shaped	0.0294	0.9939
Average uni-axial tensile	0.0203	0.9967
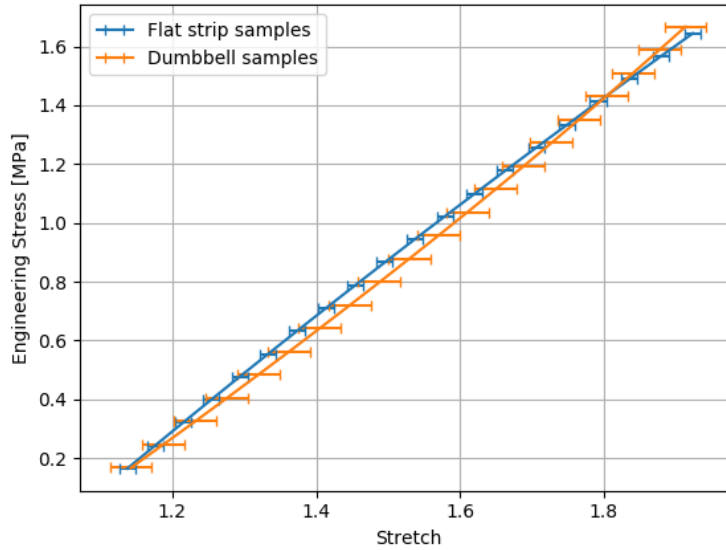
Figure 6.3: Average engineering stress vs. stretch graph with one standard deviation error bars for rectangular flat strip and dumbbell shaped samples.

samples. Figure 6.4 shows the avergae engineering stress-stretch graphs of the three different moulding processes, with one standard deviation error bars. Four samples were tested for each moulding process. It can be observed that when the material is not vacuumed and left to cure at ambient temperature, the material shows a possible trend to become more stiff as the stretch increases.

For consistency, all samples (except the compression cylindrical samples) that were used to determine material models were made using the same moulding process. This was using no vacuum and curing at ambient temperature for 24 hours.
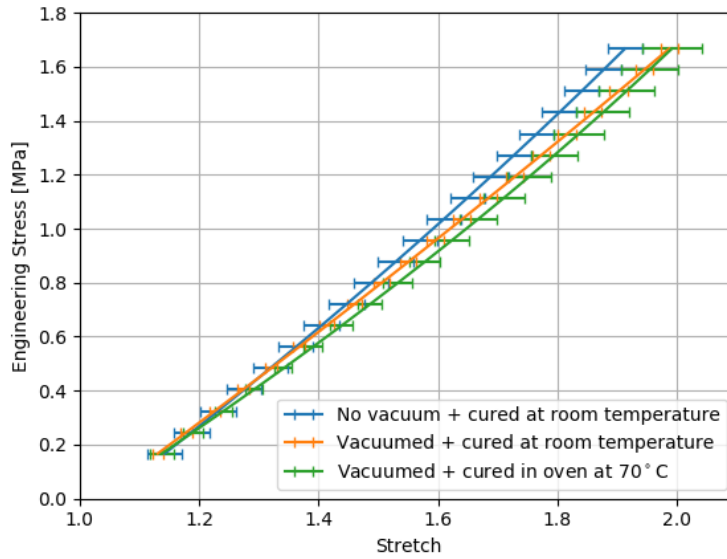
Figure 6.4: Average engineering stress vs. stretch graph for the different moulding processes for dumbbell samples. One standard deviation error bars are also shown.

6.4   Strain-rate Sensitivity Study

A strain-rate sensitivity study was also conducted using the dumbbell samples. Taking the gauge length of the samples to be 75 mm, three different strain rates were tested:

1. 450^{-1} s^{-1} or 10 mm/min.

2. 45^{-1} s^{-1} or 100 mm/min.

3. 9^{-1} s^{-1} or 500 mm/min.

Four samples were tested for each strain rate. Figure 6.5 shows the average engineering stress-stretch graphs of the three strain rates, with one standard deviation error bars. It can be observed that at a low (10 mm/min) to medium (100 mm/min) strain rate, there is a good correlation between the data. When the strain rate is high (500 mm/min), the curve shows a trend to be slightly more non-linear. A possible explanation for this can be that the material exhibits strain hardening when subjected to a high strain rate. This result correlates well with the result obtained from Meunier *et al.* (2008), who reported that silicone-rubber (RTV 141) shows no strain-rate dependency when the strain-rate is below 10^{-1} s^{-1} or 450 mm/min.

For consistency within this thesis, all data that was used for the determination of material models were tested at a medium to low strain rate. Uni-axial
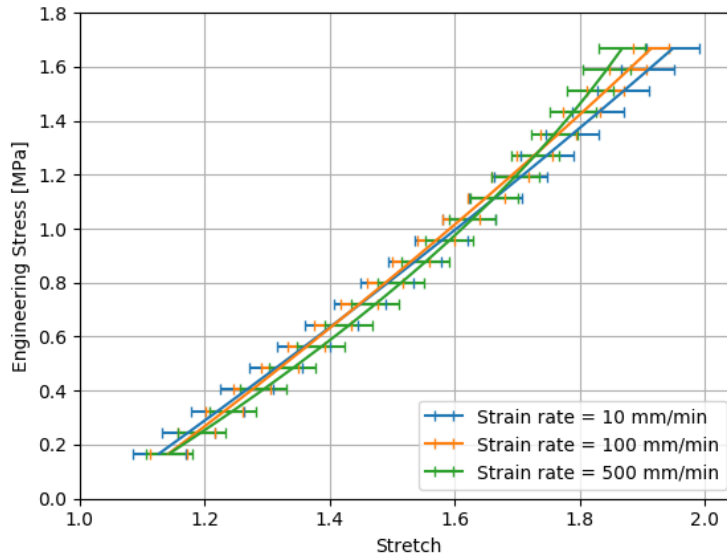
Figure 6.5: Average engineering stress vs. stretch graph for different strain rates for dumbbell samples. One standard deviation error bars are also shown.

tensile and uni-axial compression tests were done with a strain rate of 45^{-1} s^{-1} or 100 mm/min.

6.5   Direct Identification Method Results

The direct method is the more traditional method to determine hyper-elastic material properties. The mechanical behaviour of rubber like materials can be determined if the deformation modes are simple like an uni-axial tension or equi-bi-axial tension. The experimental test data is used to calculate stress-stretch data. With this data, the material model constants can be calculated by means of a least squares fit procedure(Rachik *et al.*, 2001). This section will present the material models obtained using the direct method for uni-axial tensile tests.

6.5.1   Mooney-Rivlin Two Parameter Model

To derive the stress-stretch relationship for the uni-axial tensile test, a cubic volume element is considered under an uni-axial tensile stress (σ), as can be seen in Figure 6.6. If the stretch is parallel to the uni-axial tensile stress, the following stretch deformations are derived:
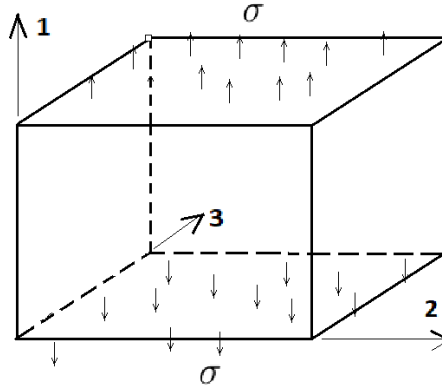
Figure 6.6: Cubic differential volume element within Cartesian coordinate system.

$$\lambda_1 = \lambda$$
$$\lambda_2 = \lambda_3 = \frac{1}{\sqrt{\lambda}} \tag{6.1}$$

Substituting Equation 6.1 into Equation 2.10, the strain invariants for an incompressible material in uni-axial tension are:

$$I_1 = \lambda^2 + 2\lambda^{-1}$$
$$I_2 = \lambda^{-2} + 2\lambda \tag{6.2}$$

The relationship between engineering stress and stretch for an incompressible material under uni-axial tension is (Rivlin, 1948):

$$\sigma_e = 2\left(\lambda - \lambda^{-2}\right)\left(\frac{\partial W}{\partial I_1} + \frac{1}{\lambda}\frac{\partial W}{\partial I_2}\right) \tag{6.3}$$

Inserting Equation 2.13 into Equation 6.3, the following equation is obtained:

$$\sigma_e(\lambda) = 2C_{10}\left(\lambda - \frac{1}{\lambda^2}\right) + 2C_{01}\left(1 - \frac{1}{\lambda^3}\right) \tag{6.4}$$

This equation was used during the least squares fit to determine the material model constants C_{10} and C_{01}. These constants govern the Mooney-Rivlin 2-parameter model and can be found in Table 6.2. Figure 6.7a shows the two material models obtained from the rectangular flat strip and dumbbell shaped samples.

Figure 6.7a shows a good fit between the material models obtained and the respective test data. However, when extrapolating the material model into the compression region (below a stretch equal to one), it can be observed that the model predicts infeasible material behaviour. Feasible material behaviour would be a non-linear increase of compression stress as stretch decreases. When

Table 6.2: Results obtained using the direct method for the Mooney-Rivlin two parameter model on uni-axial tensile tests.

	C_{10} [Pa]	C_{01} [Pa]
Rectangular flat strip	817694.34	-621784.68
Dumbbell shaped	894939.06	-737925.57

(a) No constraints.

(b) Positive constant constraints.
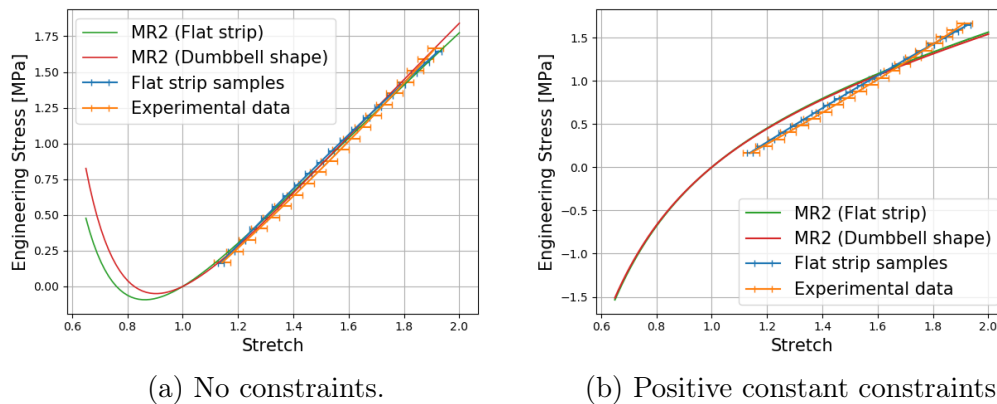
Figure 6.7: Mooney-Rivlin two parameter models calculated using the direct method on uni-axial tensile tests.

these material models were used within an FE model, the result was a failed analysis, due the determinant of the stiffness matrix becoming zero or negative. A reason may be due to the strain state being in a region where the input data for the strain energy function is invalid. Thus using a hyper-elastic material model in a simple uni-axial tensile FE model, will result in a complex stress state. To solve this problem, constraints were introduced, where both parameters were forced to be positive (Gent, 2012). Table 6.3 shows the Mooney-Rivlin two parameter model obtained incorporating the positive constant constraints. Figure 6.7b shows the engineering stress-stretch graph for the the Mooney-Rivlin two parameter model constants obtained incorporating the positive constant constraint. It can be observed that logical material behaviour are being predicted in the compression region. However, the material model shows a poor fit to the experimental data. The need for additional user input constraints can be seen as a disadvantage when using the direct method to determine hyper-elastic material models.

6.5.2 Mooney-Rivlin Three Parameter Model

The engineering stress-stretch relationship for the Mooney-Rivlin three parameter model (Equation 6.5) can be derived from Equation 2.14 using the same steps as for the two parameter Mooney-Rivlin model.

Table 6.3: Results obtained using the direct method for the Mooney-Rivlin two parameter model on uni-axial tensile tests (positive constant constraints).

	C_{10} [Pa]	C_{01} [Pa]
Rectangular flat strip	446491.45	0.0
Dumbbell shaped	440141.19	0.0

$$
\begin{aligned}
\sigma_e(\lambda) =& 2C_{10}\left(\lambda - \frac{1}{\lambda^2}\right) + 2C_{01}\left(1 - \frac{1}{\lambda^3}\right) \\
& + 4C_{20}\left(\lambda - \frac{1}{\lambda^2}\right)\left(\lambda^2 + \frac{2}{\lambda} - 3\right)
\end{aligned}
\tag{6.5}
$$

Using the above equation the material constants were determined as described for the Mooney-Rivlin two parameter model. The material constants that govern the Mooney-Rivlin three parameter material model can be found in Table 6.4. Figure 6.8a shows the two material models obtained from the rectangular flat strip and dumbbell shaped samples.

Table 6.4: Results obtained using the direct method for the Mooney-Rivlin three parameter model on uni-axial tensile tests.

	C_{10} [Pa]	C_{01} [Pa]	C_{20} [Pa]
Rectangular flat strip	800010.50	-599005.05	1824.24
Dumbbell shaped	784574.16	-597372.13	11921.4

Figure 6.8a shows a good fit between the material models obtained and the respective test data. However, as in the previous subsection, when extrapolating the material models into the compression region, it can be observed that the material models predict infeasible material behaviour. Using the obtained material models in an FE analysis, will once again result in a failed analysis as discussed before. To solve the problem, positive constant constraints were once again introduced (Gent, 2012). Figure 6.8b shows the Mooney-Rivlin three parameter models obtained incorporating the positive constant constraints. A good correlation can be seen between the material models and their respective experimental data and both predict feasible material behaviour. The Mooney-Rivlin three parameter model constants obtained incorporating the positive constant constraints can be found in Table 6.5.

While the material models obtained from the direct method with positive constant constraints gave a good prediction of the uni-axial tensile data as well as predicted feasible material behaviour, the need for additional user input constraints were once again required.

(a) No constraints.   (b) Positive constant constraints.
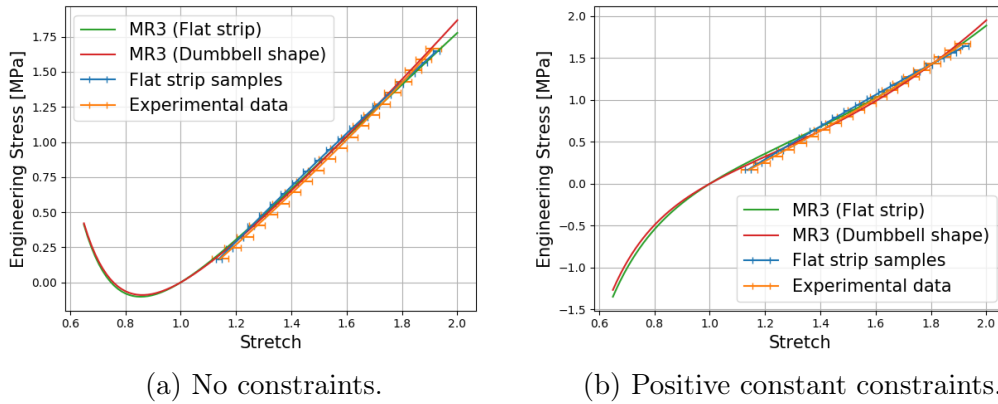
Figure 6.8: Mooney-Rivlin three parameter models calculated using the direct method on uni-axial tensile tests.

Table 6.5: Results obtained using the direct method for the Mooney-Rivlin three parameter model on uni-axial tensile tests (positive constant constraints).

	C_{10} [Pa]	C_{01} [Pa]	C_{20} [Pa]
Rectangular flat strip	343879.29	0.0	48820.41
Dumbbell shaped	306269.50	0.0	62791.08

6.5.3   Ogden Three Parameter Model

To derive the constitutive equation for the strain energy (W) based on principal stretches, Equation 6.1 is inserted into Equation 2.15, which yields the following equation:

$$W(\lambda) = \sum_{i=1}^{N} \frac{\mu_i}{\alpha_i} \left(\lambda^{\alpha_i} + 2\lambda^{\frac{1}{2}\alpha_i} - 3 \right) \tag{6.6}$$

Rackl (2015) stated that the stress-stretch relationship for uni-axial tension can be obtained by deriving the strain energy with respect to the stretch:

$$\sigma(\lambda) = \frac{\partial W(\lambda)}{\partial \lambda} \tag{6.7}$$

Using Equation 6.6 and Equation 6.7, the engineering stress-stretch equation used during the least squares fit, can be determined:

$$\sigma(\lambda) = \sum_{i=1}^{N} \mu_i \left(\lambda^{\alpha_i - 1} - \lambda^{-(\frac{1}{2}\alpha_i + 1)} \right), \quad N = 3 \tag{6.8}$$

The traditional Ogden model (three parameters, and six unknowns) was used, this is when $N = 3$. The results for the Ogden three parameter

model, determined by the direct method, can be seen in Table 6.6. It can be observed that the constants and exponents only differ slightly or are the same. A reason for this is that the initial guess for constants and exponents in the least squares fit were also the same. Thus it can be concluded that the Ogden model works by the relationship between its parameters, with each parameter carrying equal weight. Figure 6.9 shows the two material models obtained from the rectangular flat strip and dumbbell shaped samples.

Table 6.6: Results obtained using the direct method for the Ogden three parameter model on uni-axial tensile tests.

	μ_1 [Pa]	α_1	μ_2 [Pa]	α_2	μ_3 [Pa]	α_3
Rect. flat strip	123310.73	3.318	124394.06	3.318	132194.86	3.318
Dumbbell shaped	103477.75	3.635	103477.72	3.635	115523.91	3.635
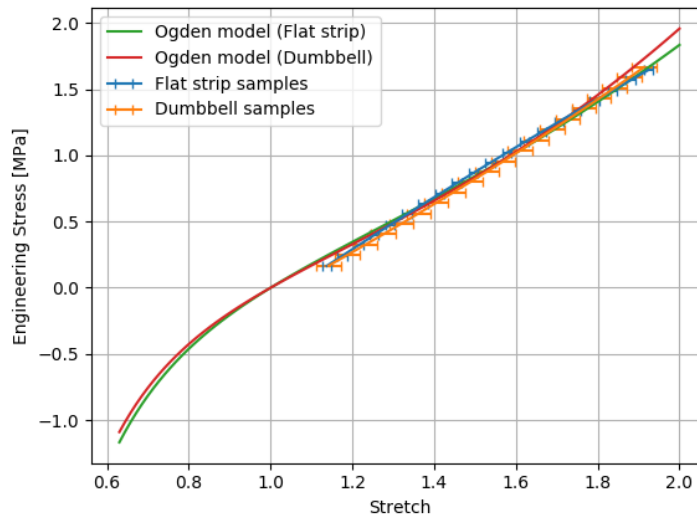
Figure 6.9: Ogden three parameter model using the direct method on uni-axial tensile tests.

It can be observed in Figure 6.9 that when extrapolating the material models into the compression region, that the material models predict feasible material behaviour. These material models will result in a successful FE analysis.

6.6   Inverse FE Model Updating Method Results

This section will present the material models obtained using the inverse FE model updating method. The procedures followed can be found in Chapter 2 and in the beginning of this chapter.

6.6.1   Mooney-Rivlin Two Parameter Model

Using Equation 6.4 as the material model in the FE analyses, the material constants were determined with numerical optimisation using no constraints, however the initial parameters for the numerical optimisation should result in a successful FE analysis. Initial parameters were found in literature (Sasso *et al.* (2008) and Rachik *et al.* (2001)). Table 6.7 shows the material constants obtained and Figure 6.10 shows the two material models obtained from the rectangular flat strip and dumbbell shaped samples.

Table 6.7: Results obtained using the inverse FEM model updating method for the Mooney-Rivlin two parameter model on uni-axial tensile tests.

	C_{10} [Pa]	C_{01} [Pa]
Rectangular flat strip	484489.36	-91966.76
Dumbbell shaped	530716.68	-143162.94
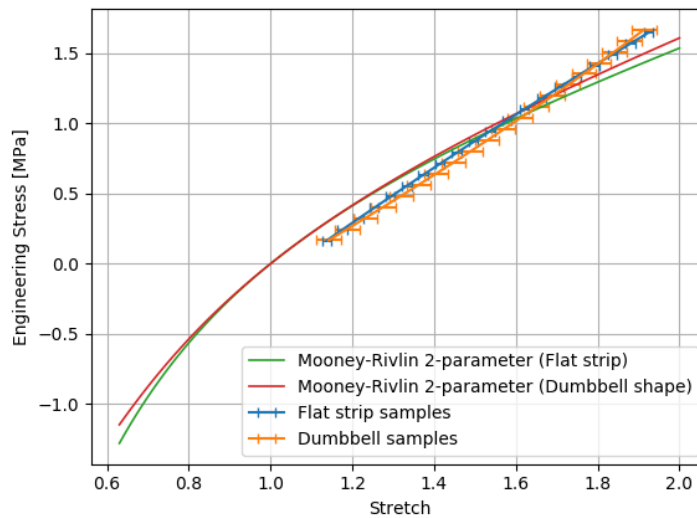
Figure 6.10: Mooney-Rivlin two parameter model calculated using the inverse FEM model updating method on uni-axial tensile tests.

Figure 6.10 shows that the material models obtained does not have a good fit to the experimental test data. However, when extrapolation the material model into the compression region, it can be seen that the material models predict feasible material behaviour, which are similar in shape of the material models obtained using the direct method with positive constant constraints. Using the inverse method to obtain Mooney-Rivlin two parameter models is an improvement over the direct method, for no constraints were required if the initial parameters resulted in a successful FE analysis. No further work was done on the Mooney-Rivlin two parameter model because the three parameter model predicted the material's behaviour better.

6.6.2 Mooney-Rivlin Three Parameter Model

Equation 6.5 was used as the material model in the FE analyses. The material constants that govern the Mooney-Rivlin three parameter material model were determined as discussed before and can be found in Table 6.8. Note the fundamental difference of the C_{01} term between the two samples. Figure 6.11 shows the two material models obtained from the rectangular flat strip and dumbbell shaped samples. It can be observed, that although the C_{01} constants differ, both material models predict similar material behaviour. A reason for this is that the C_{01} constant in a Mooney-Rivlin three parameter model are responsible for either a concave upward (flat strip) profile or a concave downward (dumbbell) profile.

Table 6.8: Results obtained using the inverse FEM model updating method for the Mooney-Rivlin three parameter model on uni-axial tensile tests.

	C_{10} [Pa]	C_{01} [Pa]	C_{11} [Pa]
Rectangular flat strip	315571.10	-5931.41	66929.04
Dumbbell shaped	297328.77	10533.75	59147.33

As seen before, when extrapolation the material models into the compression region, it can be seen in Figure 6.11 that the models predicts feasible material behaviour. This will also result in a successful FE analysis when these material models are used in an FE model.

6.6.3 Ogden Three Parameter Model

Equation 6.8 with $N = 3$ was used as the material model in the FE analyses. Table 6.9 shows the material model constants obtained as previously discussed, that govern the Ogden three parameter material model. The parameters can be seen to be the same or only differ slightly within each material model. The reason for this is as discussed before. However, the two material models obtained are different, but they both have a good fit to the experimental data.
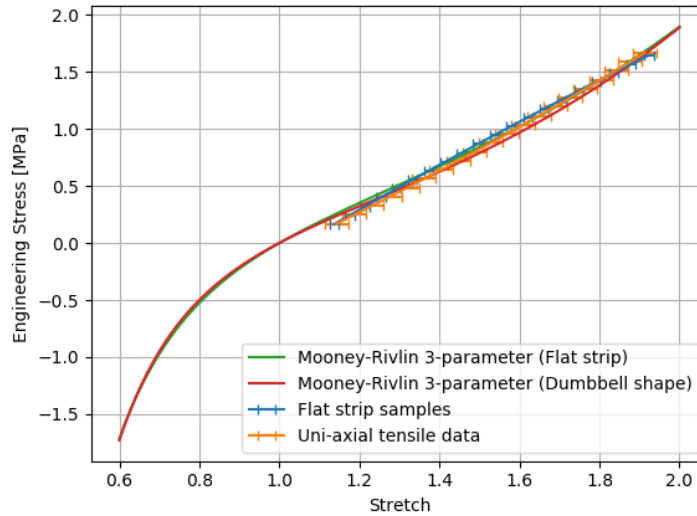
Figure 6.11: Mooney-Rivlin three parameter model calculated using the inverse FEM model updating method on uni-axial tensile tests.

It Figure 6.12 shows the two material models obtained from the rectangular flat strip and dumbbell shaped samples.

Table 6.9: Results obtained using the inverse FEM model updating method for the Ogden three parameter model on uni-axial tensile tests.

	μ_1 [Pa]	α_1	μ_2 [Pa]	α_2	μ_3 [Pa]	α_3
Rect. flat strip	30397.64	3.303	45686.86	3.312	297519.42	3.312
Dumbbell shaped	100000.01	3.667	100000.01	3.667	100000.01	3.667

It can be observed in Figure 6.12 that the material models obtained shows a good fit to the respective test data. When extrapolating the material models into the compression region, the models predicts feasible material behaviour, and will result in a successful FE analysis.

6.7   Material Models Obtained for Dumbbell Shaped Samples

In this section the Mooney-Rivlin three parameter and Ogden three parameter models obtained from both the direct and inverse FE model updating methods will be shown on one graph (Figure 6.13). Only the dumbbell shaped samples were chosen, because the material models obtained were similar to that of the rectangular flat strip samples. Thus the conclusions that can be drawn for
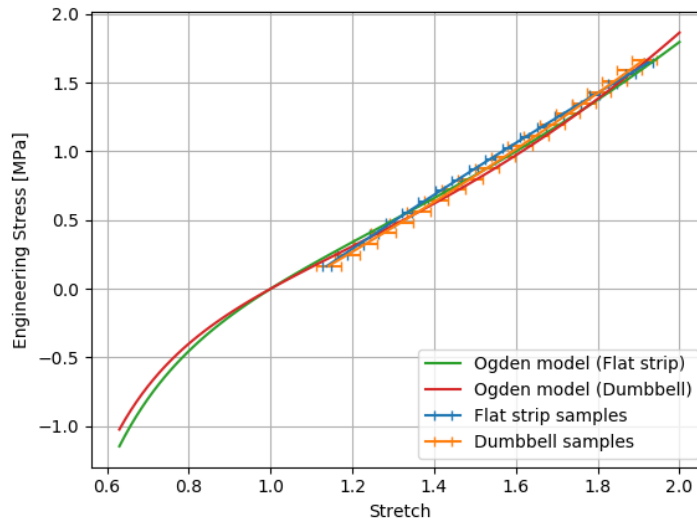
Figure 6.12: Ogden three parameter model using the inverse FEM model updating method on uni-axial tensile tests.

the dumbbell shaped samples can also be drawn for the rectangular flat strip samples. It can be observed in Figure 6.13 that the Mooney-Rivlin and Ogden models are predicting similar behaviour. While all the material models predict the uni-axial tensile data well, the difference are in the extrapolation to the uni-axial compression region. This will be discussed further in Chapter 10.

6.8   Sensitivity Study of Material Models' Constants

When using optimisation to obtain material models, it is important to note that the answer is an approximation within predefined tolerances of the correct one. This study was thus conducted to study the effect of material model constant deviation. Material constants near the values obtained using the inverse FE model updating method were selected for each material model, and each constant was then changed by 10 %. The effects are presented below in the same material model sequence of previous sections.

6.8.1   Mooney-Rivlin Two Parameter Model

The material model constants selected for the Mooney-Rivlin two parameter model can be seen in Table 6.10. Figure 6.14 shows the effect of deviating each constant. It can be observed that constant C_{10} has a great effect (about 0.3 MPa) on the prediction curve when deviation occurs.
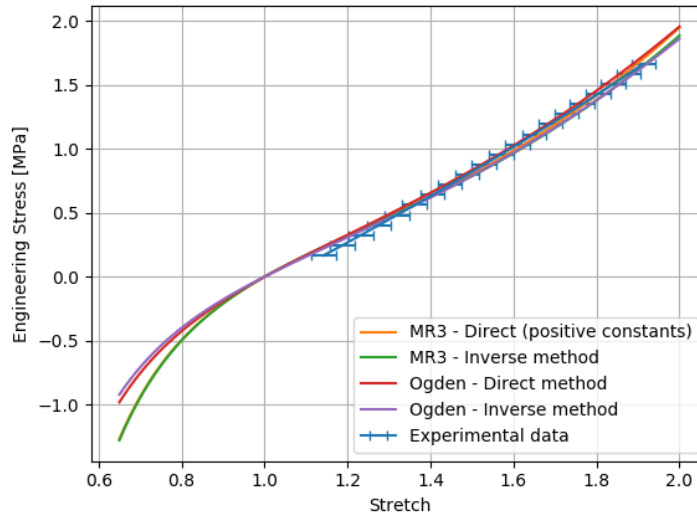
Figure 6.13: Mooney-Rivlin three parameter and Ogden three parameter models obtained from both the direct and inverse FE model updating methods for dumbbell shaped samples on uni-axial tensile tests.

Table 6.10: Material model constants selected for the Mooney-Rivlin two parameter model.

	C_{10} [Pa]	C_{01} [Pa]
Material constants	507603.02	-117564.85

6.8.2   Mooney-Rivlin Three Parameter Model

The material model constants selected for the Mooney-Rivlin three parameter model can be seen in Table 6.11. Figure 6.15 shows the effect of deviating each constant. It can be observed that constant C_{10} has the greatest effect (about 0.3 MPa), followed by the constant C_{20} on the prediction curve when the deviation occurs.

Table 6.11: Material model constants selected for the Mooney-Rivlin three parameter model.

	C_{10} [Pa]	C_{01} [Pa]	C_{20} [Pa]
Material constants	306449.93	2301.17	63038.18
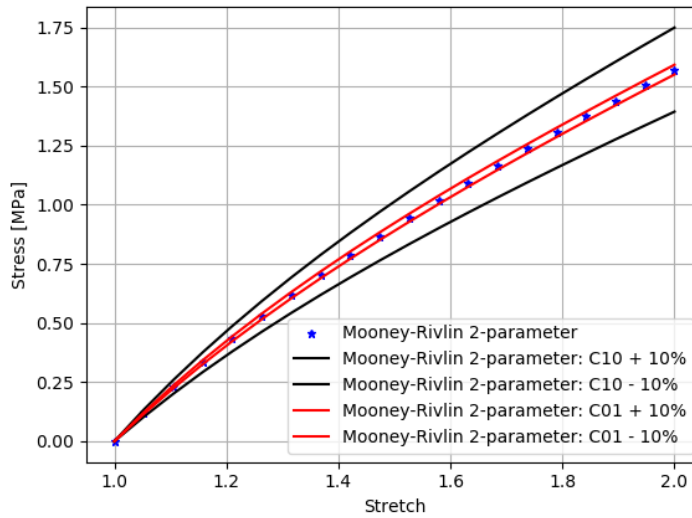
Figure 6.14: Mooney-Rivlin two parameter material model constants' sensitivity study.
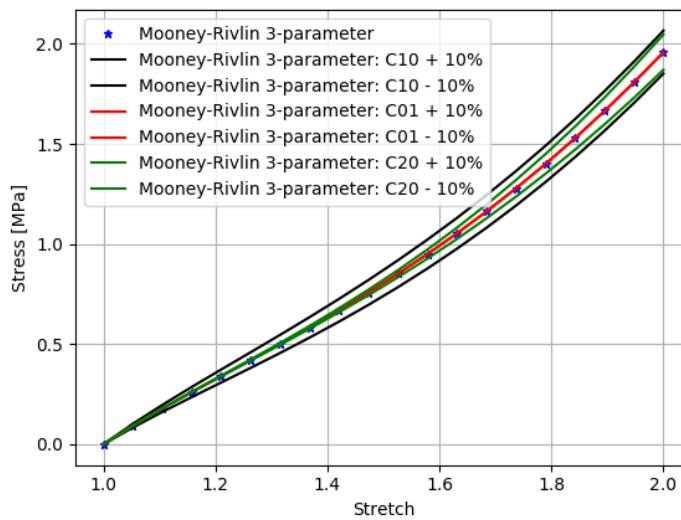
Figure 6.15: Mooney-Rivlin three parameter material model constants' sensitivity study.

6.8.3 Ogden Three Parameter Model

The material model constants selected for the Ogden three parameter model can be seen in Table 6.12. Figure 6.16 shows the effect of deviating each constant. It can be observed that the exponent constants α_i has the greatest effect (about 0.4 MPa), followed by the constants μ_i on the prediction curve when deviation occurs.

Table 6.12: Material model constants selected for the Ogden three parameter model.

	μ_1 [Pa]	α_1	μ_2 [Pa]	α_2	μ_3 [Pa]	α_3
Material constants	100000.01	3.667	100000.01	3.667	100000.01	3.667
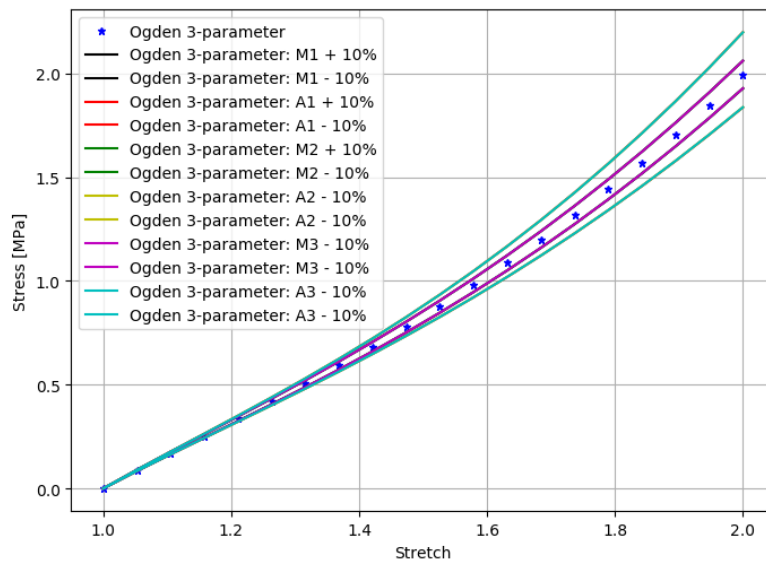
Figure 6.16: Ogden Three parameter material model constants' sensitivity study.

When observing the above figures, it is clear that certain parameters are more sensitive to deviation than others. A reason for the sensitivity of a certain parameter, could be its magnitude relative to the magnitude of other parameters. With an -10 % to +10 % deviation of the parameters the maximum error was ≈ 0.4 MPa (Ogden), which calculated to a ≈ 20 % relative error of stress. It can thus be concluded that the percentage deviation of a certain parameter will result in approximately the same amount of stress prediction error.

Chapter 7

Bi-axial Bubble Inflation Tests

This chapter will discuss the various specifics regarding the bi-axial bubble inflation tests. This will include the test method followed, experimental results and material models obtained.

7.1   Bi-axial Bubble Inflation Test Method

Bi-axial bubble inflation tests were done on a rig that was designed and manufactured in-house. Figure 7.1 shows a side view of the bi-axial bubble inflation test set-up. The rig has a diameter of 50 mm, thus the sample initial diameter (D_0) was also 50 mm. The average sample initial thickness e_0 was measured to be 1.6 mm. Sample membranes were made according to the specifics discussed in Chapter 5. A FESTO pressure transducer was used (Appendix E) to measure the air pressure in the rig, with a rated range of 0 kPa to 200 kPa relative pressure. Testing was conducted at ambient temperature.
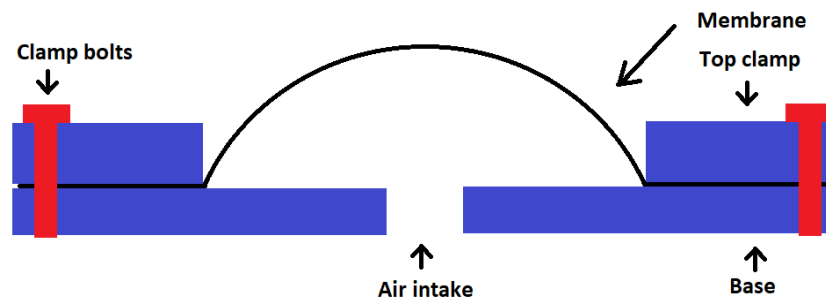
Figure 7.1: Side view of the bi-axial bubble inflation test set-up.

To ensure that the membrane is evenly tightened around the periphery, a torque wrench was used along with a tightening sequence. Eight bolts evenly spaced around the periphery were used. The tightening sequence was torquing

one bolt, skipping two bolts, then torquing the third bolt and continuing this until all bolts were torqued. This was repeated two times to ensure the membrane is evenly torqued all around. The torque value is not as important as having the same value for each bolt. It was found during tests that a larger torque value is better, for it prevented slippage of the material. Figure 7.2 shows a before and after photo of testing a membrane in the bi-axial bubble inflation test rig. Note the blue pen line drawn around the periphery before the test, and how its position stays the same after the test. Thus it can be concluded that no slippage occurred during testing.
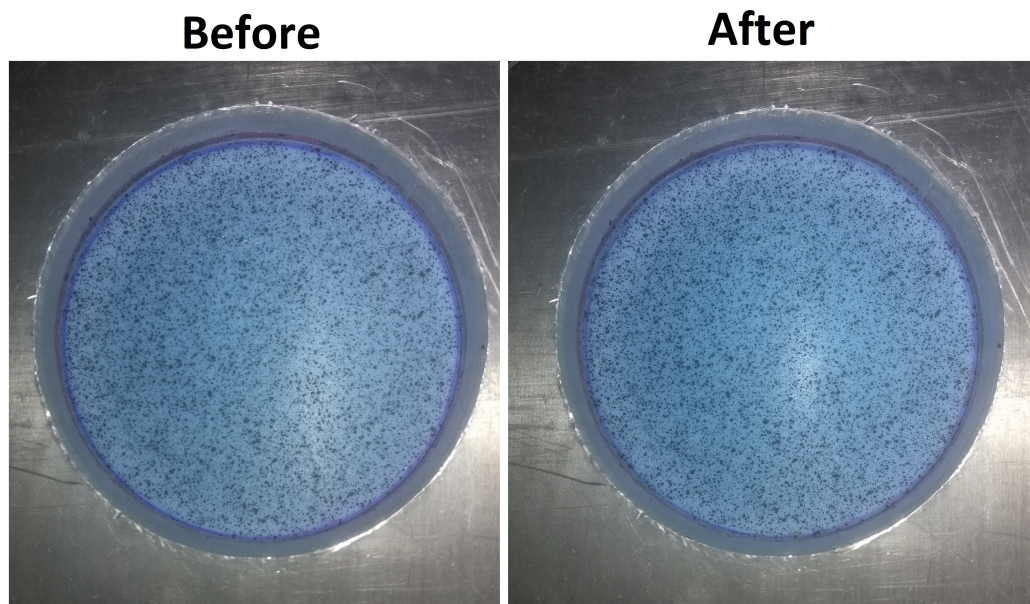
Before   **After**

Figure 7.2: Before and after photo of testing a membrane in the bi-axial bubble inflation test rig. No slippage can be observed.

Figure 7.3 shows the FE mesh that was used for the inverse model updating method. The mesh consisted of 720 Quad 4 thin shell elements. The boundary conditions were:

1. Zero displacement constrains in all three degrees of freedom around the periphery nodes.

2. A frictionless touching contact body boundary condition where the top clamps might come into contact with the membrane.

3. A cavity on all the bottom faces to represent the air pressure.

A mesh refinement study can be found in Appendix H.
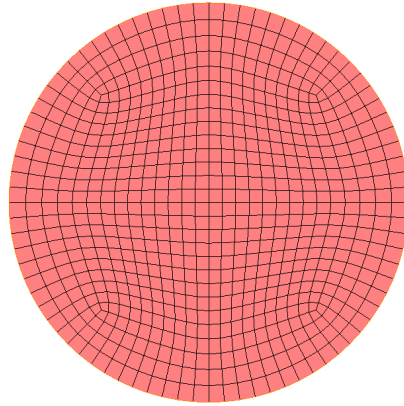
Figure 7.3: FE element mesh of the bi-axial bubble inflation membrane used for the inverse FE model updating method.

7.2 Bi-axial Bubble Inflation Test Experimental Results

Figure 7.4 shows the average engineering stress stretch graph obtained during the bi-axial bubble inflation tests. Six samples were tested. This engineering stress-stretch data were obtained using the X, Y and Z-displacements from the experimental data. The average is shown with relative one standard deviation error bars. Table 7.1 shows the minimum, maximum and average standard deviation of the stretch of the tests. The stretch correlation factor between all tests was calculated to be 0.9799.

Table 7.1: Standard deviations of stretch for bi-axial bubble inflation tests.

	Value
Minimum STD	0.0061
Maximum STD	0.0816
Average STD	0.0428

For the inverse FE model updating method, only the Z-displacements were matched between the FE analysis and the experimental results. To validate this. Figure 7.5 and Figure 7.6 show the material models obtained from the inverse method along with the experimental engineering stress-stretch curve. It can be observed that the material models match the experimental data. Thus using only the Z-displacements during the inverse method is sufficient when it matched the experimental data which was obtained using X, Y and Z-displacements.
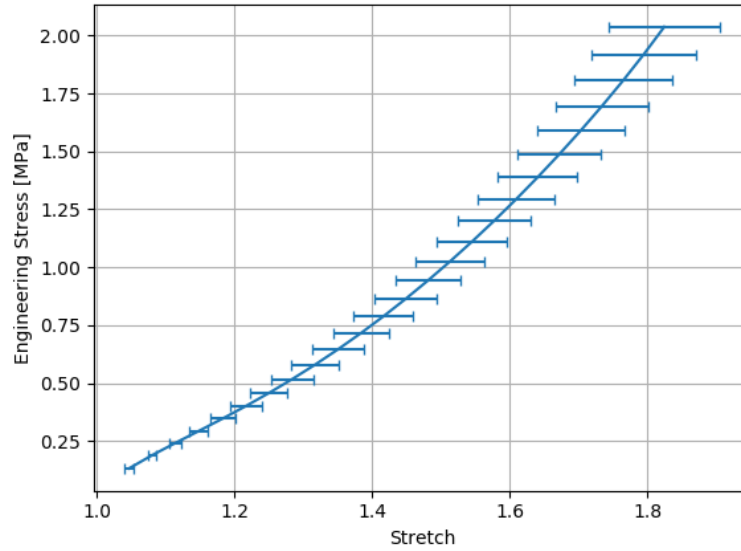
Figure 7.4: Engineering stress stretch graph obtained during the six bi-axial bubble inflation tests. The average of the tests are also shown with relative one standard deviation error bars.

7.3   Mooney-Rivlin Three Parameter Model

The bi-axial bubble inflation test can be seen as an equi-bi-axial tensile load state. To conserve the assumption of incompressibility, the stretch deformations become:

$$\lambda_1 = \lambda_2 = \lambda$$
$$\lambda_3 = \frac{1}{\lambda^2} \tag{7.1}$$

Using this, the following engineering stress-stretch equation for a equi-bi-axial tensile load state can be determined:

$$
\begin{aligned}
\sigma_e(\lambda) =& 2C_{10}\left(\lambda - \frac{1}{\lambda^5}\right) + 2C_{01}\left(\lambda^3 - \frac{1}{\lambda^3}\right) \\
& + 4C_{20}\left(\lambda - \frac{1}{\lambda^5}\right)\left(2\lambda^2 + \frac{1}{\lambda^4} - 3\right)
\end{aligned} \tag{7.2}
$$

Table 7.2 shows the material constants that govern the Mooney-Rivlin three parameter material model obtained using the direct method and the inverse FE model updating method. The two material models obtained with the average experimental data can be seen in Figure 7.5. No constraints were necessary during the direct method to obtain a feasible material model. The extrapolation of the material models that were obtained can be found in Chapter 10. It

can be observed that both have a good fit to the experimental data.

Table 7.2: Mooney-Rivlin three parameter model constants obtained using the direct and inverse methods on bi-axial bubble inflation experimental data.

	C_{10} [Pa]	C_{01} [Pa]	C_{20} [Pa]
Direct method	391166.63	-152451.75	92171.05
Inverse method	392077.85	-153817.83	93338.85
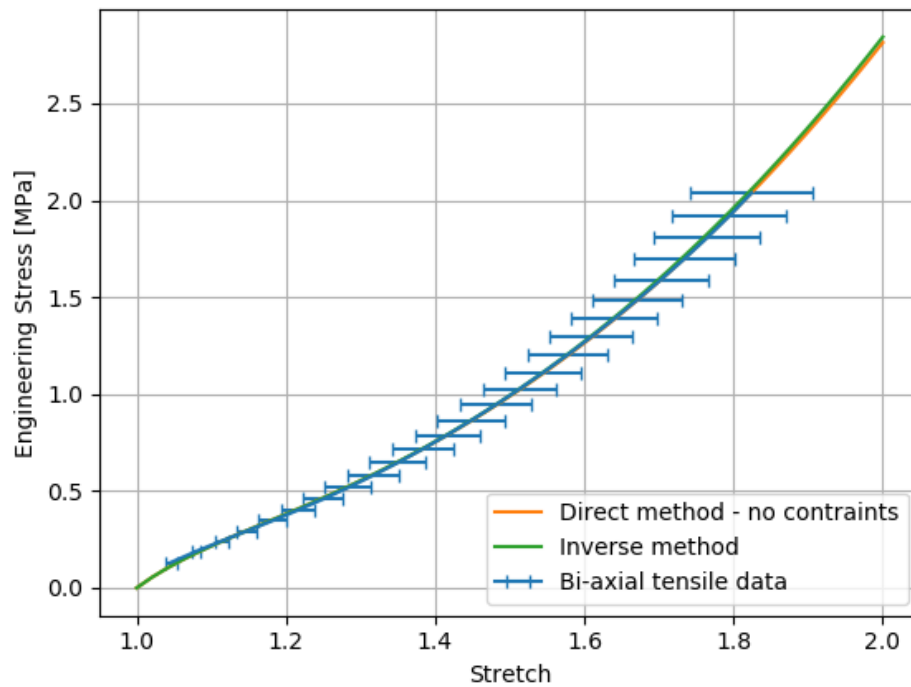
Figure 7.5: Mooney-Rivlin three parameter models obtained using the direct and inverse methods on bi-axial bubble inflation experimental data.

7.4   Ogden Three Parameter Model

The equation that governs the Ogden three parameter model for a equi-bi-axial tensile load state, can be determined by using Equation 7.1 in Equation 2.15. The obtained equation is then partially derived with respect to stretch (Equation 6.7) to obtain the following:

$$\sigma(\lambda) = \sum_{i=1}^{N} \mu_i \left(\lambda^{\alpha_i - 1} - \lambda^{-(2\alpha_i + 1)} \right), \quad N = 3 \tag{7.3}$$

The material model's parameters obtained using the direct method and inverse FE model updating method can be seen in Table 7.3. Figure 7.6 shows the two material models obtained from the two methods. It can be observed that the material models have a good fit to the experimental data.

Table 7.3: Ogden three parameter model constants obtained using the direct and inverse methods on bi-axial bubble inflation experimental data.

	$\mu 1$	$\alpha 1$	$\mu 2$	$\alpha 2$	$\mu 3$	α
Direct method	121691.65	4.384	-139085.16	2.328	186040.15	4.384
Inverse method	120664.49	4.200	-137268.42	2.536	185289.84	4.490
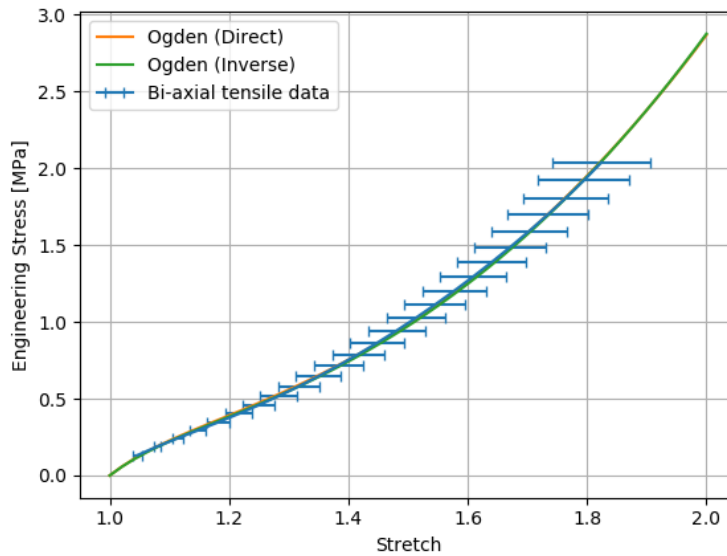
Figure 7.6: Stress-Stretch graph of Ogden three parameter models obtained using the direct and inverse methods on bi-axial bubble inflation experimental data.

Chapter 8

Unconstrained Uni-axial Compression Tests

In this chapter, the unconstrained uni-axial compression tests will be discussed. The chapter will start with the test parameters that were followed, and then the respective results that were obtained.

8.1 Unconstrained Uni-axial Compression Test Method

Using the MTS Criterion 44 universal testing machine, unconstrained uni-axial compression tests were done. In-house manufactured flat cylindrical platforms were used instead of the normal MTS grips. The crossarm was set to move these platforms towards each other, which caused the compression of the samples. A MTS 30 kN load cell was used to measure the compression force. Samples were cylindrical with an initial diameter (D_0) of 32 mm and initial height (h_0) 26 mm. The compression platforms were coated with a silicone lubricant to limit the friction between them and the samples. The DIC system described in Chapter 2 was used to measure the deformation.

For the inverse FE model updating method, an FE model was required. Figure 8.1 shows the FE model that was used for the unconstrained uni-axial compression samples. A quarter model was used with 1 474 tetrahedral elements. The FE model was only a portion of the centre of the sample to avoid the complex boundary conditions near the compression platforms. The boundary conditions were:

1. A prescribed non-zero displacement in the Y-direction for the top nodes.

2. A prescribed non-zero displacement in the Y-direction for the bottom nodes.

3. Symmetric constraints in the X- and Z-direction faces

With these boundary conditions, the reaction force obtained from the experimental results were compared to the one obtained from the FE analysis in the inverse FE model updating method. A mesh refinement study can be found in Appendix I.
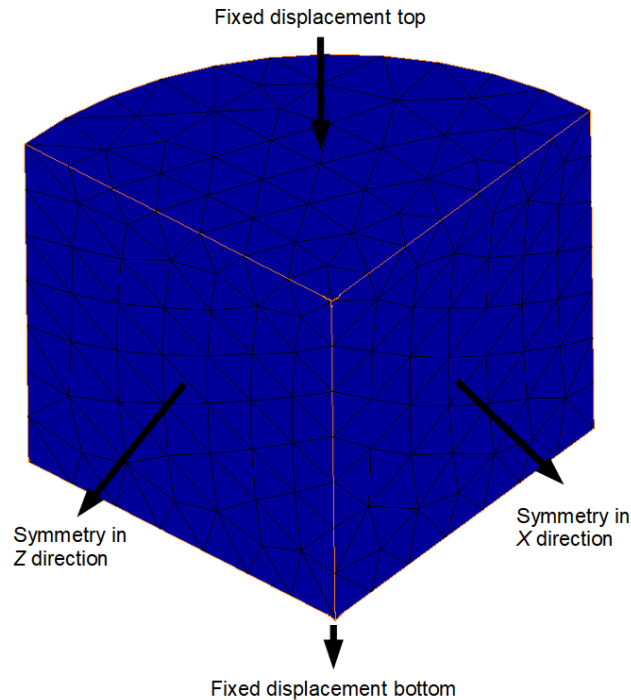
Figure 8.1: FE model used for the unconstrained uni-axial compression samples for inverse FE model updating method. The boundary conditions are also shown.

8.2   Unconstrained Uni-axial Compression Test Experimental Results

Figure 8.2 shows the average engineering stress stretch graph obtained during the four uni-axial compression tests. The average is also shown with relative one standard deviation error bars. Table 8.1 shows the minimum, maximum and average standard deviation of the stretch of the tests. The correlation factor between all tests was calculated to be 0.9832.

Table 8.1: Standard deviations of stretch for unconstrained uni-axial compression tests.

	Value
Minimum STD	0.0031
Maximum STD	0.0185
Average STD	0.0086
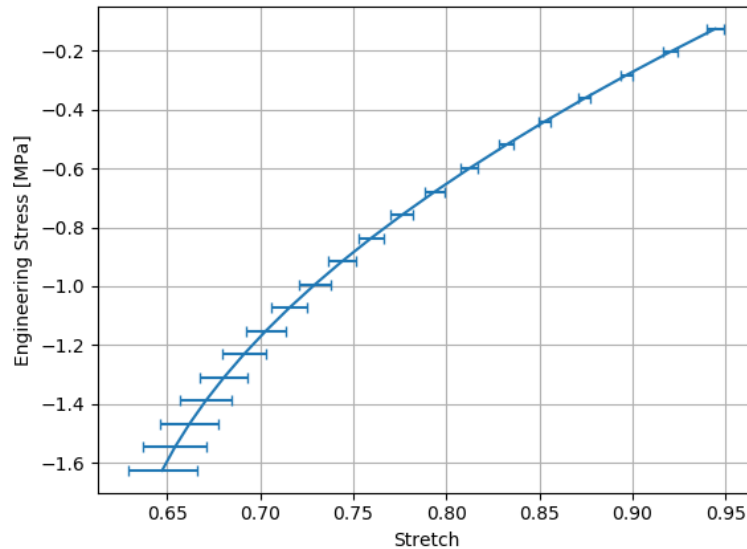
Figure 8.2: Engineering stress stretch graph obtained during the four uni-axial compression tests. The average of the tests are also shown with relative one standard deviation error bars.

8.3   Mooney-Rivlin Three Parameter Model

To determine the Mooney-Rivlin three parameter model, the same equation is used as in the uni-axial tensile tests (Equation 6.5). Table 8.2 shows the material constants that govern the Mooney-Rivlin three parameter material model obtained using the direct method and the inverse FE model updating method. The two material models obtained with the average experimental data can be seen in Figure 8.3. It can be observed that the material models have a good fit to the experimental data.

8.4   Ogden Three Parameter Model

As in the previous section, the same equation is used as in the uni-axial tensile tests to determine the Ogden three parameter model (Equation 6.8). The

Table 8.2: Mooney-Rivlin three parameter model constants obtained using the direct and inverse methods on compression experimental data.

|	C_{10} [Pa]	C_{01} [Pa]	C_{20} [Pa]
Direct method	618294.59	-187384.12	130124.58
Inverse method	620054.38	-184715.04	131775.38

Figure 8.3: Stress-Stretch graph of Mooney-Rivlin three parameter models obtained using the direct and inverse methods on compression experimental data.

material model's parameters obtained using the direct method and inverse FE model updating method can be seen in Table 8.3. Note the big difference between the μ_1 and α_1 constants from both material models.

Table 8.3: Results obtained using the direct method for the Ogden three parameter model.

	μ_1 [Pa]	α_1	μ_2 [Pa]	α_2	μ_3 [Pa]	α_3
Direct method	0.05	64.73	1736868.52	0.463	1691030.15	0.463
Inverse method	130151.00	4.811	130151.00	4.811	130151.00	4.811

It can also be observed in Figure 8.4 that the material model from using the direct method has a better fit to the compression data than the one obtained from the inverse FE model updating method. However, when extrapolating the

models into the uni-axial tensile region (Figure 8.5) it is can be observed that the material model obtained from the direct method predicts at first an under prediction of stress (below 1.28 stretch), followed by an over prediction of stress with a large gradient (above 1.28 stretch). This material behaviour can be considered illogical. It can be concluded that while the direct method provides a material model with a better fit to the compression data, the material model obtained from the inverse FE model updating method provides a more robust material model when extrapolated.
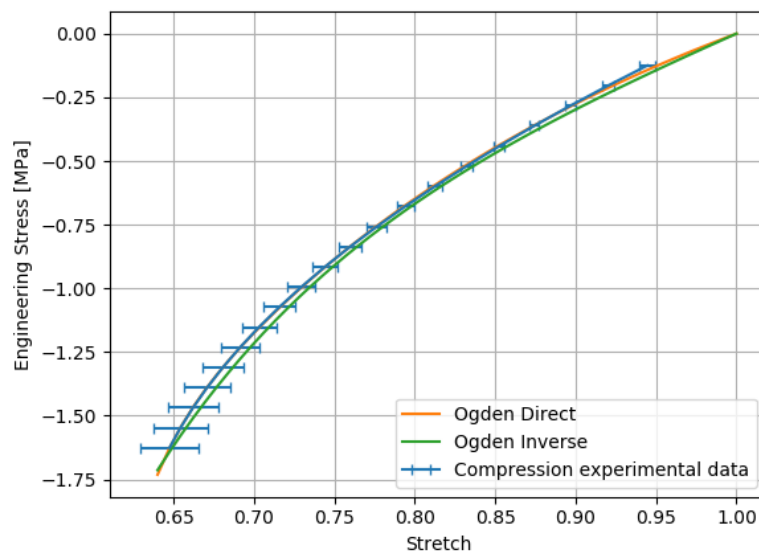
Figure 8.4: Stress-Stretch graph of Ogden three parameter models obtained using the direct and inverse methods on compression experimental data.
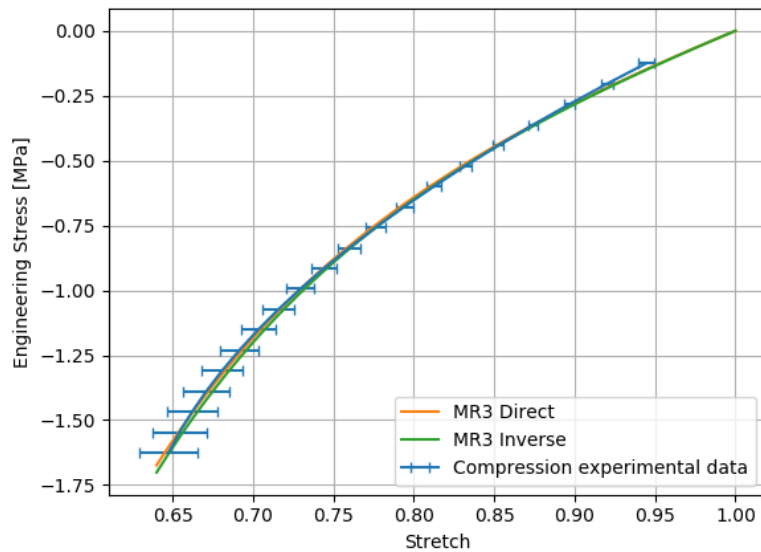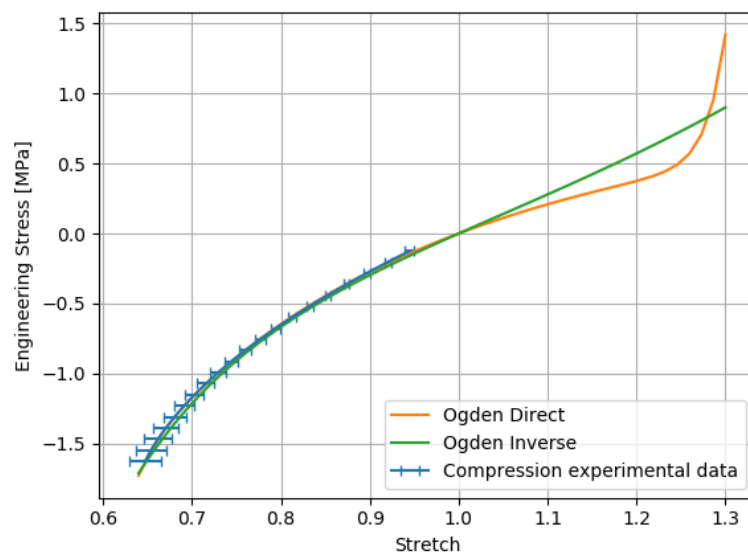
Figure 8.5: Stress-Stretch graph of Ogden three parameter models obtained using the direct and inverse methods on compression experimental data. The material models are also extrapolated into the uni-axial tensile region.

Chapter 9

Combination of Uni-axial Tensile and Compression Data

In this chapter, the uni-axial tensile and unconstrained uni-axial compression test data were combined. Thereafter, Mooney-Rivlin and Ogden three parameter models were obtained using the direct and inverse FE model updating methods.

9.1   Material Models Obtained

For the direct method, uni-axial tensile data from both the rectangular flat strip samples and the dumbbell shaped samples were combined for the average uni-axial tensile engineering stress-stretch data. The obtained data was then combined with the unconstrained uni-axial compression test data. Using the direct method, as described in Chapter 6, the following Mooney-Rivlin (Table 9.1) and Ogden three parameter (Table 9.2) models were obtained.

For the inverse FE model updating method, the FE model for the dumbbell shaped samples (uni-axial tensile) and the FE model for the compression cylinders were set to run in series within the numerical optimisation work flow. Both RMS error values are then normalised and combined to produce a single RMS error value. The rest of the method was done as described in Chapter 6. The Mooney-Rivlin and Ogden three parameter models obtained can be found in Table 9.1 and Table 9.2 respectively.

Figure 9.1a and Figure 9.1b shows the uni-axial tensile and compression experimental data, along with the Mooney-Rivlin- and Ogden three parameter models obtained respectively. It can be observed that all material models show a good fit to the experimental data. An evaluation of the material models can be found in Chapter 10.

Table 9.1: Mooney-Rivlin three parameter model constants obtained using
the direct and inverse FE model updating method on uni-axial tensile and
compression experimental data.

	C_{10} [Pa]	C_{01} [Pa]	C_{20} [Pa]
Direct method	269643.83	90990.36	57058.50
Inverse method	260567.62	97549.81	57500.69

Table 9.2: Ogden three parameter model constants obtained using the direct
method and inverse FE model updating method on uni-axial tensile and com-
pression experimental data.

	μ_1 [Pa]	α_1	μ_2 [Pa]	α_2	μ_3 [Pa]	α_3
Direct method	-918366902	1.502	404974716	1.618	519845057	1.397
Inverse method	-918374777	1.502	404966035	1.617	519837879	1.396
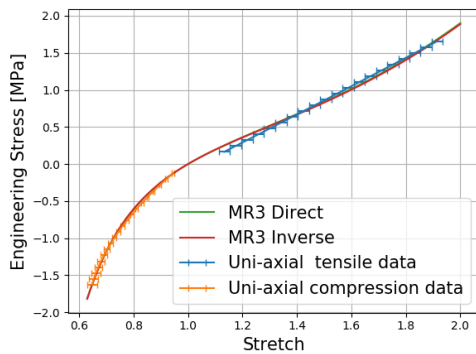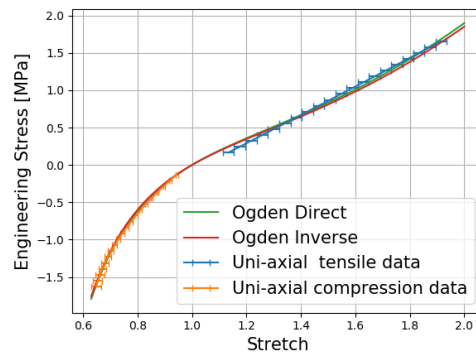
(a) Mooney-Rivlin three parameter.   (b) Ogden three parameter.

Figure 9.1: Stress-Stretch graph of uni-axial tensile and compression test data
along with material models obtained.

Chapter 10

Validation Test and Model Extrapolation

This chapter will discuss specifics regarding the independent validation test. The purpose of this test was to compare the different models obtained, independently with one another. To choose the best model, the validation test results along with the extrapolation of the model into different stress states will be considered.

10.1   Validation Test Method

The validation test was a uni-axial tensile test, with a complex sample geometry, as can be seen in Figure 10.1a. The MTS Criterion 44 universal testing machine with a 1 kN load cell was used with standard MTS grips. The DIC system as described in Chapter 2, was used to measure the deformation. Two samples were tested. Figure 10.1b shows the mesh used for the FE analysis, along with the following boundary conditions:

1. Prescribed Y-displacement on the top nodes.

2. Prescribed Y-displacement on the bottom nodes.

3. Prescribed X-displacement on the top and bottom most left nodes.

4. Prescribed X-displacement on the top and bottom most right nodes.

An FE mesh refinement study can be seen in Appendix J.

To emphasize the complexity of the validation sample, Figure 10.2 shows the FE model with the equivalent Von Mises stress state.

(a) Validation test sample geometry.

(b) Validation test FE mesh with boundary conditions.
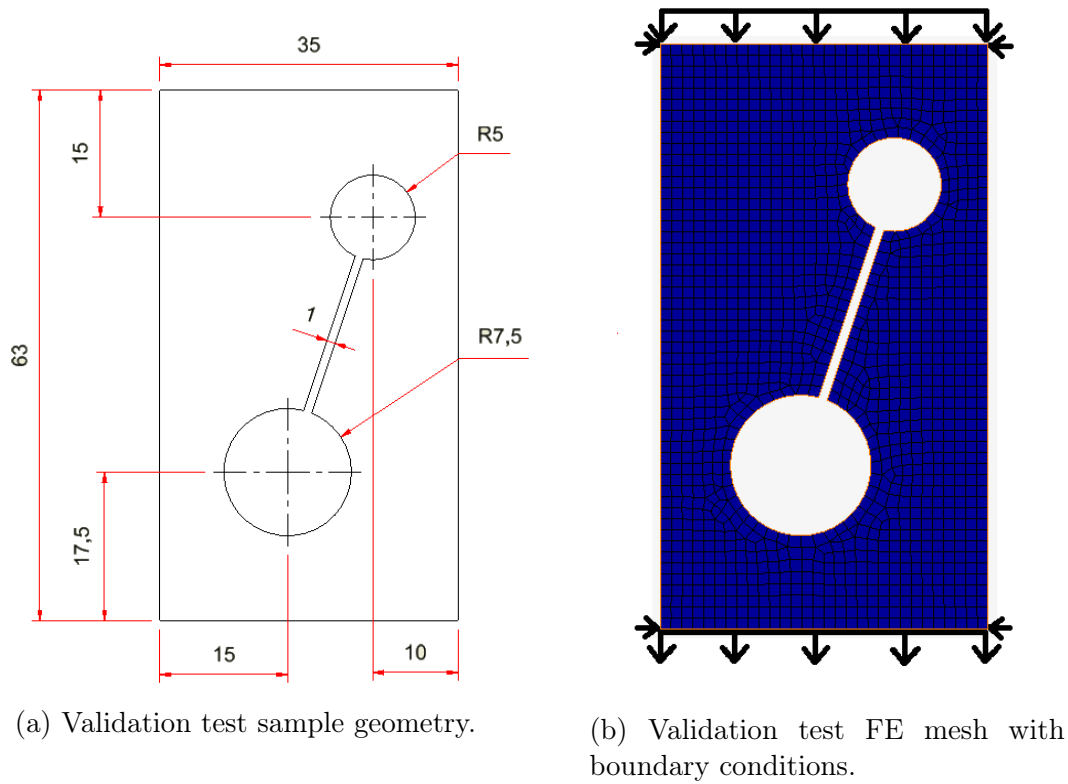
Figure 10.1: Uni-axial tensile validation test sample.

The top and bottom node displacements were predicted using a polynomial fit, with their X-coordinates as the input and the Y-displacements as the output. For the top nodes, a fourth order fit was used with an R-squared valued of 0.996 and R-squared adjusted value of 0.996. For the bottom nodes, a fifth order fit was used with an R-squared valued of 0.996 and R-squared adjusted value of 0.996. Figure 10.3 shows the top and bottom nodes before the test and at the moment where the displacements are predicted. The polynomial predicted vs. actual displacements for the top and bottom nodes are also shown.
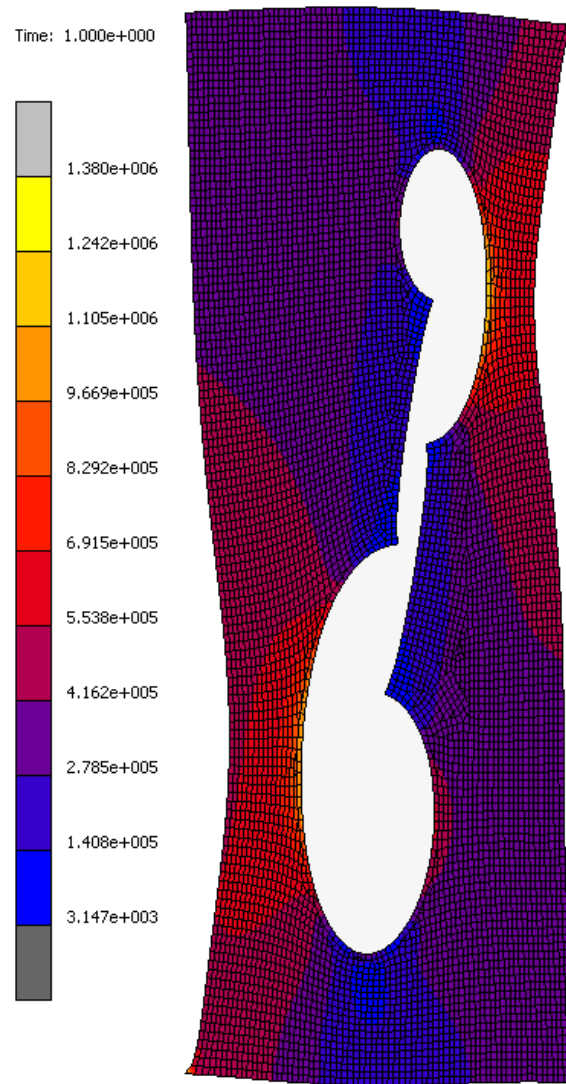
Figure 10.2: FE model of validation test sample with a complex equivalent Von Mises stress state.
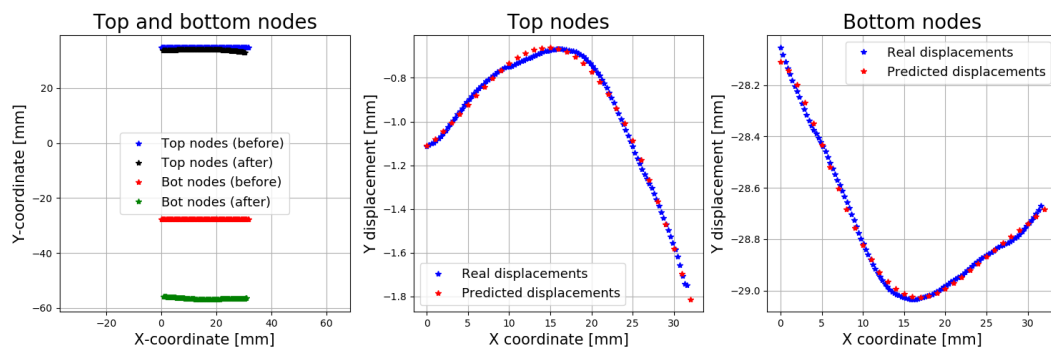
Figure 10.3: Top and bottom nodes before the test and at the moment where the displacements are predicted.

10.2   Evaluation of Models Obtained with Validation Test

For the validation tests, the top and bottom displacements are prescribed within the FE model as the boundary conditions. Figure 10.4 shows the experimental outline of a validation sample, and how it overlaps the FE model. It can be seen that it has a good fit. To calculate how good a certain material model is, the calculated reaction force is compared to the reaction force obtained from the experimental data. Table 10.1 shows the results from various Mooney-Rivlin three parameter models. Only material models obtained that predicted logical material behaviour are shown. The direct method material models for Mooney-Rivlin are the ones obtained using the positive constant constraints. The relative error was calculated with the following equation:

$$error_\% = \frac{F_{FEM} - F_{Exp}}{F_{Exp}} \times 100 \qquad (10.1)$$

where F_{FEM} is the reaction force obtained from the FE model and F_{Exp} is the actual reaction force from the experiments. A positive answer in Equation 10.1 will indicate that the model over predicts the reaction force, while a negative answer correlates to an under prediction. It can be observed that the Mooney-Rivlin three parameter models obtained from the uni-axial compression tests have a large reaction force prediction error. A reason for this could be that these models were obtained from different stress state than the validation test, and thus are bad in prediction different stress states other than their own. The material models obtained from the bi-axial bubble inflation tests, the uni-axial tensile tests and the combination of uni-axial tension and compression data have the smallest errors (accuracy within 5 %). However, the validation test only evaluates the material model's prediction of a specified reaction force, which in this thesis correlates to ≈ 0.9 MPa.

Table 10.2 shows various Ogden three parameter models obtained from the various tests and methods. Only material models that predicted valid material behaviour are shown. The relative error was calculated as in Equation 10.1. For the Ogden models, both bubble inflation methods and the inverse uni-axial compression method had large errors (≥ 10 %). While the uni-axial tensile methods had the smallest errors, with the inverse method on dumbbell shaped samples the winner. The material models obtained using the direct and inverse method on uni-axial tensile and compression data also gave reasonable assumptions.
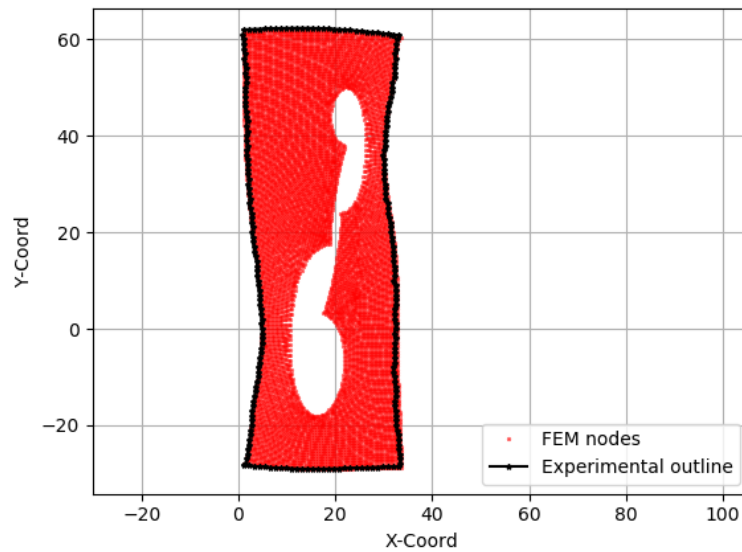
Figure 10.4: Experimental outline of validation sample overlapping the FE model.

Table 10.1: Results for various Mooney-Rivlin three parameter models when compared to the validation test results.

Material Model	Relative error [%]
Inverse flat strip	0.44
Inverse bubble	-0.89
Direct bubble	-1.16
Direct dumbbell	-1.91
Inverse uni+comp	2.37
Inverse dumbbell	-3.36
Direct uni+comp	3.97
Direct flat strip	4.23
Direct compression	63.11
Inverse compression	69.91

Table 10.2: Results for various Ogden three parameter models when compared to the validation test results.

Material Model	Relative error [%]
Inverse dumbbell	-0.04
Inverse flat strip	4.93
Direct dumbbell	5.85
Direct flat strip	7.12
Inverse uni+comp	7.87
Direct uni+comp	8.05
Inverse bubble	15.33
Direct bubble	16.79
Inverse compression	114.01

10.3   Evaluation of Model Extrapolation

The previous section was used as the deciding factor to filter the material models used in this section. For a material model to be used in this section, it must have predicted the validation test reaction force within a 10 % error. However, when comparing the material models obtained from each experimental test, it can be observed that both identification methods deliver similar results for that specific test. For that reason only one material model from each experimental test was chosen to be extrapolated. The observations made for the extrapolated material model can be assumed to be the same for the other identification method in the specific experimental test. Thus the following Mooney-Rivlin three parameter models were investigated further:

1. Inverse method on uni-axial tensile tests (rectangular flat strip samples).

2. Inverse method on bi-axial bubble inflation tests.

3. Direct method on uni-axial tensile tests (dumbbell shaped samples).

4. Inverse method on uni-axial tensile and compression data.

The following Ogden three parameter models were also investigated further, in order of samples:

1. Inverse method on uni-axial tensile tests (dumbbell shaped samples).

2. Inverse method on uni-axial tensile tests (rectangular flat strip samples).

3. Inverse method on uni-axial tensile and compression data.

Each material model will be extrapolated to predict uni-axial tension, uni-axial compression and bi-axial tension stress states. To validate the accuracy of prediction, experimental data obtained throughout this thesis will be used.

The following two subsections will discuss the Mooney-Rivlin three parameter models and Ogden three parameter material models respectively.

10.3.1 Extrapolation of Mooney-Rivlin Three Parameter Models

Figure 10.5 shows the extrapolation of the Mooney-Rivlin three parameter model obtained on uni-axial tensile data for the rectangular flat strip samples using the inverse method. The material models have been interpolated for uni-axial tension data (Equation 6.5) and extrapolated for both uni-axial compression (Equation 6.5) and bi-axial tension data (Equation 7.2). It can be observed that the material model has a good prediction of uni-axial tensile engineering stress (expected), with an under prediction of engineering stress for uni-axial compression (maximum $\approx 20\%$ relative error) and an over prediction for bi-axial engineering stress (maximum $\approx 50\%$ relative error).

Figure 10.5: Extrapolation of Mooney-Rivlin three parameter model obtained using the inverse method on uni-axial tensile test data (Rectangular flat strip samples).

Figure 10.6 shows the extrapolation of the Mooney-Rivlin three parameter model obtained from using the inverse method on bi-axial bubble inflation data. A good fit on the bi-axial tensile engineering stress can be seen (expected), but uni-axial compression engineering stress is under predicted (maximum $\approx 47\%$ relative error). For the uni-axial tensile engineering stress, a good prediction can be observed below a stretch of 1.6, there-after the material

model over predicts the engineering stress (maximum ≈ 20 % relative error).

Figure 10.6: Extrapolation of Mooney-Rivlin three parameter model obtained using the inverse method on bi-axial bubble inflation test data.

Figure 10.7 shows the extrapolation of the Mooney-Rivlin three parameter model obtained on uni-axial tensile data for the dumbbell shaped samples using the direct method. It can be observed that the material model has a good prediction of uni-axial tensile engineering stress (expected), with an under prediction of engineering stress for uni-axial compression (maximum ≈ 20 % relative error) and an over prediction for bi-axial engineering stress (maximum ≈ 50 % relative error).
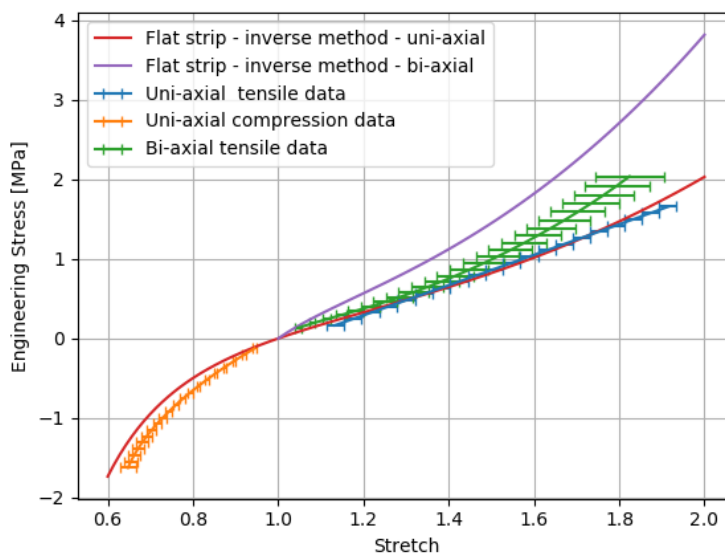
Figure 10.8 shows the extrapolation of the Mooney-Rivlin three parameter models obtained from the combination of uni-axial tensile and compression data. A good fit can be seen for both these stress states (expected), but the bi-axial bubble inflation tensile engineering stress are being over predicted (maximum ≈ 90 % relative error)

When observing the above figures, it can be seen that the validation test alone was alone not sufficient enough to validate the material models. When comparing the validation test results and the extrapolation of the material models, the material models obtained from the uni-axial tensile tests were chosen as the best. However, for the direct method, extra user-input constraints were necessary to find a material model that predicted feasible material be-

Figure 10.7: Extrapolation of Mooney-Rivlin three parameter model obtained using the direct method on uni-axial tensile test data (Dumbbell shaped samples).
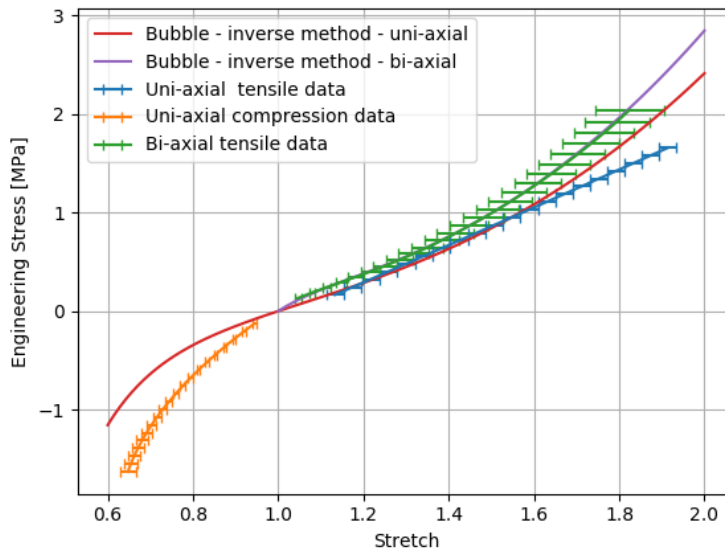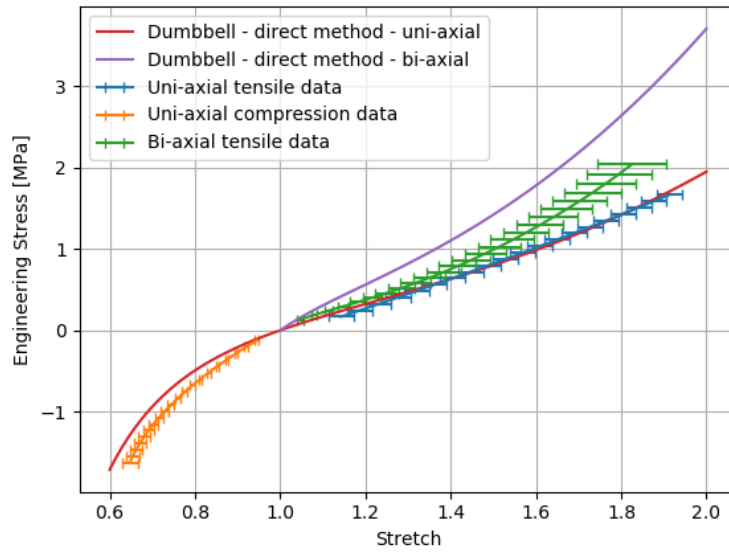

Figure 10.8: Extrapolation of Mooney-Rivlin three parameter model obtained using the inverse method on a combination of uni-axial tensile and compression test data.

haviour. It is also necessary to note that the Mooney-Rivlin three parameter model is only an approximation, and thus, in this case, cannot predict all the stress states.

10.3.2   Extrapolation of Ogden Three Parameter Models

Figure 10.9 shows the extrapolation of the Ogden three parameter model obtained from the uni-axial tensile data (dumbbell shaped samples). It can be observed that the material model has a good prediction of uni-axial tension (Equation 6.8) engineering stress (expected), with an under prediction of engineering stress for uni-axial compression (Equation 6.8) (maximum $\approx$ 42 % relative error). The bi-axial tension (Equation 7.3) engineering stress are firstly over predicted (below 1.3 stretch) followed by an under prediction (above 1.3 stretch) with a maximum relative error approximately 38 %.

Figure 10.9: Extrapolation of the Ogden three parameter model obtained using the inverse method on uni-axial tensile data (Dumbbell shaped samples)

Figure 10.10 shows the extrapolation of the Ogden three parameter model obtained from the uni-axial tensile data (Rectangular flat strip samples). It can be observed that the material model has the same prediction characteristics as stated above for the dumbbell shaped samples.

Figure 10.11 shows the extrapolation of the Ogden three parameter models obtained from the combination of uni-axial tensile and compression data. A

Figure 10.10: Extrapolation of the Ogden three parameter model obtained using the inverse method on uni-axial tensile data (Rectangular flat strip samples)

good fit can be seen for both these stress states (expected) but the bi-axial bubble inflation tensile engineering stress are being over predicted with a maximum relative error approximately 90 %.

In the above figures, it can be observed that the Ogden three parameter mode fails to predict all the stress states. A reason for this is that the Ogden three parameter model is only an approximation.

10.4   Best Material Model Obtained

When the Ogden three parameter models are compared to the Moonley-Rivlin three parameter models, a possible trend can be observed where the Mooney-Rivlin models tend to have a better prediction of the stress states when extrapolated than the Ogden models. Another advantage of the Mooney-Rivlin model (three unknowns) is that it is simpler that the Ogden model (six unknowns). For this reasons, the Mooney-Rivlin three parameter was chosen as the best material model in this thesis.

An advantage of using the inverse FE model updating method, is that it guarantees a successful FE analysis without using constraints, as long as the initial parameters are valid. Initial parameters were found in literature as
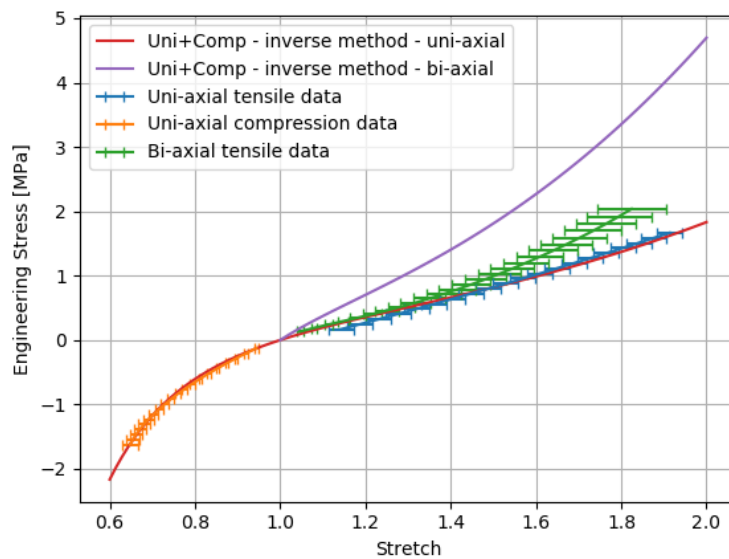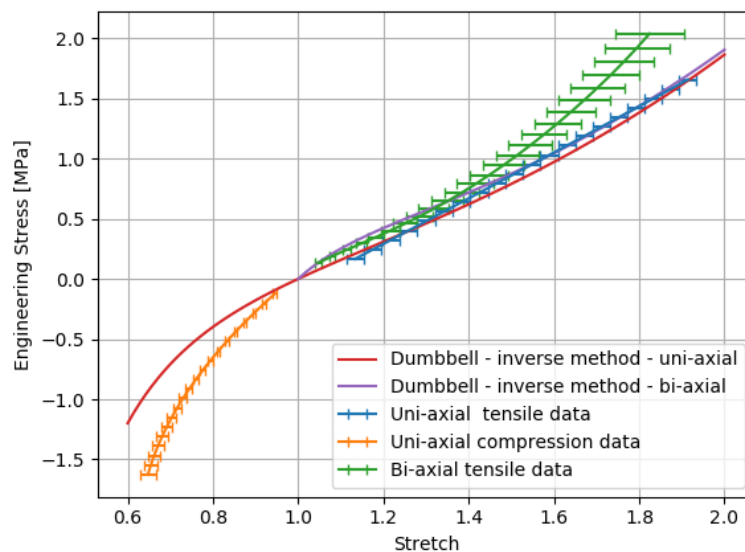
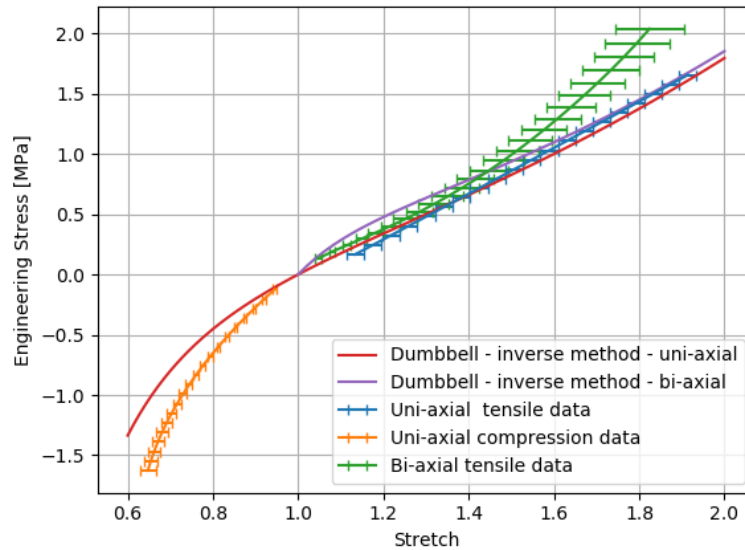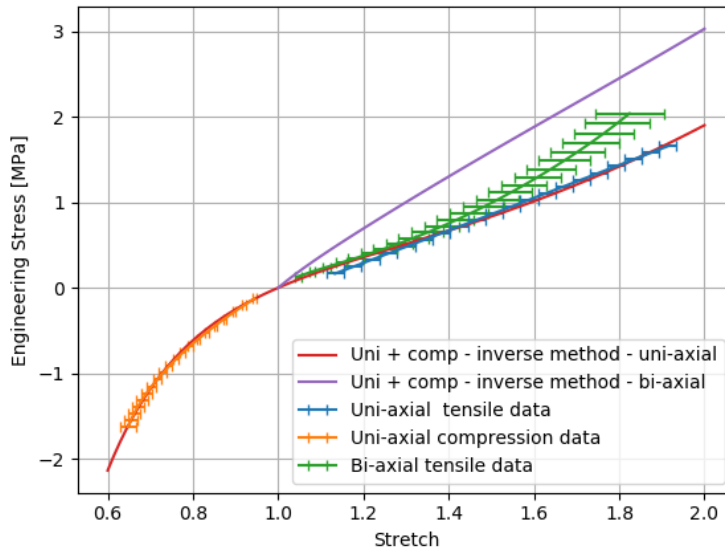Figure 10.11: Extrapolation of the Ogden three parameter model obtained using a combination of uni-axial tensile and compression test data using the inverse method.

stated before (Sasso *et al.* (2008) and Rachik *et al.* (2001)). Using the inverse method will ensure that the material model will predict feasible material behaviour when extrapolated.

When taking the validation test results and the extrapolation into account, the best material model would be the Mooney-Rivlin three parameter model obtained from using both identification methods on uni-axial tensile tests (both samples).

Chapter 11

Conclusion

Uni-axial tension, compression and bi-axial bubble inflation tests were performed on silicone-rubber. As an introduction, Mooney-Rivlin two parameter models were determined from uni-axial tensile test data using the direct and inverse FE model updating method. It was found that the Mooney-Rivlin two parameter model fails to accurately predict the stress state. The more complex Mooney-Rivlin three parameter and Ogden three parameter hyperelastic constitutive material models were then determined from each test using the direct and inverse FE model updating methods. A special Mooney-Rivlin three parameter and Ogden three parameter model were determined by combining uni-axial tensile and compression data and using the direct and inverse FE model updating methods. An independent validation test was done along with an evaluation on material model extrapolation. Taking both into account, it was found that the Mooney-Rivlin three parameter model obtained from uni-axial tensile tests using both identification methods gave the best prediction.

11.1   Experimental Tests

Specifics regarding the uni-axial tensile test will first be discussed, followed by the bi-axial bubble inflation and uni-axial compression tests.

11.1.1   Uni-axial Tensile

Four samples of each geometry (rectangular flat strip and dumbbell shaped) samples were tested, with a correlation factor of 0.9989 and 0.994 for stretch, respectively. A moulding process study was conducted and concluded that using a vacuum and an elevated cure temperature will result in possible different material behaviour. Thus the moulding process for this thesis was consistent throughout all samples (no vacuum and curing at ambient temperature), except for the cylindrical samples used for the uni-axial compression tests (vac-

uumed and cured at ambient temperature). A strain-rate sensitivity study was also conducted and concluded that silicone-rubber is not very strain rate dependent, but there is a small effect for high strain rates (9^{-1} s^{-1}). Thus for consistency, all tests were done on a medium strain rate of 45^{-1} s^{-1} or less. It was also shown that using only Y-displacements is enough compared to using X and Y-displacements for determining material models using displacement field measurements.

As an introduction to both the direct and inverse FE model updating methods, the Mooney-Rivlin two parameter model was determined for both sample geometries. After this four material models were determined for each sample geometry:

1. Mooney-Rivlin three parameter model using the direct method.

2. Mooney-Rivlin three parameter model using the inverse FE model updating method.

3. Ogden three parameter model using the direct method.

4. Ogden three parameter model using the inverse FE model updating method.

The Mooney-Rivlin three parameter models obtained using the direct method initially failed to predict feasible material behaviour. The problem was solved by introducing positive constant constraints. To ensure that the material model always predict feasible material behaviour, the inverse FE model updating method should be used with valid initial parameters that can be found in literature.

11.1.2   Bi-axial Bubble Inflation and Uni-axial Compression

Six samples were tested using the bi-axial bubble inflation test, with a correlation factor of 0.9799 for stretch. A no-slippage assumption was confirmed by the described method, which simplifies the material model determination. It was shown that the bubble deforms symmetrical and hemispherical. It was also shown that only the Z-displacements are sufficient when determining material models from the inverse FE model updating method.

Four samples were tested using the uni-axial compression test, with a correlation factor of 0.9832 for stretch. For both tests, four material models each were determined:

1. Mooney-Rivlin three parameter model using the direct method.

2. Mooney-Rivlin three parameter model using the inverse FE model up-dating method.

3. Ogden three parameter model using the direct method.

4. Ogden three parameter model using the inverse FE model updating method.

The Ogden three parameter model obtained using the direct method on compression data failed to predict feasible material behaviour. While the Mooney-Rivlin three parameter model obtained using the inverse FE model updating method on bi-axial bubble inflation data performed the best.

11.2   Combination of Uni-axial Tensile and Compression Data

The uni-axial tension and compression test data were combined. Thereafter, Mooney-Rivlin and Ogden three parameter models were determined using the direct and inverse FE model updating methods. All the material models had a good prediction of uni-axial tension and compression engineering stress, however it over predicted the bi-axial engineering stress.

11.3   Independent Validation Test and Evaluation of Model Extrapolation

An independent validation test with a complex stress state was done to compare all the material models obtained. Two samples were tested. Using full field DIC displacements, an FE model was created with non-linear top and bottom displacements as boundary conditions. To test a material model, the material model was used within the FE model and the reaction force of the FE model was then calculated and compared to the reaction force obtained from the experiments. Twenty-eight different material models were determined using the different tests and methods. As a first filter, only models that predicted logical material behaviour were used within the validation test. This was necessary because a successful FE analysis was required to obtain results. It was also observed that material models obtained from both identification methods for the same test gave similar results, thus only the best material model was further investigated. For the Mooney-Rivlin three parameter models, the following had an error percentage of less than 10 %:

1. (0.44 %) Inverse method on uni-axial tensile data (flat strip samples).

2. (-0.89 %) Inverse method on bi-axial bubble inflation data.

3. (-1.16 %) Direct method on bi-axial bubble inflation data.

4. (-1.91 %) Direct method on uni-axial tensile data (dumbbell shaped samples).

5. (2.37 %) Inverse method on a combination of uni-axial tensile and compression data.

6. (-3.36 %) Inverse method on uni-axial tensile data (dumbbell shaped samples).

7. (3.97 %) Direct method on a combination of uni-axial tensile and compression data.

8. (4.23 %) Direct method on uni-axial tensile data (flat strip samples).

For the Ogden three parameter models, the following had an error percentage of less than 10 %:

1. (-0.04 %) Inverse method on uni-axial tensile data (dumbbell shaped samples).

2. (4.93 %) Inverse method on uni-axial tensile data (flat strip samples).

3. (5.85 %) Direct method on uni-axial tensile data (dumbbell shaped samples).

4. (7.12 %) Direct method on uni-axial tensile data (flat strip samples).

5. (7.87 %) Inverse method on a combination of uni-axial tensile and compression data.

6. (8.05 %) Direct method on a combination of uni-axial tensile and compression data.

A negative answer indicates an under-prediction of engineering stress and vice versa.

Seven material models were further investigated by extrapolating the material model over all three stress states: uni-axial tension, uni-axial compression and bi-axial tension. It was observed that there exists a possible trade off within the material models, where the accuracy of the bi-axial tensile and uni-axial compression data are indirectly connected. By means of visual inspection, the Mooney-Rivlin three parameter models obtained from uni-axial tests and using the direct method (positive constant constraints) and the inverse FE model updating method were the best.

Although the direct method is faster to use, the inverse method ensures that the material model obtained will always predict feasible material behaviour, without the use of constraints if the initial parameters are valid.

11.4   Future Work

Only three experimental tests were conducted in this thesis. The introduction of more experimental tests such as a shear test or planar bi-axial tensile test will result in more stress states to analyse, and thus will result in a better understanding of the material's behaviour.

Only three commonly used hyper-elastic material models were considered. Introducing more material models and a more in depth investigation into the material models might result in a better prediction of the material's behaviour.

In this thesis both identification methods performed similarly. To further investigate the advantage of using the inverse FE model updating method, it can be used on a test sample having a complex stress state to obtain material models. This might be an interesting study, for a direct identification method would not be possible.

An in-depth study on the effects of curing temperature and curing time at that temperature will also result in a better understanding of the material's behaviour. Although for such a study, it might be necessary to use different kinds of silicone-rubbers. Repeating this study on different kinds of silicone-rubbers will also answer the repeatability of this thesis' results and broaden the current knowledge on such materials.

Appendices

Appendix A

X and Y Displacements vs. Y Displacements

The effect of using full field displacements (X and Y) vs. only using the longitudinal displacements (Y) during the inverse FE model updating method for rectangular flat strips was investigated. This was achieved by determining a Mooney-Rivlin three parameter model for each displacement field. Figure A.1 shows the engineering stress-stretch graph obtained from each displacement field. It can be observed that the difference between then is negligible small.
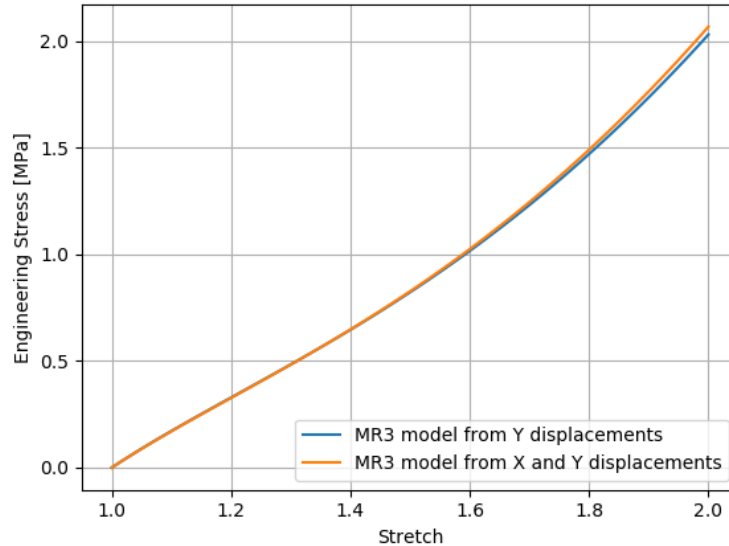

Figure A.1: Graph showing engineering stress-stretch for full field displacements vs. only longitudinal displacements.

Appendix B

Bi-axial Bubble Inflation Experimental Data Polynomial Fit

Figure B.1 and Figure B.2 shows a typical fourth order polynomial fit for the X and Y-displacements of bi-axial bubble inflation tests respectively. Both had an R-squared value of 0.997. The red lines present a perfect prediction.
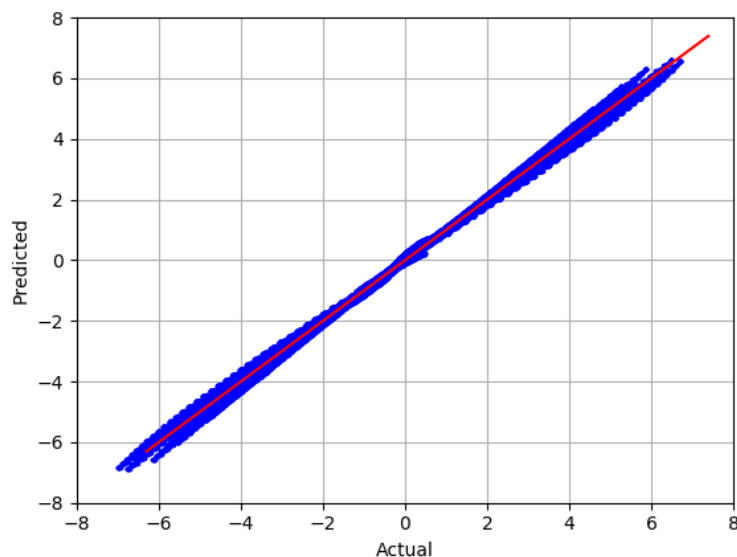

Figure B.1: Typical fourth order fit for X-displacement obtained from bi-axial bubble inflation tests.

To validate the assumption that the bubble deforms symmetric, Figure B.3 shows the top view of the bubble inflation membrane. The original virtual circle, how the circle deformed at a pressure of 150 kPa and a circle fit on the deformed virtual circle. It can be observed that the deformed virtual circle is
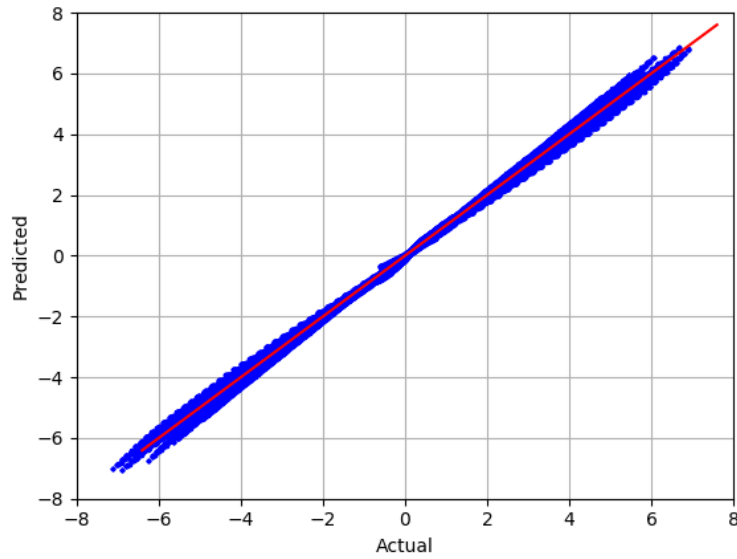
83

Figure B.2: Typical fourth order fit for Y-displacement obtained from bi-axial bubble inflation tests.

symmetric and the centre is in the membrane centre.

Figure B.4 shows the bubble deformation at a pressure of 140 kPa. It can be observed that the bubble deform hemispherical. Thus the assumption for hemispherical deformation holds true.
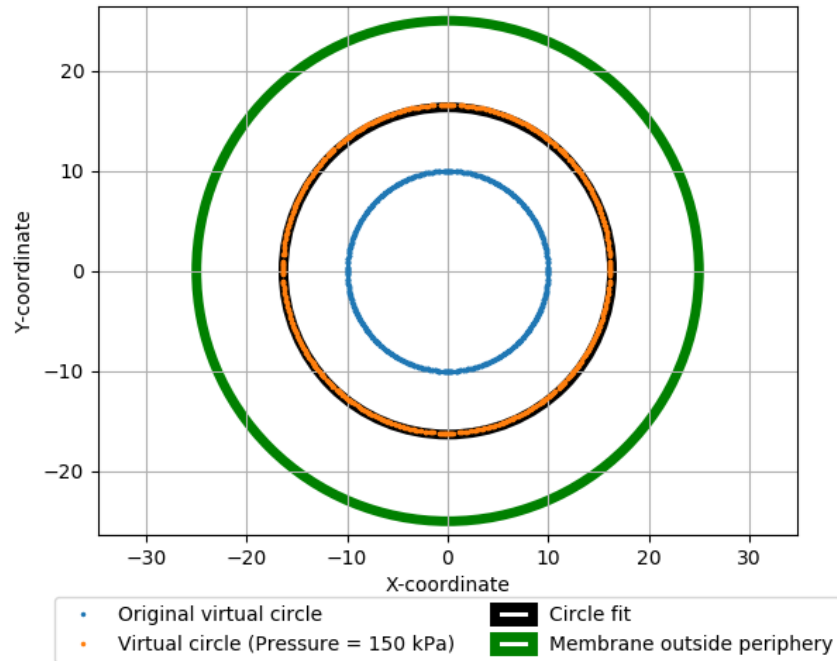
Figure B.3: Top view of bubble inflation membrane. The virtual circle's symmetrical deformation can be observed.
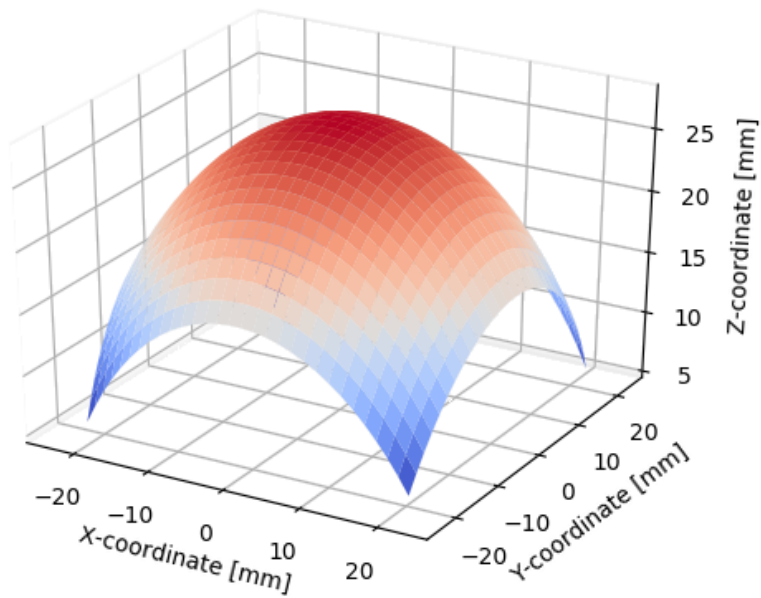

Figure B.4: Bubble inflation membrane's deformation at a pressure of 140 kPa.

Appendix C

Calibration of Kern EMB 600-2 Scale

To calculate the accuracy of the scale used to mix the two parts of silicone when moulding, a calibration was done using standard engineering calibration weights. Five consecutive measurement tests were done, all ranging from 1 g to 50 g. The average relative error was calculated to be 0.61 %. Figure C.1 shows a graph with the 5 measurement tests. A linear fit was done on the average of the measurements, to obtain a correction factor. For this thesis the correction factor is assumed to be small and is being neglected.
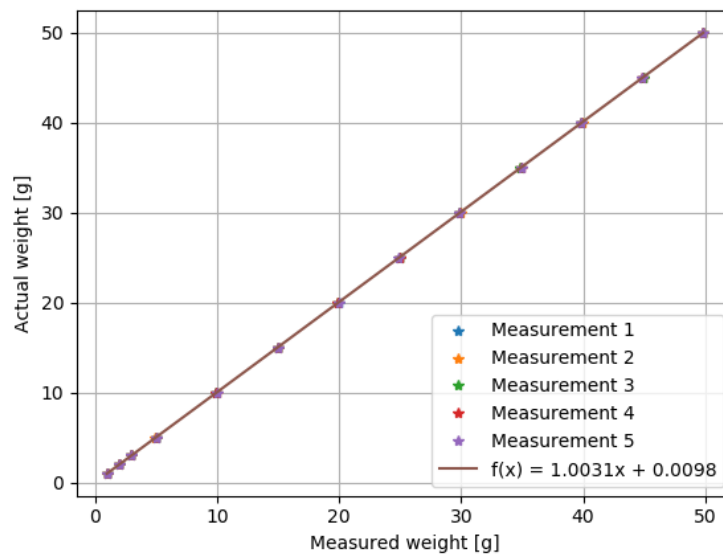

Figure C.1: Graph showing actual vs. predicted weight for Kern EMB 600-2 scale.

Appendix D

Calibration MTS 1kN Load Cell

To calculate the accuracy of the MTS 1 kN load cell, used during uni-axial tensile testing, a calibration was done using standard engineering calibration weights. Five consecutive measurement tests were done, all ranging from 2 N to 49 N. The average relative error was calculated to be 0.996 %, and the average repeatability error was 0.416 %. Figure D.1 shows a graph with the 5 measurement tests. A linear fit was done on the average of the measurements, to obtain a correction factor. For this project the correction factor is used to correct the measured force during tests.
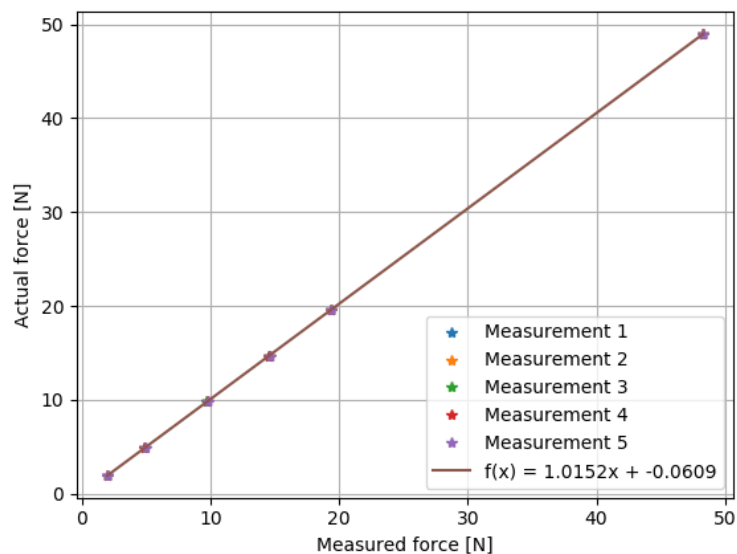

Figure D.1: Graph showing measured force vs. actual for 5 measurements to obtain relative error.

After the uni-axial tensile tests were completed, a HBM 500 N load cell became available. To further validate the 1 kN MTS load cell, four uni-axial tensile tests were done using the 500 N HBM load cell with dumbbell shaped samples. The test method was the same as described in Chapter 6. Figure D.2 shows the engineering stress-stretch graph for dumbbell shaped samples during uni-axial tensile tests using a 1 kN and 500 N load cell. Relative one standard deviation error bars are also shown. It can thus be concluded that the results are the same.
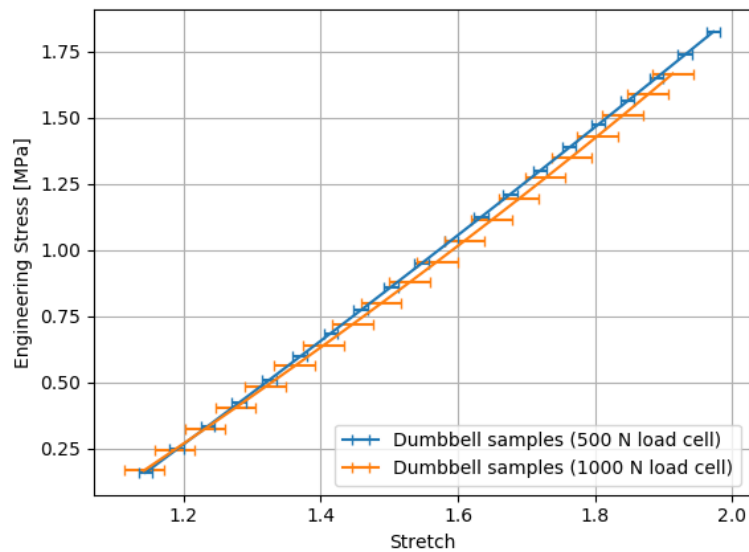

Figure D.2: Engineering stress-stretch graph showing the comparison between using a 1 kN and 500 N load cell with one standard deviation error bars.

Appendix E

FESTO Pressure Transducer

To calibrate the 200 kPa FESTO pressure transducer used during bi-axial bubble tests, a HBM Spider8 data logger was used parallel to the DIC system. The voltage readings of both systems are then compared, using the HBM Spider8 as the actual, the DIC system can be calibrated. Figure E.1 shows the predicted vs. actual voltage graph obtained, the solid blue line represents a perfect match. With a R-squared value of 0.999, a linear fit was then used to correct the DIC system's readings. To convert the voltage readings to pressure, a manufacturer calibration sheet was used. Table E.1 shows the calibration sheet data from the manufacturer.

Table E.1: FESTO pressure transducer calibration data sheet.

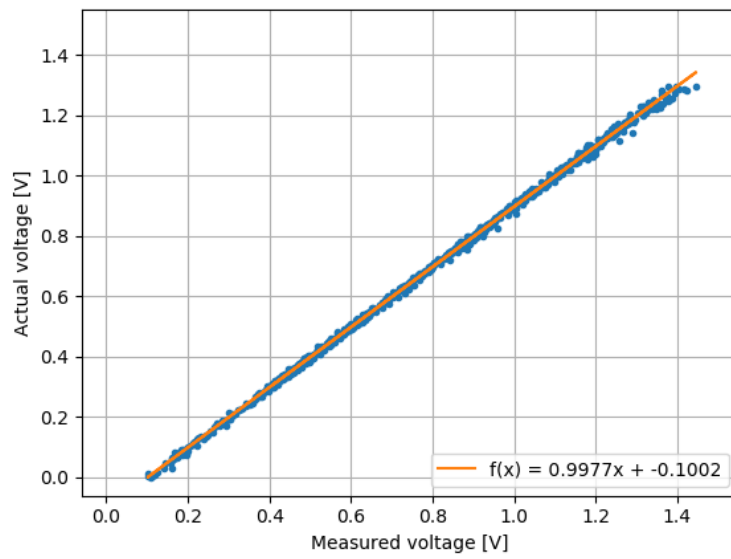| Pressure [kPa]	Voltage [V]
0	0.116
100	1
200	2

Figure E.1: Graph showing measured force vs. actual for 5 measurements to obtain relative error.

Appendix F

Mesh Refinement Study: Uni-axial Tensile Rectangular Flat Strip Samples

To validate the FE model used for the rectangular flat strip samples, a mesh refinement study was done. An arbitrary Mooney-Rivlin three parameter model was chosen. Table F.1 shows the Mooney-Rivlin constants used. The boundary conditions were the same as described in Chapter 6. Figure F.1 shows how the maximum displacement converges as the number of elements increases. It can be observed that using around 200 elements is enough for convergence.

Table F.1: Arbitrary Mooney-Rivlin three parameter constants used for mesh refinement study (rectangular flat strip samples).

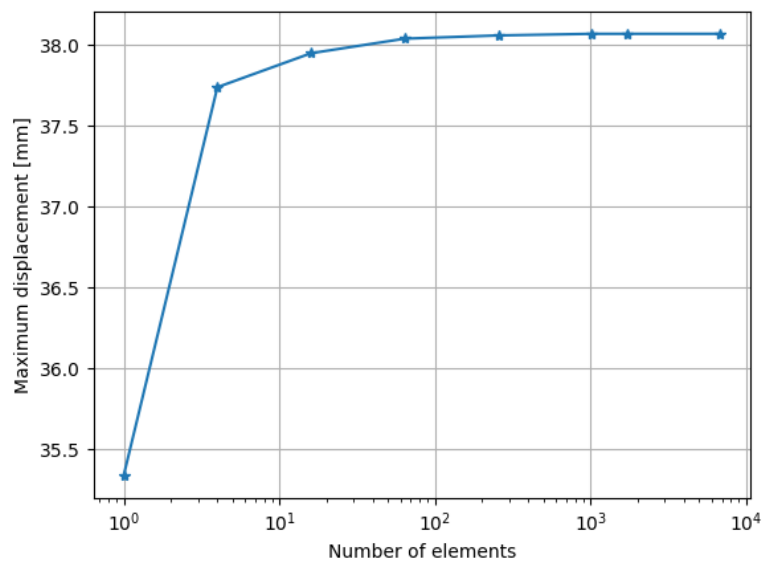| Model constant	Value [Pa]
C_{10}	315571
C_{01}	-5931.41
C_{20}	66929

Figure F.1: Graph showing how maximum displacement converges as number of elements increases (rectangular flat strip samples).

Appendix G

Mesh Refinement Study: Uni-axial Tensile Dumbbell Shaped Samples

To validate the FE model used for the dumbbell shaped samples, a mesh refinement study was done. An arbitrary Mooney-Rivlin three parameter model was chosen. Table G.1 shows the Mooney-Rivlin constants used. The boundary conditions were the same as described in Chapter 6. Figure G.1 shows the maximum reaction force vs. number of elements. It can be observed that the difference between the maximum and minimum is 0.0003 N, thus it can be concluded that using any number of elements is sufficient.

Table G.1: Arbitrary Mooney-Rivlin three parameter constants used for mesh refinement study (dumbbell shaped samples).

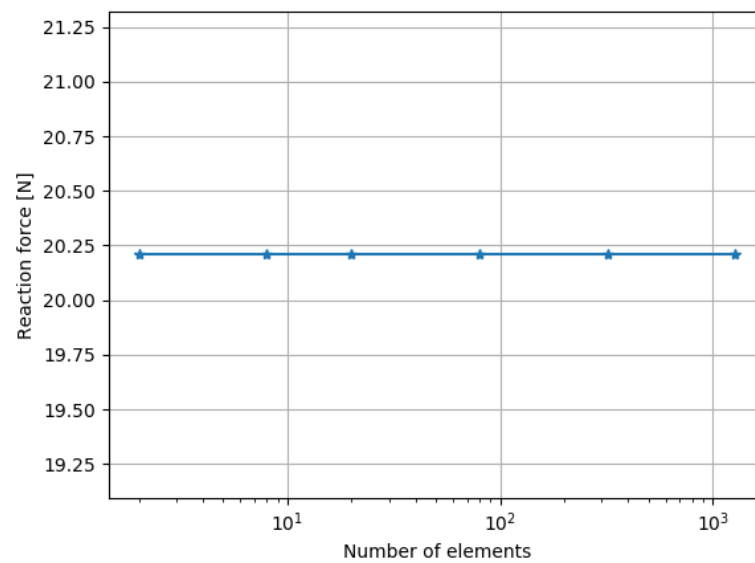| Model constant	Value [Pa]
C_{10}	297329
C_{01}	10533.8
C_{20}	59147.3

93

Figure G.1: Graph showing maximum reaction force vs. number of elements (dumbbell shaped samples).

Appendix H

Mesh Refinement Study: Bi-axial Bubble Inflation Membranes

To validate the FE model used for the bubble inflation membranes, a mesh refinement study was done. An arbitrary Mooney-Rivlin three parameter model was chosen. Table H.1 shows the Mooney-Rivlin constants used. The boundary conditions were the same as described in Chapter 7. Figure H.1 shows the maximum displacement convergence at the number of elements increases. It can be observed that using around 700 elements should sufficient.

Table H.1: Arbitrary Mooney-Rivlin three parameter constants used for mesh refinement study (bubble inflation membranes).

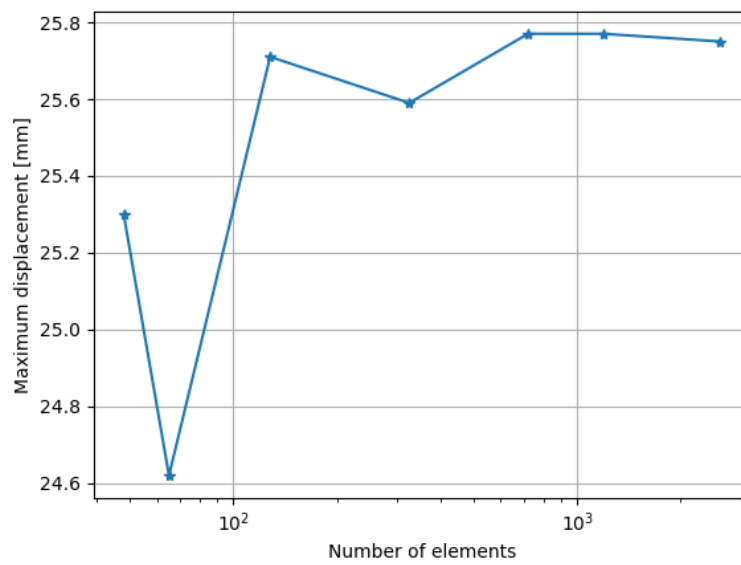| Model constant	Value [Pa]
C_{10}	624011
C_{01}	-371538
C_{20}	195009

Figure H.1: Graph showing maximum displacement convergence as number of elements increases (bubble inflation membranes).

Appendix I

Mesh Refinement Study: Unconstrained Uni-axial Compression Samples

To validate the FE model used for the unconstrained uni-axial compression samples, a mesh refinement study was done. An arbitrary Mooney-Rivlin three parameter model was chosen. Table I.1 shows the Mooney-Rivlin constants used. The boundary conditions were the same as described in Chapter 8. Figure I.1 shows the maximum displacement convergence and the analysis time as the number of elements increases. It can be observed that using around 1000 elements is sufficient, for the increase in accuracy is not worth the computational time increase.

Table I.1: Arbitrary Mooney-Rivlin three parameter constants used for mesh refinement study (uni-axial compression samples).

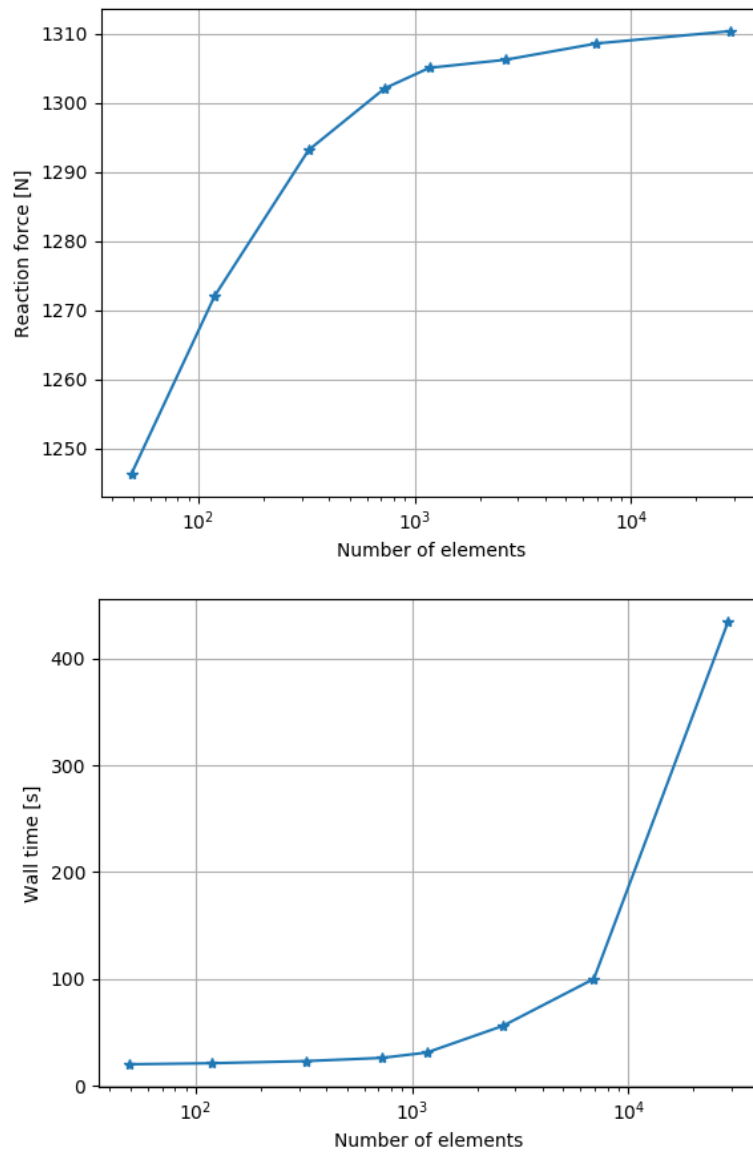| Model constant	Value [Pa]
C_{10}	687592
C_{01}	-203701
C_{20}	96561.5

Figure I.1: Graph showing maximum displacement convergence and analysis time as number of elements increases (uni-axial compression samples).

Appendix J

Mesh Refinement Study: Uni-axial Tensile Validation Samples

To validate the FE model used for the uni-axial validation samples, a mesh refinement study was done. An arbitrary Mooney-Rivlin three parameter model was chosen. Table J.1 shows the Mooney-Rivlin constants used. The boundary conditions were the same as described in Chapter 10. Figure J.1 shows the maximum reaction force convergence and the analysis time as the number of elements increases. It can be observed that using around 1000 elements is sufficient, for the increase in accuracy is not worth the computational time increase.

Table J.1: Arbitrary Mooney-Rivlin three parameter constants used for mesh refinement study (uni-axial validation tensile samples).

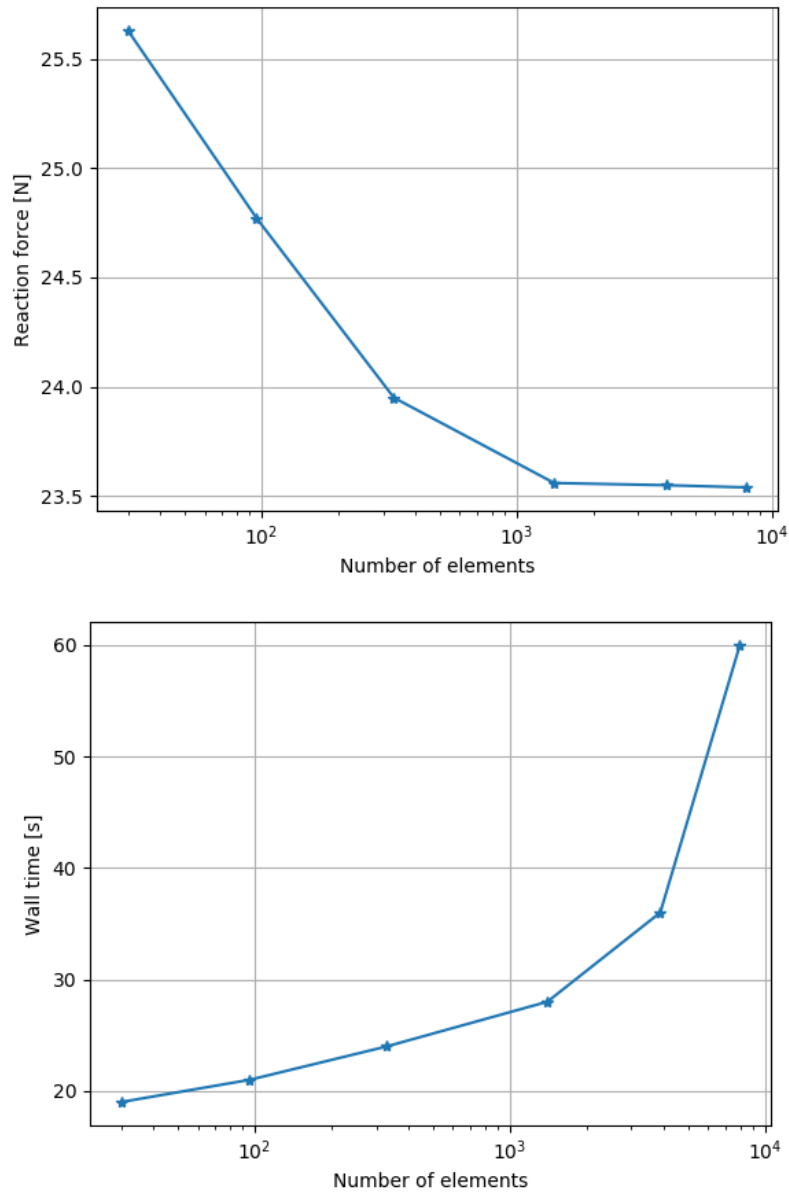| Model constant	Value [Pa]
C_{10}	339943
C_{01}	-120038
C_{20}	95459.1

Figure J.1: Graph showing maximum reaction force convergence and analysis time as number of elements increases (uni-axial validation tensile samples).

References

Bojtos, A. (2010). Optical measuring system for equibiaxial test of hyperelastic rubber-like materials. , no. 1, pp. 170–173.

Case, J.C., White, E.L. and Kramer, R.K. (2015). Soft Material Characterization for Robotic Applications. vol. 2, no. 2, pp. 80–87.

Crammond, G., Boyd, S. and Dulieu-Barton, J. (2013). Speckle pattern quality assessment for digital image correlation. *Optics and Lasers in Engineering*, vol. 51, pp. 1368–1378.

Fazzini, M., Dalverny, O. and Mistou, S. (2011). Identification of materials properties using displacement field measurement. *Key engineering materials*, vol. 482, pp. 57–65.

Garbowski, T., Maier, G. and Novati, G. (2011). On calibration of orthotropic elastic-plastic constitutive models for paper foils by biaxial tests and inverse analyses. *Structural and Multidisciplinary Optimization*, vol. 46, pp. 111–128.

Gent, A. (2012). *Engineering with rubber: How to design rubber components.* 3rd edn. Cincinnati: Hanser Publications.

Holzapfel, G.A. (2000). *Non-linear Solid Mechanics.* John Wiley and Sons, New York.

Jekel, C.F. (2016). Obtaining non-linear orthotropic material models for pvc-coated polyester via inverse bubble inflation. , no. March.
Available at: http://hdl.handle.net/10019.1/98627

Jekel, C.F., Venter, G. and Venter, M.P. (2016). Obtaining a hyperelastic non-linear orthotropic material model via inverse bubble inflation analysis. *Structural and Multidisciplinary Optimization*, vol. 54, no. 4, pp. 927–935. ISSN 16151488.

LaVision, G. (2014). Product-manual davis 8.2 software.

Martins, P.A.L.S., Jorge, R.M.N. and Ferreira, A.J.M. (2006). A Comparative Study of Several Material Models for Prediction of Hyperelastic Properties: Application to Silicone-Rubber and Soft Tissues. *Strain*, vol. 42, no. 3, pp. 135–147. ISSN 00392103.

Meunier, L., Chagnon, G., Favier, D., Orgéas, L. and Vacher, P. (2008). Mechanical experimental characterisation and numerical modelling of an unfilled silicone rubber. *Polymer Testing*, vol. 27, no. 6, pp. 765–777. ISSN 01429418.

Mooney, M. (1940). A theory of large elastic deformation. *Journal of Applied Physics*, vol. 11.

MSC Software, C. (2015). *Marc 2015, Volume A: Theory and user information.* MSC Software Corporation, 4675 MacArthur Court, Suite 900, Newport Beach, CA.

Ogden, R.W. (1984). *Non-linear Elastic Deformations.* Dover Publications Inc., Mineola, NY, USA.

Polygerinos, P., Lyne, S., Wang, Z., Fernando, L., Mosadegh, B., Whitesides, G.M. and Walsh, C.J. (2013). Towards a Soft Pneumatic Glove for Hand Rehabilitation. *IEEE/RSJ International Conference on Intelligent Robots and Systems*, pp. 1512–1517.

Rachik, M., Schmidt, F., Reuge, N., Y., L.M. and F., A. (2001). Elastomer Biaxial Characterization Using Bubble Inflation Technique. II: Numerical Investigation of Some Constitutive Models. *Polymer Engineering and Science*, vol. 41, no. 3, pp. 532–541.

Rackl, M. (2015). Curve fitting for ogden, yeoh and polynomial models. *ScilabTEC conference 2015*.

Reuge, N., Schmidt, F.M., Le Maoult, Y., Rachik, M. and Abbé, F. (2001). Elastomer biaxial characterization using bubble inflation technique. I: Experimental investigations. *Polymer Engineering and Science*, vol. 41, no. 3, pp. 522–531. ISSN 00323888.

Rey, T., Chagnon, G., Cam, J.L. and Favier, D. (2013). Influence of the temperature on the mechanical behaviour of filled and unfilled silicone rubbers. *Polymer Testing*, vol. 32, pp. 492–501.

Rivlin, R.S. (1948). Large elastic deformations of isotropic materials. iv. further developments of the general theory. *Philosophical Transactions of the Royal Society of London. Series A, Mathematical and Physical Sciences*, vol. 2.

Sasso, M., Palmieri, G., Chiappini, G. and Amodio, D. (2008). Characterization of hyperelastic rubber-like materials by biaxial and uniaxial stretching tests based on optical methods. *Polymer Testing*, vol. 27, no. 8, pp. 995–1004. ISSN 01429418. Available at: http://dx.doi.org/10.1016/j.polymertesting.2008.09.001

Smooth-On (2012). Smooth-sil series: addition cure silicone rubber compounds. http://www.amtcomposites.co.za/products/silicone-rubber/platinum-cure. Accessed: 17 February 2017.

Treloar, L.R.G. (1944). Trans. inst. rubber ind. 19. vol. 201.

Vanderplaats Research & Development, I. (2013*a*). *Design Optimization Tools (DOT) users manual, version 6.* VR&D, 1767 S. 8th Street, Suite 200, Colorado Springs, CO.

Vanderplaats Research & Development, I. (2013*b*). *VisualDOC theory manual, version 7.2.* VR&D, 1767 S. 8th Street, Suite 200, Colorado Springs, CO.

Vanderplaats Research & Development, I. (2013, July). *VisualDOC user's manual, version 7.2.* VR&D, 1767 S. 8th Street, Suite 200, Colorado Springs, CO.

Venter, G. (2010). *Encyclopedia of Aerospace Engineering, chapter Review of Optimization Techniques.* John Wiley and Sons.